

The Atom Probe FIM

by

John A. Panitz

An Abstract of a Thesis

in

Physics

Submitted in Partial Fulfillment  
of the Requirements  
for the Degree of

Doctor of Philosophy

December 1969

The Pennsylvania State University  
The Graduate School  
Department of Physics

## ABSTRACT

The ultimate microanalytical tool would be an instrument capable of selecting and identifying the individual constituents of a surface seen in atomic resolution. Within certain limits, set primarily by the type of material which can be successfully examined, the atom probe F.I.M. can do just this.

A surface species, imaged in a field ion microscope, is selected for examination by positioning its image over a small "probe hole" in the microscope's fluorescent screen. The selected particle is then removed from the surface as a positive ion by field evaporation, and travels through the probe hole into a time-of-flight mass spectrometer. The definite time correlation between the ion's impact at a suitable detector, and the evaporation event itself, allows the ion's travel time to be determined with great precision. Since its kinetic energy is also well defined and accurately known, its mass-to-charge ratio can be determined for a given distance of travel. Two independent calibration techniques assure an overall accuracy of  $\pm 1.0$  amu at  $m/n = 50$ , or in special cases,  $\pm 0.2$  amu at  $m/n = 50$ . Time resolution is more than sufficient to unambiguously resolve the two isotopes of iridium when triply charged.

Results with a prototype and a refined instrument showed an unexpectedly high ionic charge for field evaporated tungsten, and confirmed the double charged ion predicted by field evaporation theory as the abundant species for most metals. The existence of adsorbed hydrogen as well as adsorbed noble imaging gases on a "clean" imaged surface has been demonstrated as well as the occurrence of metal-noble gas, and metal-hydrogen molecular ions. The zone line decorations of tungsten and iridium as well as some alloys have been successfully examined. Finally, the process of charge exchange, and the spatial dissociation of molecular ions originating on the surface have been considered.

The Pennsylvania State University

The Graduate School

Department of Physics

The Atom Probe FIM

A Thesis in

Physics

by

John A. Panitz

Submitted in partial fulfillment  
of the requirements  
for the degree of

Doctor of Philosophy

December 1969

Date of Approval:

Nov. 4, 1969

Erin W. Miller  
Evan-Pugh Research Professor of Physics  
Thesis Adviser

Nov. 4, 1969

D. H. Rank  
Evan-Pugh Research Professor of Physics  
Head of Department of Physics

## ACKNOWLEDGMENT

The success of the current atom probe program has been due, in large measure, to the active cooperation between Professor E. W. Müller, Mr. S. B. McLane, Mr. G. E. Fowler, and the author.

In particular, the greatest portion of the atom probe's success must be directly attributed to Professor Müller who conceived the principle of the instrument and participated, spiritedly, in every phase of its development. His original suggestion of the problem, his designs, and his active and continual interest are all gratefully acknowledged.

Special thanks are also due to Mr. S. B. McLane who not only developed and operated the special electronic equipment needed, but also was the source of many fruitful ideas, suggestions, and conversations.

The technical competence, versatility, and interest of Gerald E. Fowler are also recognized, and appreciated. Mr. Fowler, in addition to assembling major portions of the instrument, provided continual technical assistance throughout the entire program.

Finally, the author wishes to thank the National Science Foundation who supported this work under NSF grant GP7452 to Professor E. W. Müller.

## TABLE OF CONTENTS

	Page
Acknowledgments . . . . .	ii
List of Figures . . . . .	iv
I. INTRODUCTION . . . . .	1
II. THEORY OF OPERATION . . . . .	6
III. A PROTOTYPE INSTRUMENT . . . . .	9
IV. THE ATOM PROBE FIM	
Vacuum and Gas Supply Systems . . . . .	18
Cold Finger Assembly . . . . .	23
Image Observation and Photography . . . . .	26
Ion Detector . . . . .	32
Electronics . . . . .	39
Alignment . . . . .	43
V. PERFORMANCE OF THE INSTRUMENT	
Further Theoretical Considerations . . . . .	50
Calibration . . . . .	66
Resolution and Accuracy . . . . .	75
VI. AIMING THE ATOM PROBE . . . . .	79
VII. EXPERIMENTAL RESULTS . . . . .	85
VIII. SUMMARY AND CONCLUSION . . . . .	109
APPENDIX A, Ion Travel Times Between Confocal Parabolic Electrodes . . . . .	111
APPENDIX B, The Newton-Raphson Method . . . . .	123
BIBLIOGRAPHY . . . . .	128

## LIST OF FIGURES

	Page
Figure 1. The Prototype Atom Probe (Schematic) . .	10
Figure 2. The Prototype Atom Probe . . . . .	11
Figure 3. Atom Probe Examination of Tungsten . . .	15
Figure 4. The Atom Probe Field Ion Microscope (Schematic) . . . . .	19
Figure 5. The Atom Probe Field Ion Microscope . .	20
Figure 6. The Atom Probe Vacuum System (Schematic) . . . . .	21
Figure 7. The Cold Finger Assembly and Alignment Jig . . . . .	25
Figure 8. The Atom Probe Field Ion Microscope (Front View) . . . . .	27
Figure 9. The Viewing Window and Binoculars . . .	28
Figure 10. The Screen and Valve Assembly . . . . .	30
Figure 11. Iridium Imaged in Helium (8.55kV) . . .	31
Figure 12. The Electron-Multiplier Detector . . . .	38
Figure 13. The Multiplier-Preamplifier Schematic . . . .	40
Figure 14. Atom Probe Examination of Rhodium . . .	42
Figure 15. The Axial Multiplier Potential . . . . .	55
Figure 16. (m/n) Correction Curves . . . . .	59
Figure 17. The Evaporation Pulse . . . . .	64
Figure 18. Abundance Histogram ( $\alpha = 1.0$ , $\delta = 0.0$ ) .	90
Figure 19. Abundance Histogram ( $\alpha = 2.0$ , $\delta = 0.02$ )	91
Figure 20. Charge-Exchange Pairs . . . . .	96
Figure 21. Charge-Exchange Pairs . . . . .	97

## LIST OF FIGURES (CONTINUED)

	Page
Figure 22. Abundance Histogram (Tungsten) . . . . .	99
Figure 23. Apparent $m/n$ vs. $V/V_0$ for Dissociation .	105
Figure 24. Dissociation Data for $H_2^+ \rightarrow H_1^+ + H_1$ . .	107
Figure 25. Terminal Travel Times ( $T_t$ ) . . . . .	118
Figure 26. Actual Travel Times ( $T_0$ ) for Confocal Paraboloid Geometry . . . . .	121



## I. INTRODUCTION

The field ion microscope, invented by Müller in 1951,<sup>1</sup> is the only instrument capable of resolving the individual atoms of a metal surface. In practice, each protruding surface atom of a specially prepared specimen is imaged on a fluorescent screen by a beam of ions, usually helium, formed some four angstroms above it in a narrow region of high ionization probability.<sup>2</sup> The image which is observed on the screen of the microscope is actually a highly magnified representation of these ionization regions. Since a one-to-one correspondence is present between each localized ionization region and the surface atom directly below it, the entire image represents the atomically resolved surface of the specimen. However, since this imaging process is similar for all surface atoms regardless of their chemical nature, it is usually not possible to use the appearance of the FIM image to directly discriminate between different atomic species at the surface. While it seems quite certain that only one kind of atom is present on pure W, Ir, Rh, or Pt surfaces characterized by a highly perfect FIM pattern, it is not possible to unambiguously identify the different atomic species forming the usually less regular FIM patterns which are obtained from alloys, crystals containing impurities, or adsorbates at the surface. Fortunately, the

field ionization of an ambient gas upon which the imaging process relies is not the only observable effect due to the presence of the high electric field near the surface. It is, in fact, an associated process called field evaporation which actually allows the surface species to be determined.

The theory of field evaporation has been covered in detail elsewhere,<sup>3,4</sup> and therefore, will not be reviewed here. Basically, it describes the field ionization of a surface atom or molecule followed by thermal activation over a field-reduced energy barrier. The result is that surface species, in the form of positive ions, may be removed from the metallic emitter at a well-defined, controllable rate. The rate is fixed by the electric field strength at the surface and; therefore, by the potential difference applied between emitter and screen. Coupling this source of surface ions with a mass spectrometer, a suggestion first advanced by Müller,<sup>5</sup> permits their mass-to-charge ratio to be determined. Since field evaporation theory, even in its somewhat contrived form, can usually predict the charge of the evaporated species the mass is also known.

Because of experimental difficulties in obtaining long-term ion currents of appreciable magnitude from a

field evaporation source, most previous experiments have been concerned with field ionization--not evaporation--mass spectroscopy. This technique utilizes the extremely high electric field near the tip to ionize ambient gases or organic vapors, the ions formed being analyzed in a suitable spectrometer. Ingram and Gomer<sup>6</sup> presented the first experimental results with the publication of their study of the field ionization of hydrogen and deuterium. Later, Müller and Bahadur<sup>7</sup> investigated, qualitatively, the field ion spectrum of hydrogen. Clements,<sup>8</sup> studying the abundance of ion species in high ambient gas pressures, discovered the  $\text{H}_3^+$  ion in the field ionized hydrogen spectrum. Beckey,<sup>9</sup> et.al., extended the technique to include the study of field induced dissociation products of hydrocarbons, using both conventional electron impact, and modified field ionization sources. Thomsen,<sup>10</sup> in addition to studying the low pressure spectra of field ionized gases, reported the first observation of an abundant field evaporated ion,  $\text{CuH}_2^+$ , during his investigation of the field evaporation of beryllium copper in  $10^{-7}$  Torr of hydrogen. Barofsky<sup>11</sup> originally continued Clements' study of the field ionized hydrogen spectra, but later<sup>12</sup> was able to examine the low temperature field evaporation products of Be, Fe, Zn, and Cu. His investigation of the last metal confirmed Thomsen's original observation of the abundant  $\text{CuH}_2^+$  ion.

Although Thomsen's work, and more particularly Barofsky's, resulted in the detection and identification of surface species during field evaporation, both investigators were limited by their apparatus. Thomsen did not have a suitable detector. Neither could localize the region of the emitter from which the ions originated, neither could preselect surface species of interest, and neither could work with fewer than perhaps  $10^4$  ions per second entering their spectrometers.

It is quite apparent that a major advance in both field ion mass spectroscopy and surface physics would be achieved with the positive identification of the atomic species associated with preselected, individual, image spots. To accomplish this feat, Müller,<sup>13</sup> in 1967, realizing that single ion detection was possible, suggested a novel combination of field ion microscope and mass spectrometer now called the Atom Probe FIM. The device incorporating single particle detection capability, relies upon the strict time correlation between a field evaporation and detection event, to eliminate random detector noise.

The atom probe was named (according to Riviere,<sup>14</sup> incorrectly) in analogy with the well-known electron microprobe developed by Castaing.<sup>15</sup> This instrument, a combination electron microscope and X-ray analyzer, can

investigate the constituents of a small section of specimen which, although typically of the order of one micron in size, still contains  $10^{11}$  atoms. The scanning electron microprobe developed by Crewe,<sup>16</sup> using a field emission source and an energy analyzer, may provide still another form of chemical analysis of selected specimen areas. The number of atoms involved, however, would still be greater than  $10^5$ .

Only with the atom probe FIM can one, ultimately, determine the identity of a single species seen with atomic resolution at a metal surface, and selected from neighboring atoms at the discretion of the experimenter. It is the purpose of this work to present, in some detail, the development of this most sensitive tool for microanalytical research.

## II. THEORY OF OPERATION

The atom probe consists of a field ion microscope modified so that the imaged atom chosen for analysis can be positioned over a small aperture, or "probe hole", in the microscope's phosphor coated screen. This probe hole provides an entrance into the analyzer which in the present designs has been a time of flight mass spectrometer with single particle resolution. After properly positioning the specimen so that the desired surface atom is imaged over the probe hole, and pumping away the imaging gas if desired, the specimen is subjected to a high voltage pulse. This pulse, superimposed on the steady state DC imaging voltage, is made sufficiently large so that the resulting electric field at the surface will cause a number of surface atoms to field evaporate as positive ions. Only the atom which was imaged over the probe hole passes, now as an ion, into the time of flight mass spectrometer; all of the other ions being blocked by the screen.

After traveling approximately one meter the ion collides with the first dynode of a multi-stage electron multiplier, thereby producing a signal which can be displayed on an oscilloscope. The recorded sweep, initiated by the evaporation pulse, is a direct measure of the ion's travel

time. If the duration of the evaporation pulse is made longer than the ion's travel time in the acceleration region near the tip, the evaporated ion will quickly attain a kinetic energy determined solely by the sum of the DC imaging voltage and evaporation pulse voltage. That is:

$$\frac{1}{2} m v_t^2 = ne (V_{dc} + V_{pulse}) \quad (1)$$

where  $ne$  is the ion's charge, and  $v_t$  its final, or terminal, velocity. Since the acceleration region near the tip is very short compared to the ion's total flight path, its travel time is, to a very good approximation, just

$$\tau \approx d/v_t \quad (2)$$

where  $d$  is the total tip to detector distance.

The ion selected for analysis is identified by its mass-to-charge ratio expressed as a function of the total voltage, travel time, and distance. Combining equations (1) and (2) gives the desired result:

$$\left(\frac{m}{n}\right)_o = K (V_{dc} + V_{pulse}) \tau^2 \quad (3)$$

where

$$K \equiv \frac{0.193}{d^2}$$

and  $V_{dc}$  and  $V_{pulse}$  are measured in kilovolts,  $\tau$  is measured in microseconds, and  $(\frac{m}{n})_0$  is expressed in terms of atomic mass units (amu). The constant  $K$  can be evaluated once the tip-to-screen distance,  $d$ , is known. For our instrument three different analyzer tube lengths have been used. Correspondingly, for  $d = 0.82m$ ,  $K = 0.228$ ; for  $d = 0.99m$ ,  $K = 0.195$ ; while for  $d = 1.98m$ ,  $K = 0.049$ .



### III. A PROTOTYPE INSTRUMENT

In order to demonstrate the feasibility of the atom probe concept, a prototype instrument was constructed. Although it has been fully described elsewhere,<sup>17</sup> its essential features will be repeated here, both for completeness, and to provide a comparison with the improved instrument to be described shortly.

Figure 1 is a schematic diagram of the prototype atom probe, while Figure 2 is a photograph of the instrument itself. The specimen to be examined is spot welded to a molybdenum wire loop which is held in position by two tungsten coils. The coils are formed from tungsten wires which are sealed through the base of a pyrex cold finger. These wires provide electrical contact to the specimen, while cooling it by conduction from the cryogenic liquid through which they pass. A grounded aluminum cone, making thermal contact with the cold finger, surrounds the tip and its mounting coils. Such a cone has been shown by Müller<sup>18</sup> to increase the intensity of the faint FIM image by as much as 300%.

The entire cold finger is inserted into the upper portion of the microscope body with the specimen tip positioned as closely as possible to the center of rotation of the greased ball joint assembly. When so placed, the tip

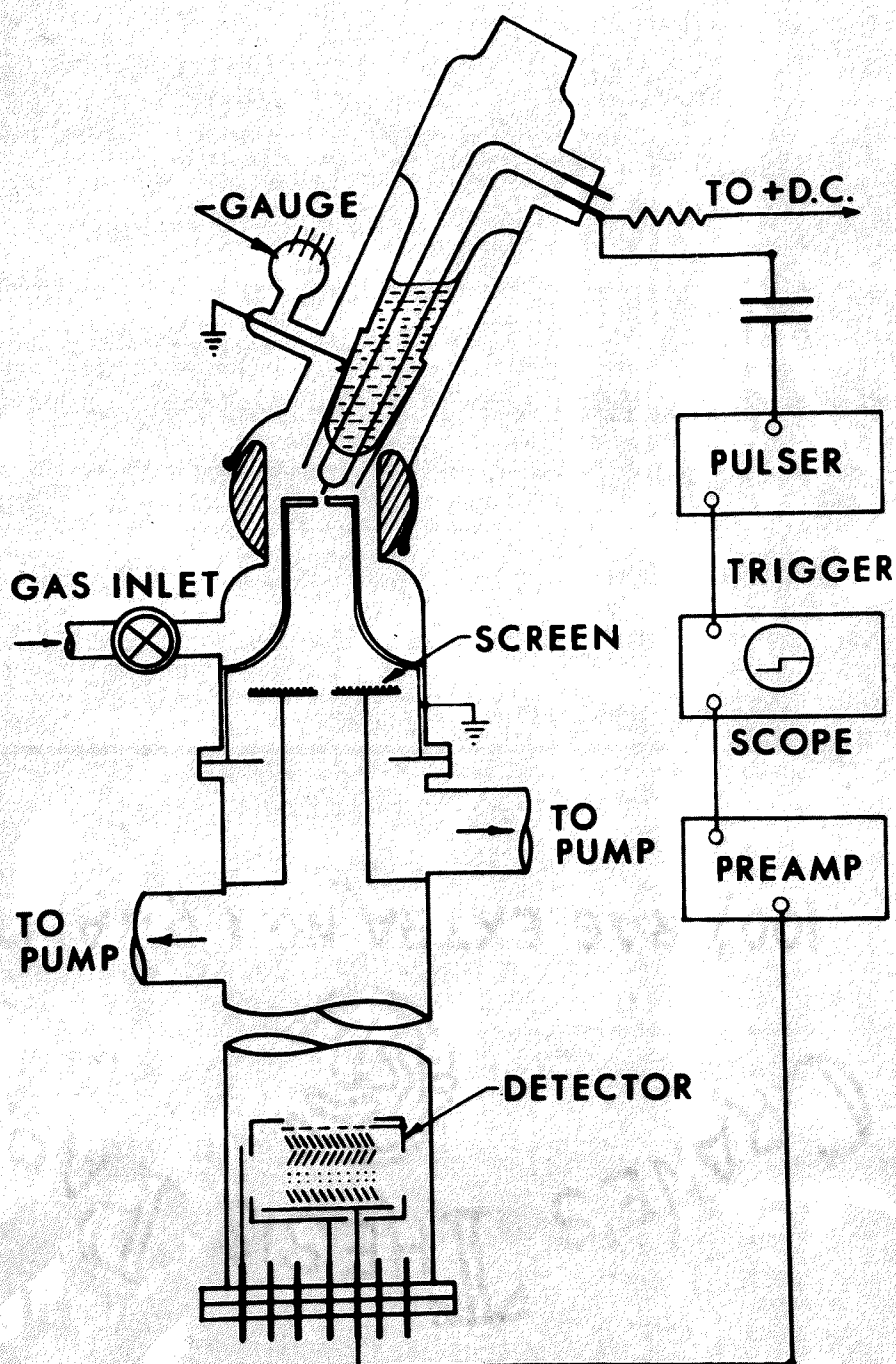


Figure 1. The Prototype Atom Probe (Schematic)

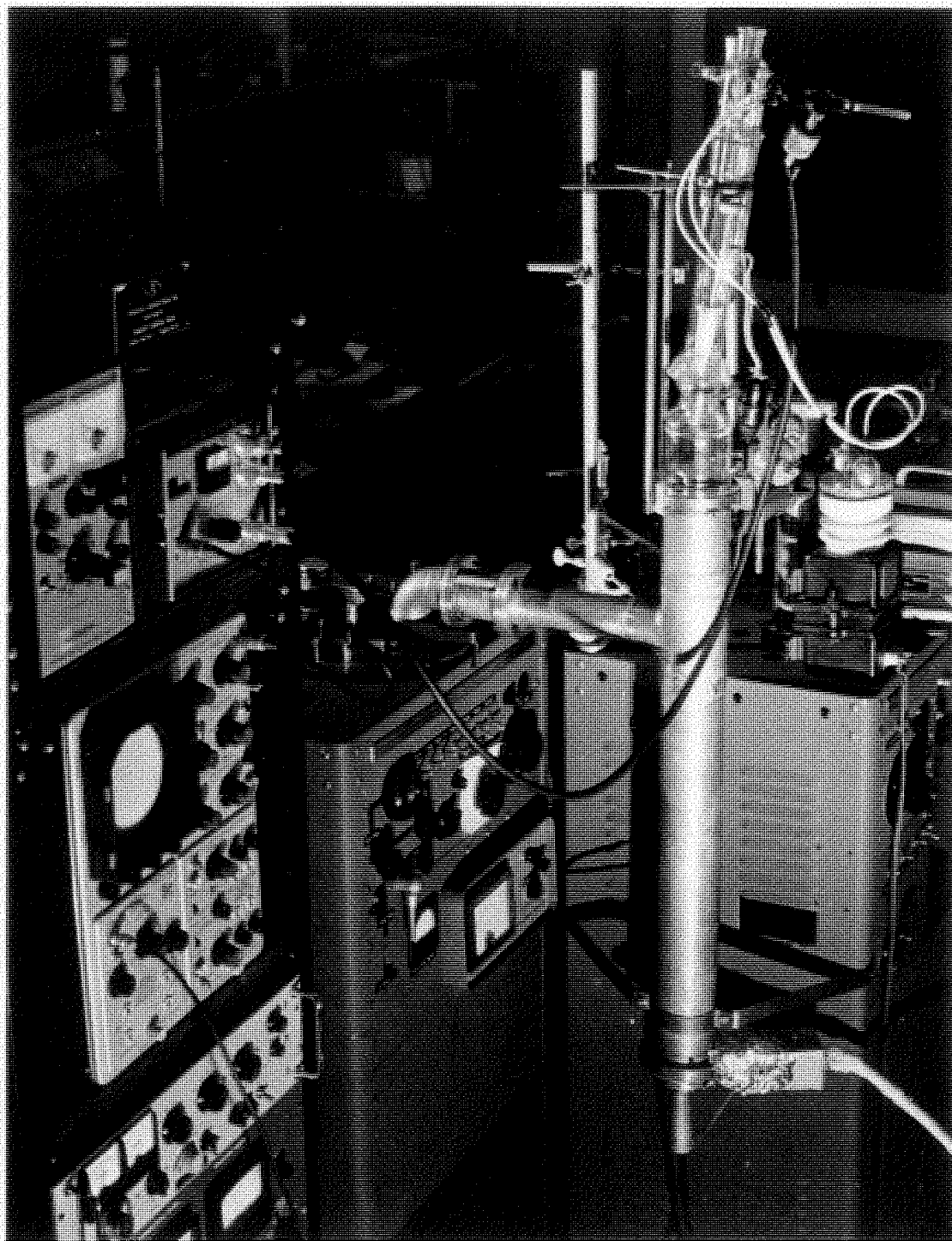


Figure 2. The Prototype Atom Probe Field Ion Microscope

is axially aligned with respect to the holes located in both the aluminum plate, and the fluorescent screen. The aluminum plate serves to separate the microscope into two sections. The upper, containing the tip, is connected to a supply of helium gas whose flow rate can be accurately adjusted. The lower portion, containing the screen, is connected to a liquid nitrogen trapped, 5 cm, oil diffusion pump. During imaging of the specimen, the lower portion of the microscope body is pumped while helium gas is admitted into the upper portion. This dynamic gas supply system<sup>19</sup> allows operation with one millitorr of imaging gas in the immediate vicinity of the tip, while maintaining the region near the screen at a considerably lower pressure.

The time-of-flight spectrometer, located directly behind the fluorescent screen, is continuously pumped by a separate, trapped, 5 cm, oil diffusion pump. With a probe hole one millimeter in diameter, the vacuum in this region is maintained, during imaging, at better than  $5.0 \times 10^{-6}$  Torr to insure that an adequate mean free path is obtained.

The evaporation pulse is supplied by a Huggins Laboratory pulse generator, model 961 D, which provides both adjustable pulse amplitude (0 to 3kV), and width. For the prototype atom probe a pulse width of 2.0 ns was chosen, with a corresponding rise and fall time of 0.5 ns sec.

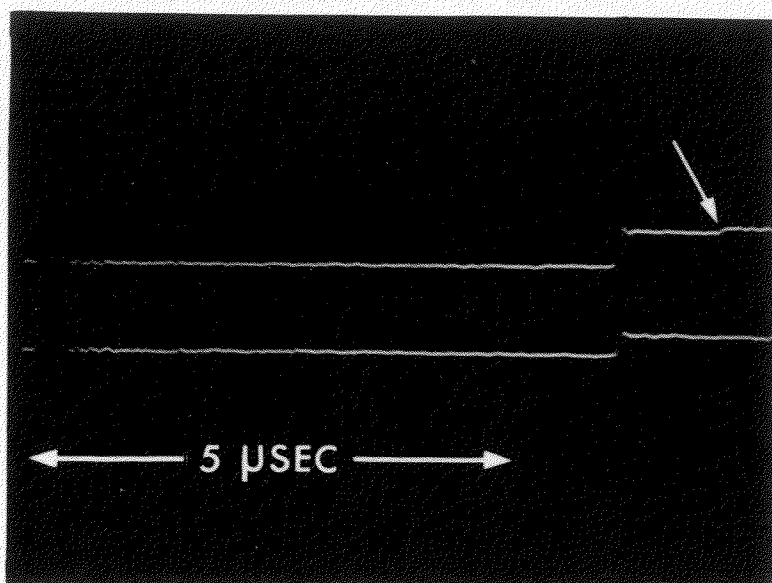
The actual pulse shape produced by the generator was observed at its output with a Tektronix type 519 oscilloscope. Manually triggered single pulses are normally used to field evaporate selected species, although the generator also permits 60 cycle repetitive operation. The evaporation pulse travels to the microscope head on a  $50\Omega$  coaxial cable terminated by a  $50\Omega$  resistor, and is coupled to the DC leads in the cold finger through a 500 pf, 30kV capacitor.

A "venetian blind" electron multiplier having a gain of  $\sim 10^6$  detects the field evaporated species. The physical configuration of this detector is similar to that of the one used currently in the improved atom probe, but incorporates 12 Be-Cu dynodes, and one anode. The multiplier assembly, mounted on a brass O-ring flange, is bolted to the base of the time-of-flight tube; all electrical connections to the multiplier being made through ceramic-to-metal seals soldered to the flange.

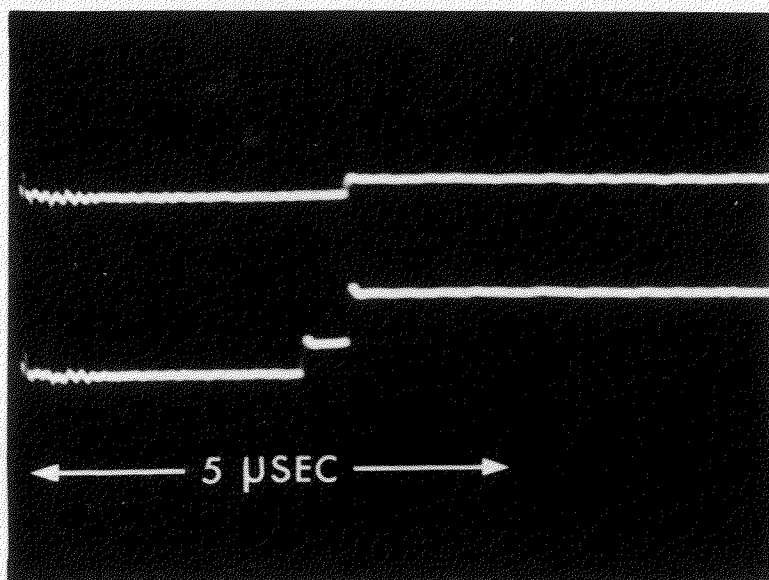
The anode of the electron multiplier is connected directly to a transistorized preamplifier originally designed by S. B. McLane<sup>12</sup> for a similar application. An overall current gain of greater than  $10^{12}$  was observed with the detector preamp combination. The 16 ns rise time of the Tektronix type 551 oscilloscope, used to measure

the time of flight, determined the rise time of the recorded pulse; the observed fall time of 1 msec was determined by the detector--preamplifier combination. Figure 3 is two typical oscilloscope photographs showing the recorded "staircase" wave shape resulting when two or more particles reached the detector during a single sweep. Since a single sweep lasts only 10 $\mu$ -seconds, and is initiated by the evaporation pulse, random events are effectively excluded from being recorded.

Preliminary results obtained with the prototype instrument indicated, at the relatively poor vacuum conditions present, the occurrence of tungsten--oxygen and tungsten--nitrogen compound ions on the surface. Figure 3B shows typical oscilloscope flight time data obtained for a tungsten specimen. For the upper trace, the species is  $^{182}\text{W } ^{16}\text{O}_2^{3+}$  ( $m/n = 71$ ), while for the lower trace (from left to right), the species are  $^{184}\text{W } ^{16}\text{O}_2^{4+}$  ( $m/n = 53.6$ ), and  $^{182}\text{W } ^{16}\text{O}_2^{3+}$  ( $m/n = 71.2$ ). In addition, the evaporation of rhenium-molybdenum alloys indicated that both metals field evaporated as doubly charged ions. A similar result was obtained for tungsten specimens, but  $\text{W}^{3+}$  and  $\text{W}^{4+}$  were also observed. Figure 3A resulted from an examination of tungsten at 21°K. A getter, installed near the tip, improved the background vacuum. For the upper trace (from left to right)  $m/n = 66$  and  $m/n = 91$ . For the lower



A. Tungsten at 9.0kV + 0.2kV pulse



B. Tungsten at 25kV + 2.4kV pulse

Figure 3. Atom Probe Examination of Tungsten

trace  $m/n = 66$ . These species are to be identified with  $^{182}\text{W } ^{16}\text{O}^{3+}$  ( $m/n = 91$ ), and  $^{182}\text{W } ^{16}\text{O}^{3+}$  ( $m/n = 66$ ) or  $^{184}\text{W } ^{14}\text{N}^{3+}$  ( $m/n = 66$ ).

Although a mass determination accurate to  $\pm 1.0$  amu was claimed, more refined experiments with the most recent instrument indicate that such a figure was probably quite optimistic. In fact, as will be discussed shortly, the very equation, equation (1), used for all the mass determinations must be refined by the incorporation of two correction factors.

Another problem with the device was that, although any region of the specimen could be positioned over the probe hole, the poor viewing conditions prevented both precise selection of single species, and photographing the image. Nevertheless, the prototype atom probe did demonstrate that the original concept of mass analyzing a single field evaporated particle was feasible. In addition, it provided novel preliminary results by establishing the unexpectedly high ionic charges of some field evaporated ions, while at the same time providing a firm basis on which to design future instruments.



## IV. THE ATOM PROBE FIM

Experience with the prototype atom probe was particularly valuable for it showed that a new instrument would have to incorporate several refinements if it was ever to perform as a versatile, microanalytical tool. It would have to provide a means of continually pumping the spectrometer, even during specimen change, so that the electron multiplier would not be exposed to the atmosphere. Repeated exposure, as observed in the prototype, contaminated the multiplier thereby seriously decreasing its gain. In addition, a means would have to be provided to bake the multiplier to 500°C, to reactivate it if contamination ever did occur. It would have to be possible to observe and photograph the weak FIM image without significant distortion, so that imaged atoms could be precisely selected and recorded. A background vacuum in the  $10^{-8}$  Torr range would have to be maintained in the microscope and analyzer sections, with sufficient pumping speed in the microscope so that the imaging gas could be removed as quickly as desired. A system to rapidly change specimens would have to be provided, as well as a means to positively align the tip, probe hole, and detector, and preserve this alignment during each tip change. Finally, the prototype instrument demonstrated the need to provide a convenient operating position for the experimenter, as well as a

system compatible with an external image intensifier for viewing and photographing the faint FIM image when extremely low imaging gas pressures were used. Figures 4 and 5 show the new horizontal atom probe which incorporates these, as well as other refinements, the most important of which is adequate electrical shielding of the specimen. Coupled with the mechanical refinements just mentioned have been definite improvements in the associated instrumentation to provide for more accurate, reliable and convenient operation.

#### 1. Vacuum and Gas Supply Systems:

Figure 6 is a schematic diagram of the vacuum and gas supply system. The microscope and spectrometer are each pumped by separate, trapped, oil diffusion pumps connected to a common foreline and a single, rotary, mechanical pump. A system of foreline valves allows either portion of the atom probe, microscope or spectrometer, to be rough pumped separately or isolated from the other portion as desired. Molecular sieve traps in the foreline prevent oil creep from the mechanical pump, while valves on either side of each trap permit bakeout when contamination eventually occurs.

The microscope head, like the major portion of the atom probe, is constructed of heliarc welded 304 stainless steel. It is connected by an O-ring flange to an NRC,

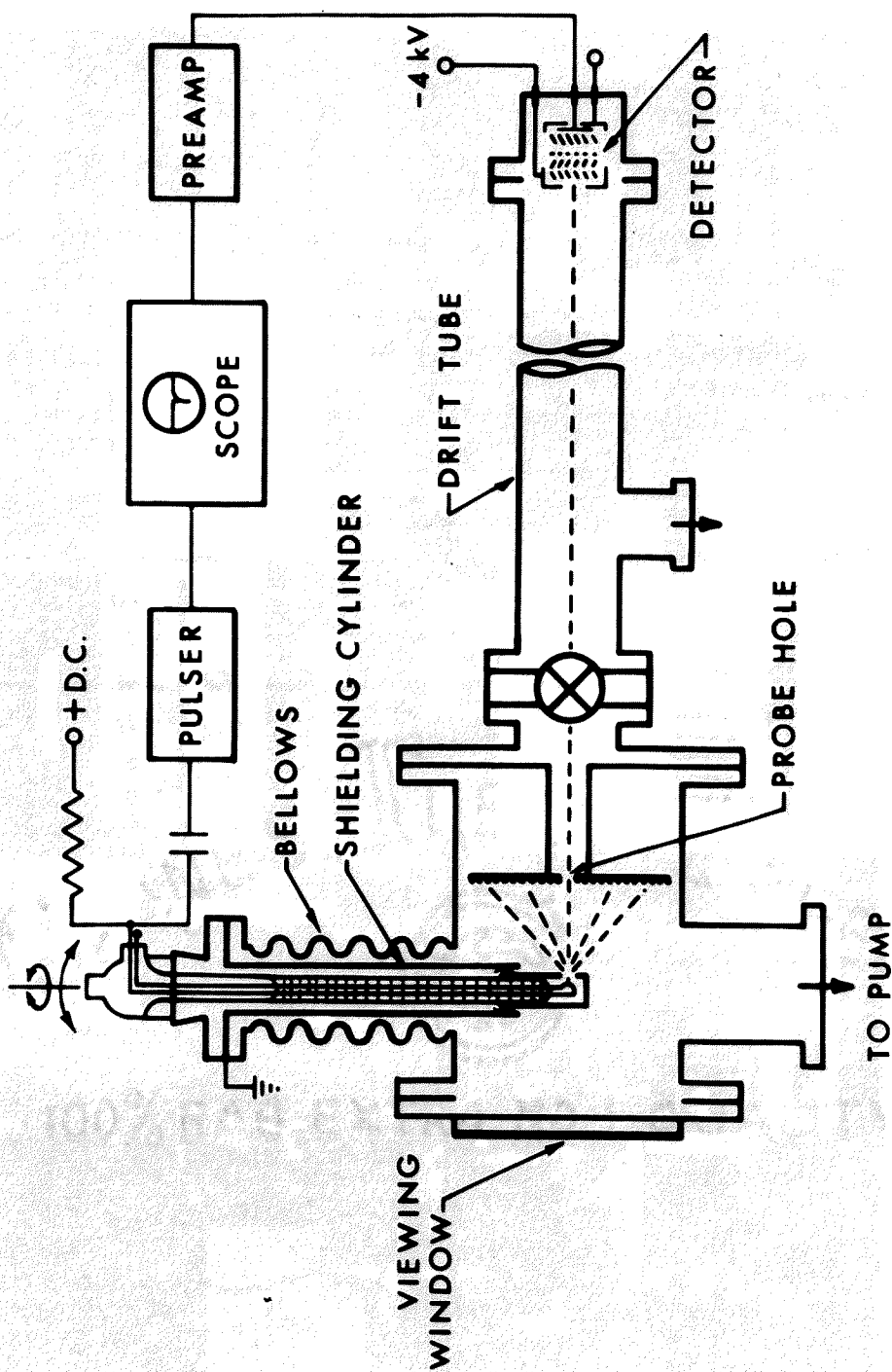


Figure 4. The Atom Probe Field Ion Microscope (Schematic)

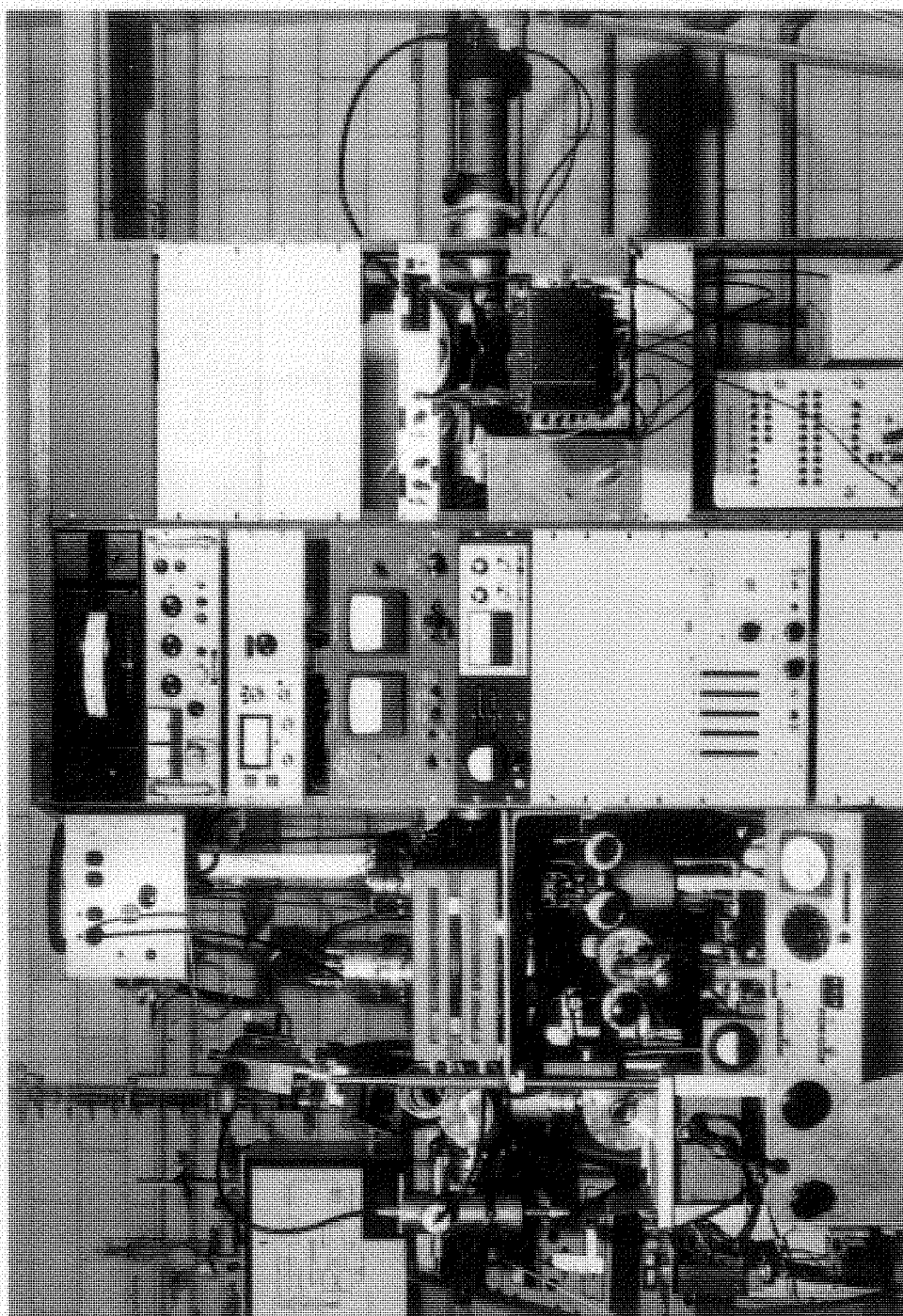


Figure 5. The Atom Probe Field Ion Microscope

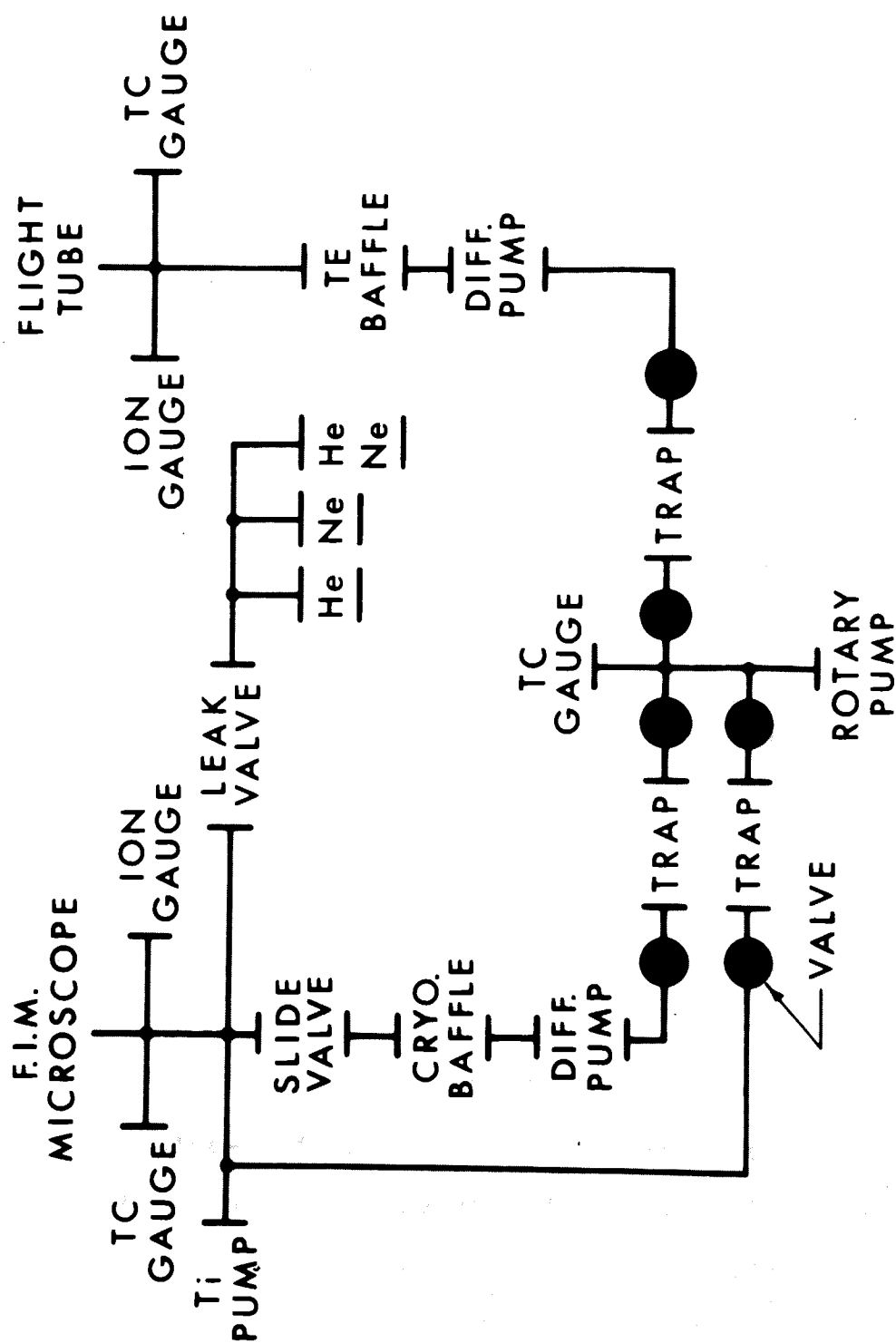


Figure 6. The Atom Probe Vacuum System (Schematic)

model 1283, high vacuum slide valve having a full aperture of 10 cm. An O-ring seals the valve to a 10 cm Granville Phillips "Cryosorb" liquid nitrogen trap. This trap, once filled, provides a positive barrier against diffusion pump oil creep. In addition, the surfaces exposed to the high vacuum remain cold even if the liquid nitrogen level in the reservoir falls appreciably. Practically, this means that contaminants will remain adsorbed even if the trap is left unattended for periods up to twelve hours. A 10 cm NRC oil diffusion pump, model NHS-4, is connected directly to the trap by another O-ring seal. A minimum area of each O-ring is exposed to the vacuum so that a typical background pressure of  $3.0 \times 10^{-8}$  Torr is easily obtained in the microscope after several hours of pumping. It should be noted that the actual pressure in the vicinity of the tip, which is almost entirely surrounded by the cold surface of a copper housing, is probably one order of magnitude lower when liquid hydrogen is used for cooling. The total pumping speed, limited by the conductance of the trap, is greater than 275 liters/sec.

The time-of-flight spectrometer is continually pumped by a 7.6 cm Edward's "Speedivac" oil diffusion pump, model E02. It is isolated from the pump by an Edwards thermoelectric (TE) baffle model DCB2A. The internal surfaces of the baffle are continually cooled  $10^\circ$  below cold water

temperature by thermoelectric elements. These are powered by a separate, well-regulated, DC power supply. This baffle has the obvious advantage of remaining at operating temperature without attendance. Typically, the pressure in the time-of-flight tube is less than  $2.0 \times 10^{-7}$  Torr.

A Pyrex gas supply manifold is connected to the microscope chamber through a Granville Phillips variable leak valve, series 203. Bottles of helium, neon, and helium-neon mixture are connected to the manifold through greased stopcocks. Both the helium and neon gas lines are provided with internal barium getters that were flashed before the bottles were initially opened. These getters provide a direct visual check on the purity of the gas remaining in each bottle, since the appearance of the active barium film changes rapidly upon contamination resulting from a leak.

Both the microscope and spectrometer are fitted with their own ionization gauge and controller, as well as a thermocouple (TC) gauge to monitor the foreline pressure of each diffusion pump. A thermocouple gauge on the high vacuum side of each pump completes the compliment of gauges.

## 2. Cold Finger Assembly:

The tip is spot welded to a 6.0 mil molybdenum wire loop which is inserted into two (20 mil I.D.) tungsten coils,

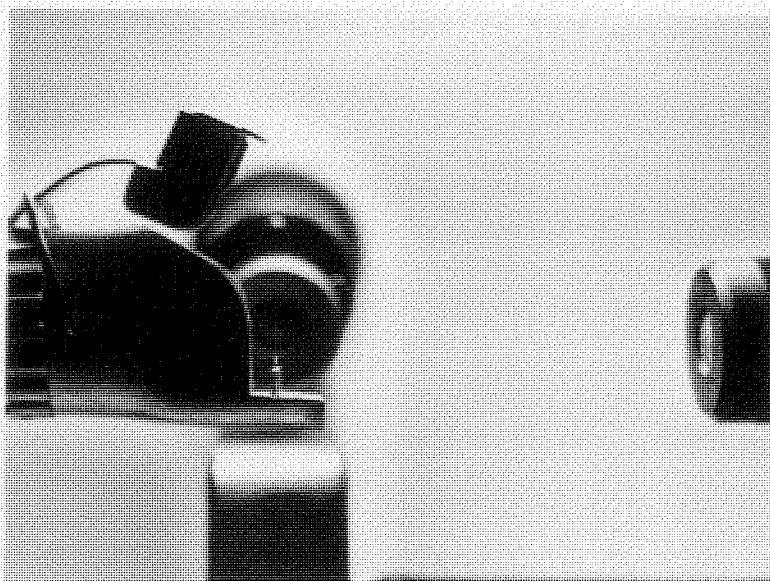
each formed at the end of a 20 mil tungsten wire. Each coil contains a "hairpin" of 8 mil tungsten wire which serves as a friction support for the molybdenum loop. With such a support the tip can be accurately adjusted and maintained at the correct orientation, in an alignment jig which will be described in section 6. The two 20 mil wires are sealed through the base of the cold finger, and extend to the upper portion of the microscope head where they connect with the high voltage DC and pulse supplies. The entire tip assembly is effectively cooled by conduction, since the tungsten wires pass through the cold finger which, during operation, is filled with a cryogenic liquid. The lower portion of the cold finger, showing the tip mounting details, is shown in Figure 7A. The tip positioning microscopes of the alignment jig are also shown.

A specially designed copper housing fits snugly around the base of the cold finger, and is cooled by conduction through its glass walls. In addition to increasing image brightness, this housing also serves to limit field penetration into the main microscope body. When the cold finger assembly is inserted into the microscope the copper housing contacts (by means of beryllium-copper leaf springs) a grounded copper cylinder which surrounds it. A small aperture in the housing permits the field evaporated ions to reach the screen. Figure 7B shows the base of the cold





A. Base of Atom Probe Cold Finger



B. Base of Atom Probe Cold Finger  
(Copper Housing Attached)

Figure 7. The Cold Finger Assembly and Alignment Jig.

finger with the housing attached, while Figure 8 shows the entire assembly inserted in the microscope body. Positioning of the specimen is effected by moving the bellows assembly and greased standard taper joint, around the axes shown in this figure. The copper housing is visible in the upper portion of the viewing window. The tip points away from the window toward the fluorescent screen. Note the complete electrical shielding of the cold finger assembly. Since the DC imaging voltage, and positive evaporation pulse travel to the tip entirely inside grounded enclosures, field penetration into the main body of the microscope is reduced to a negligible amount. Field penetration must be made as small as possible to insure that a well-defined ion trajectory, so critical to successful identification of preselected species, is achieved.

### 3. Image Observation and Photography:

During operation, a pair of modified 7 X 50 binoculars or a suitable camera is placed in front of the viewing window. Figure 9 shows the binoculars positioned to examine a small area ( $\sim 6 \text{ cm}^2$ ) around the probe hole. Once focused on the screen, the binoculars (or camera) can observe the faint FIM image without serious vignetting by the cold finger housing positioned directly in the optical path. This desirable situation results from the wide aperture optics employed. The cold finger housing is essentially

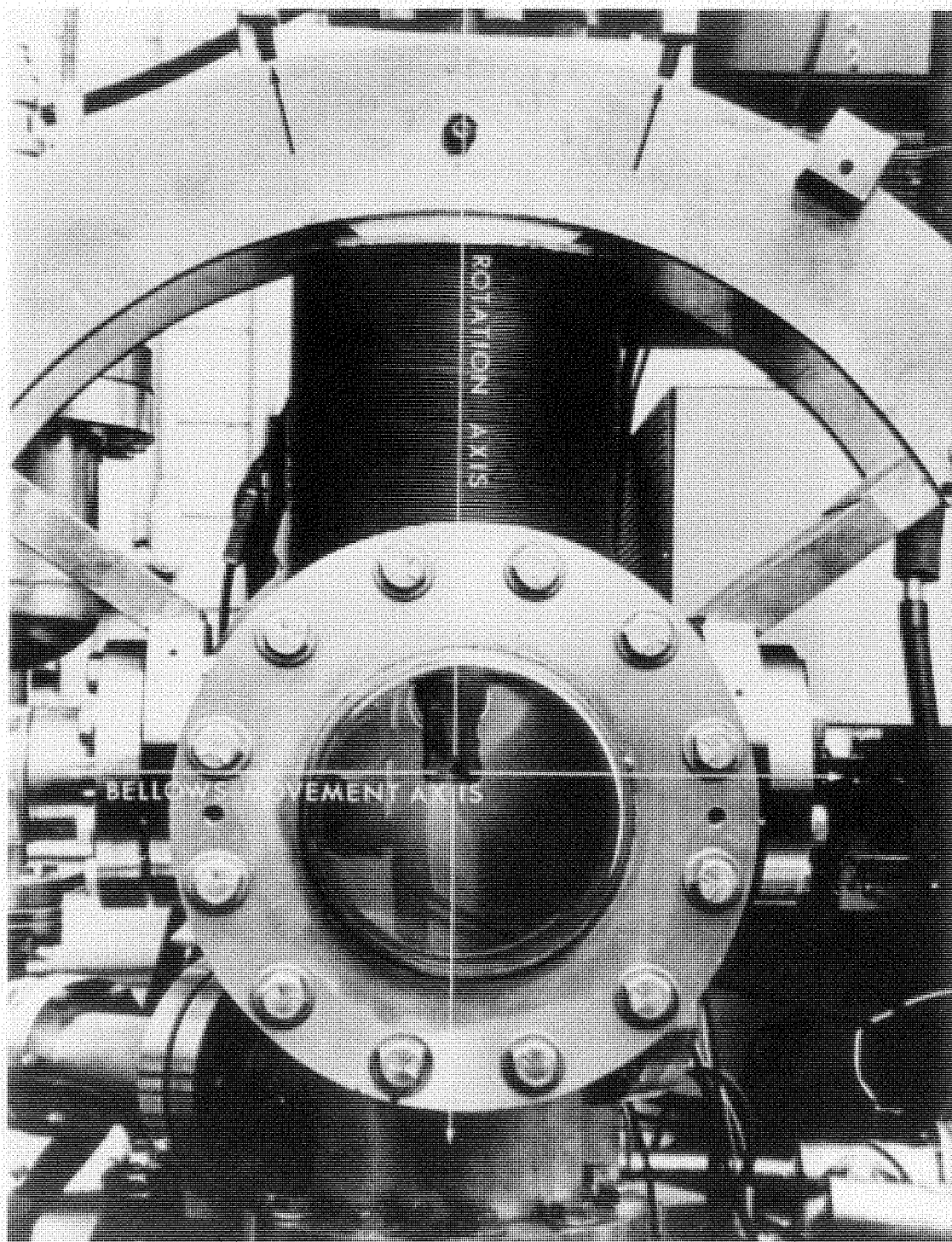


Figure 8. The Atom Probe Field Ion Microscope (Front View)

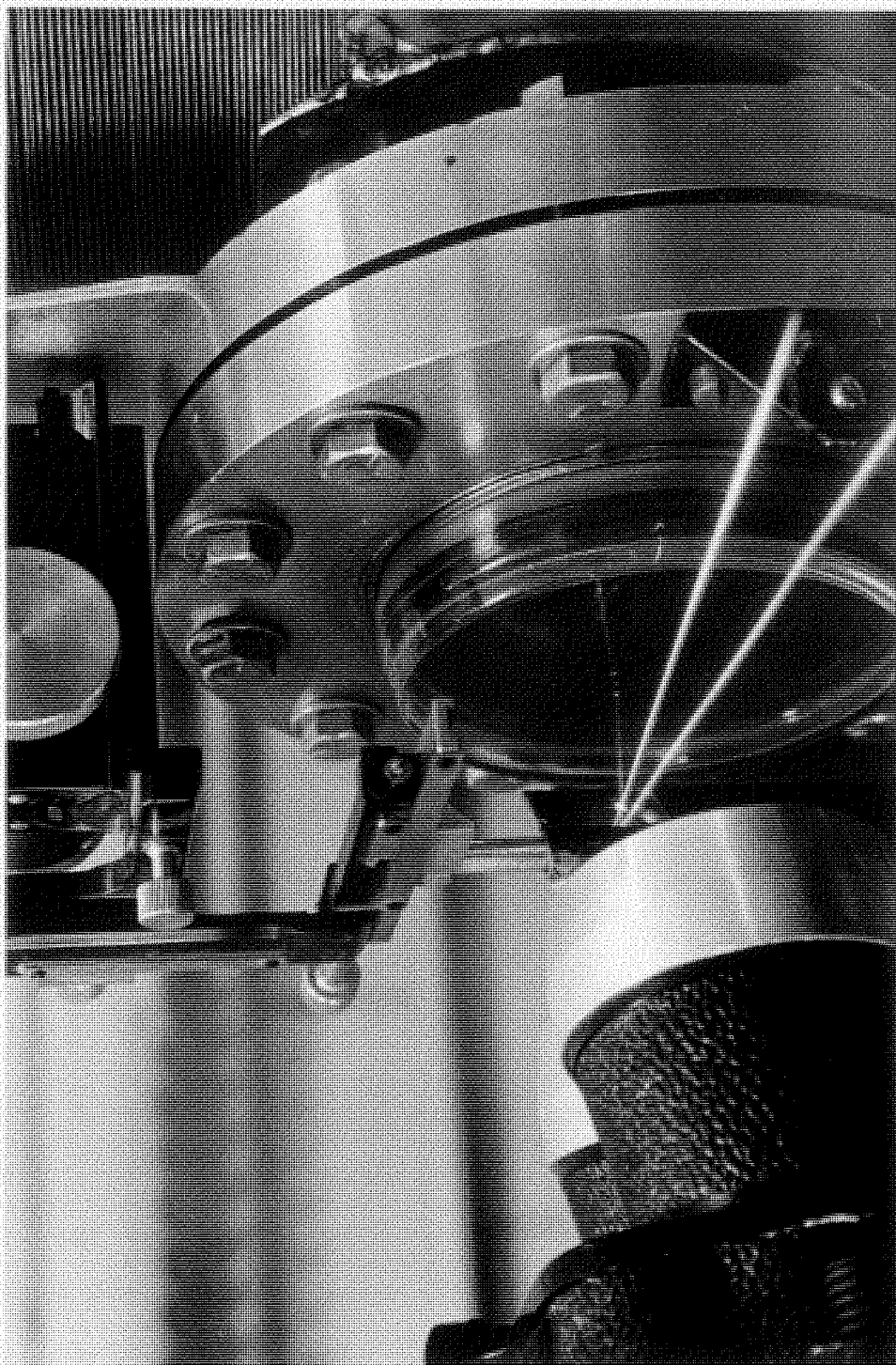


Figure 9. The Viewing Window and Binoculars

out of focus, the binoculars or camera effectively "seeing" around it.

Figure 10 shows the screen valve assembly used in the atom probe. The large flange bolts to the microscope body directly opposite the viewing window. A phosphor screen, dusted on a 60 mil aluminum plate, mounts on the D-shaped support shown in this figure. When mounted, the probe hole is located over the large aperture in the support. Two pins, passing through both the screen and support, position the screen positively so that it may be removed for redusting, and then replaced, without changing the probe hole alignment.

Figure 11 shows a field ion microscope image of iridium photographed in the atom probe. The probe hole intercepts the 7th ring of the central 001 plane at approximately the one o'clock position. As can be seen, no trace of the copper housing is visible. A modified Argus C-3 camera fitted with an F:0.87 (72 mm focal length) Super-Farron lens was used to obtain this photograph. Kodak type 103 aG spectroscopic film recorded the faint FIM image appearing on the phosphor dusted screen. The phosphor, manganese doped zinc ortho-silicate ( $\text{ZnSiO}_4:\text{Mn}$ ), is dusted onto the aluminum screen plate using a binder of 1 part glycerine and 9 parts alcohol. Before insertion, the plate is heated to 330°C to completely drive off any volatile



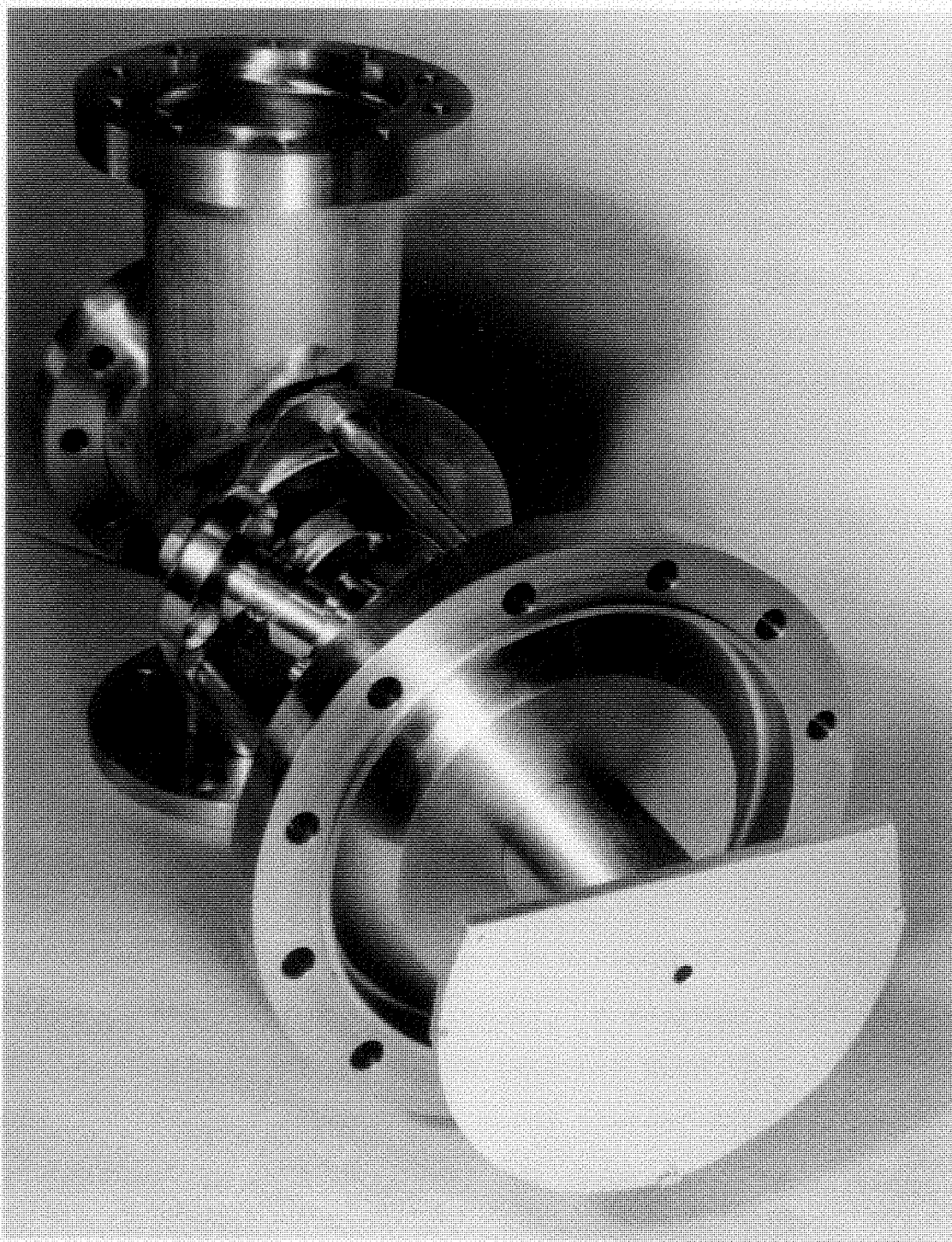


Figure 10. The Screen and Valve Assembly

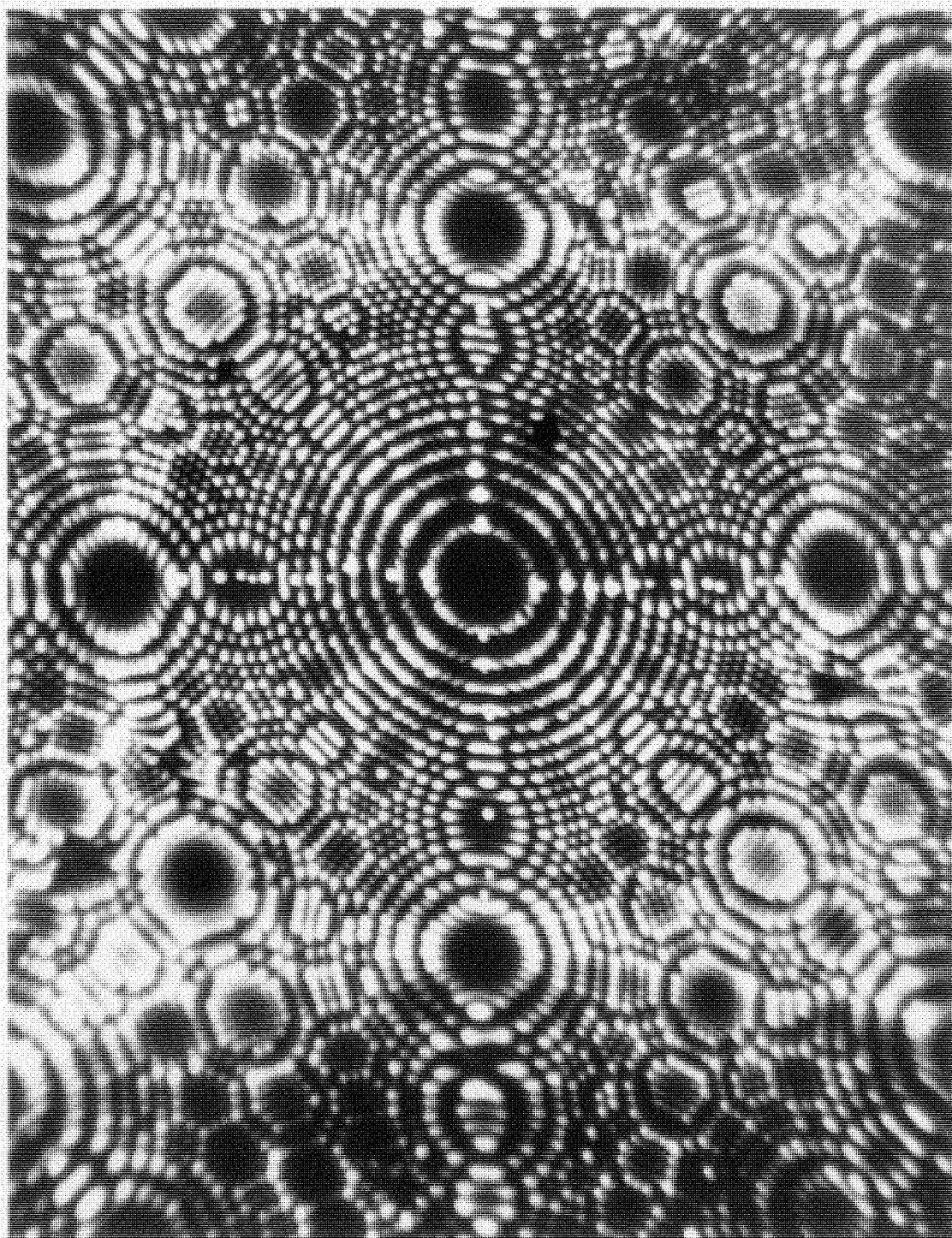


Figure 11. Iridium Imaged in Helium (8.55 kV)

vapors, and provide a screen of maximum efficiency for the imaging gas ions.

#### 4. Ion Detector:

The ion detector used in the atom probe must be capable of detecting single particles, while responding to their impact in times shorter than those corresponding to the difference in the travel times of adjacent masses of 1 amu separation. This "response time" may be estimated by direct differentiation of equation (3):

$$\Delta t = \frac{\Delta \left(\frac{m}{n}\right)_0}{2 \left(\frac{m}{n}\right)_0} \tau \quad (4)$$

using equation (3) to eliminate  $\tau$  gives:

$$\Delta t = \frac{\Delta \left(\frac{m}{n}\right)_0}{2 \sqrt{K V_{\text{total}} \left(\frac{m}{n}\right)_0}} \quad (5)$$

The worst case corresponds to the minimum time difference which occurs for  $\sqrt{K V_{\text{total}} \left(\frac{m}{n}\right)_0}$  a maximum. Consider 20 KV, doubly charged iridium isotopes with  $\left(\frac{m}{n}\right)_0 = 191/2$ , and  $\left(\frac{m}{n}\right)_0 = 193/2$ . For a two meter time-of-flight tube,  $K = 0.049$ . Since  $\Delta \left(\frac{m}{n}\right)_0 = 1$ , the required response time is, from equation (5), just:

$$\Delta t \text{ (}\mu \text{ seconds)} = \frac{1}{\sqrt{4 (.049) (20) (193/2)}} \approx 0.05$$



An additional requirement is that the active area of the detector must be as large as possible to insure that ions are detected even if they do not travel exactly on the axis of the instrument. Consider a two meter flight path, and a probe hole of 1.0 mm diameter. An ion which originates on the instrument axis, and travels to the detector in a straight line path will arrive 1.2 cm from the axis if it just clears the edge of the probe hole. This straightforward calculation assumes a tip-to-probe hole distance of 8.0 cm. Practically, this result means that the minimum active detector area should correspond to a circle of at least 1.2 cm radius, centered on the instrument axis.

The three considerations mentioned: single particle sensitivity, 50 nanosecond response time, and  $4.5 \text{ cm}^2$  active area, suggest some form of electron multiplier ion detector. The device finally chosen, a 14 stage copper-beryllium "venetian-blind" electron multiplier with  $\sim 6.0 \text{ cm}^2$  of active area was constructed from parts supplied by EMI (Electrical and Musical Industries) of London, England.

The gain,  $G$ , of such a device depends upon the number of active stages, or dynodes, used, as well as their secondary electron emission coefficient  $\sigma$ . By definition,  $\sigma$  is the number of secondary electrons released per incident

primary particle. For  $n$  stages, the gain is just:<sup>20</sup>

$$G = \sigma^n, \quad (6)$$

where  $\sigma$  depends upon the energy of the incident particle, the material from which the dynodes are constructed, and the condition of the dynode surface. For properly prepared<sup>21</sup> Be-Cu dynodes, with 200-375 volts applied between each pair,  $\sigma \sim 3$ . Although  $\sigma$  increases with increasing primary particle energy (and, therefore, with increasing interdynode potential), breakdown between stages usually limits the maximum applied voltage per stage to those given above.

The secondary emission coefficient  $\sigma$  can be even larger for the first dynode which is struck by the field-evaporated ions, with energies always greater than 4.0 kV. Allen,<sup>22</sup> in fact, notes that for positive ions with energies greater than 4.0 kV detection efficiency, using such a multiplier, should be very close to 100%. The yield of secondary electrons released by ions with energies greater than 4 kV is essentially constant. For Be-Cu the secondary electron coefficient for such ions, as given by Allen<sup>23</sup> may reach 8 or 10 for properly activated surfaces. If  $\sigma_1$  is defined as the secondary electron coefficient of the first dynode, and  $\sigma$  the secondary electron coefficient of the remaining  $(n-1)$  dynodes, the gain becomes, for a

fourteen stage multiplier,

$$G = \sigma_1 \sigma^{(n-1)} \approx 8.3^{13} \approx 10^7 . \quad (7)$$

The actual number of secondaries emitted per dynode, and therefore the actual pulse height observed is, of course, a statistical quantity. Fortunately, the mass determination of field-evaporated ions does not depend on the magnitude of the pulse height, but only on the time when the pulse appears.

An order of magnitude calculation for the expected pulse amplitude, due to the impact of a single positive ion with the multiplier, may be obtained as follows: By definition, the gain of a multiplier is the ratio of the output to the input current; or, equivalently, the ratio of the output to the input charge. If a doubly charged ion strikes the first dynode of a multiplier of gain  $G$ , the resulting output charge will be:

$$Q = 2eG \quad (8)$$

where  $e$  is the electronic charge. Assume that the multiplier is connected by a line of negligible impedance to an oscilloscope of input impedance  $Z$ . If  $Z \approx j\omega C$ , where  $C$  is the input capacitance, the voltage developed across this

capacitance as a result of the charge  $Q$  will be:

$$V = Q/C = 2eG/C = (3.2 \times 10^{-19}) G/C \quad . \quad (9)$$

For a modest multiplier gain of  $10^6$  and an input capacitance of twenty picofarads (the input capacitance of a Tektronix type 454 oscilloscope), the recorded voltage would be:

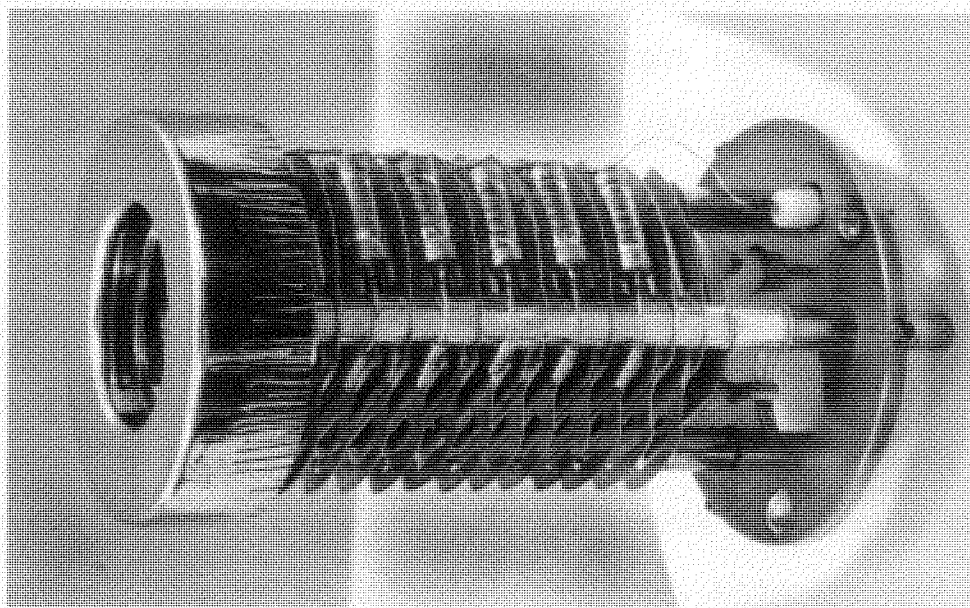
$$V = (3.2 \times 10^{-19}) (1.0 \times 10^6) / (20.0 \times 10^{-12}) \approx 20\text{mV} \quad .$$

Typical noise levels would be below one millivolt, so that such an amplitude is quite sufficient for satisfactory pulse discrimination. In practice, an MOS-FET preamp, having a voltage gain of one, is connected directly to the multiplier. The preamp serves, primarily, to match the high output impedance of the multiplier to the low input impedance of the coaxial cable which carries the signal to a Tektronix type 454 oscilloscope. An average pulse amplitude of 30mV is typical during actual operation.

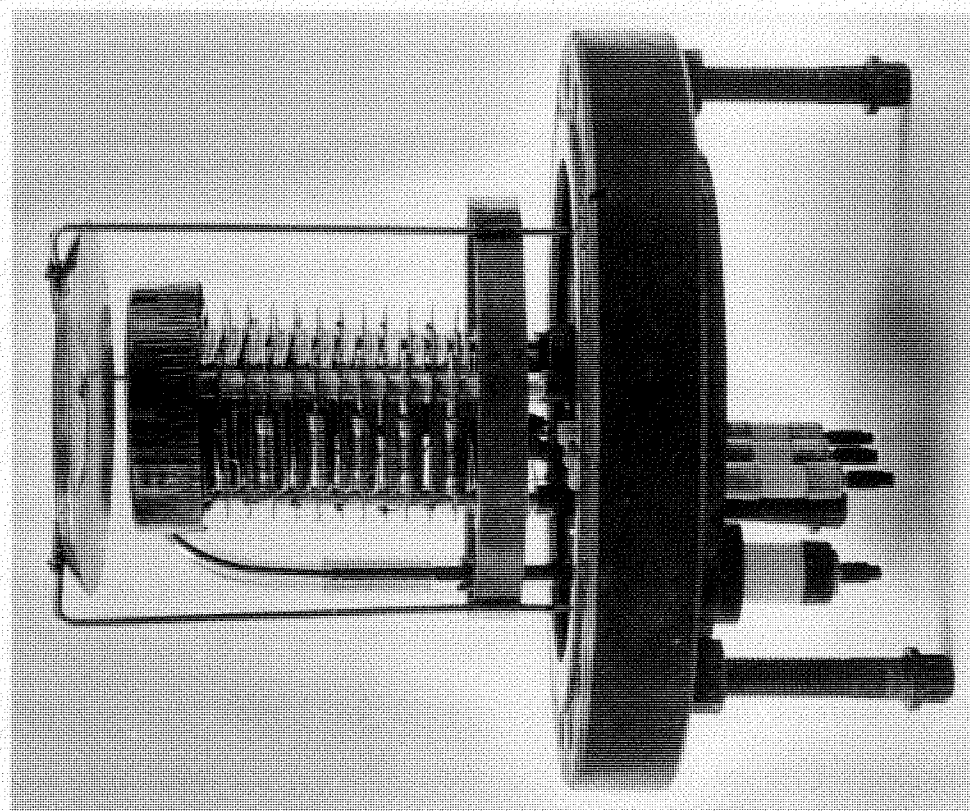
Since the sweep of the oscilloscope is triggered by dynodes, as well as by the multiplier output, the evaporation pulse, and the sweep lasts for only ten or to appropriate ceramic seals. A typical gain, however, twenty microseconds, random noise at the output is reduced by capacitors and connected externally to the multiplier to completely negligible amounts. For the same reason, completes the circuit when the multiplier dark current of, typically, one pulse per appropriate materials. At a rate of one pulse per second is unobservable.

The completed fourteen-stage ion detector is shown in Figure 12A. Fourteen beryllium-copper dynodes, and one anode, are stacked on three ceramic rods, and separated from each other by Pyrex spacers. The entire assembly is spring loaded (with copper flashed Inconel springs) and fastened, rigidly, to a stainless steel base, which bolts to a stainless steel flange located at the end of the flight tube. Figure 12B shows the multiplier-flange assembly. A grounded wire mesh, supported over the first dynode, is also shown. The flange, as shown, contains the ceramic-to-metal seals which carry the electrical signals from the multiplier, and the electrical power to it. The multiplier assembly actually plugs into these seals, so that installation and removal is quite convenient.

The dynodes are maintained at appropriate potentials by an in-situ resistor chain of 2.0 megohm deposited film resistors manufactured by Pyrofilm Incorporated, of New Jersey. The chain of resistors extends from the first to the thirteenth dynode, the thirteenth and fourteenth dynodes, as well as the anode cup being connected directly to appropriate ceramic seals. A resistor chain, by-passed by capacitors and connected externally to these seals, completes the circuit which maintains the dynodes at appropriate potentials. An electropolished nickel cap covers the first three dynodes. It is maintained at the same



A. The Electron Multiplier



B. The Detector Flange

Figure 12. The Electron-Multiplier Detector

potential as the first dynode (-4000 volts DC), and serves to suppress field emission from possible sharp edges on those initial dynodes held at large negative DC potentials.

Before initial use and after prolonged use, the electron multiplier must be baked in vacuum to activate its secondary emission surfaces.<sup>24,25</sup> To accomplish this in situ, a furnace is placed around the end of the time-of-flight tube containing the detector. With the system under vacuum, the furnace temperature is maintained at 500°C for one-half hour, and then allowed to decrease, slowly. During the bake-out procedure the system pressure is always kept below  $8.0 \times 10^{-5}$  Torr. Alternately, the multiplier may be activated in an auxiliary vacuum system by heating the dynodes to a dull red color with an R.F. generator. When cool, the multiplier is mounted on the detector flange and inserted into the time-of-flight tube. Exposure to the atmosphere reduces the secondary emission coefficient of the dynodes, and therefore must be minimized.

## 5. Electronics:

Figure 13 contains a schematic diagram of the transistorized FET preamplifier designed by S. B. McLane for use with the electron multiplier previously described, which is also shown in this figure. The input impedance of the preamp is greater than  $10^8$  ohms and, when coupled to the vertical amplifier of a Tektronix type 554 oscilloscope,

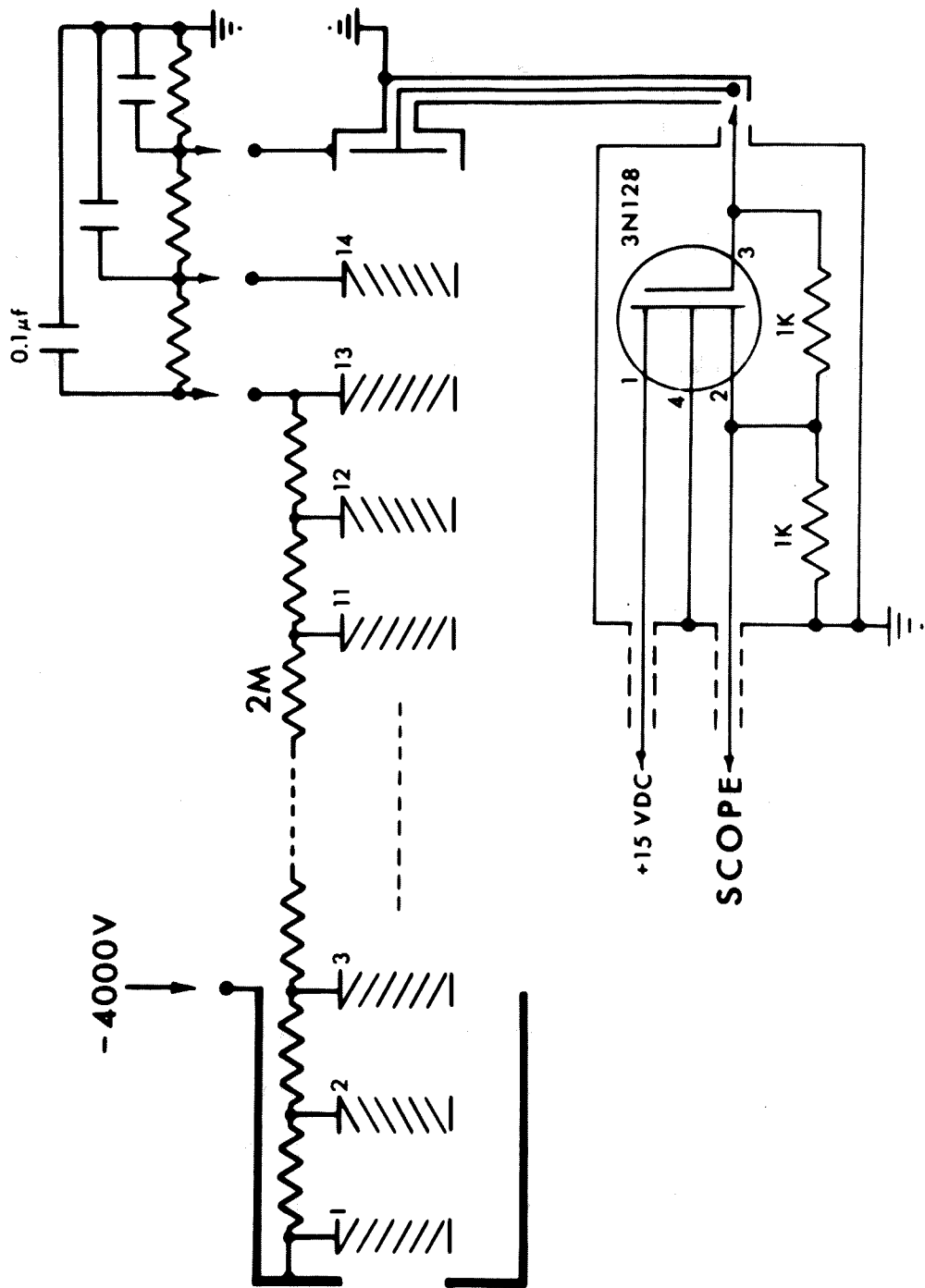


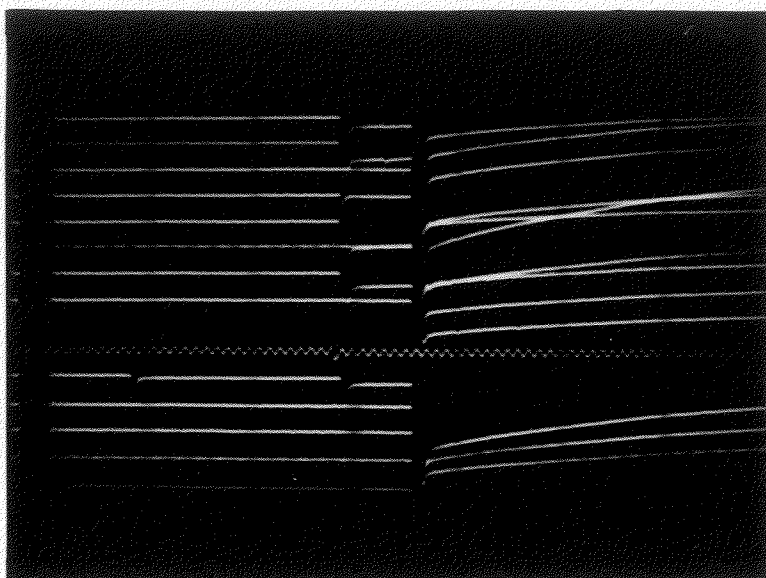
Figure 13. The Multiplier-Preamplifier Schematic



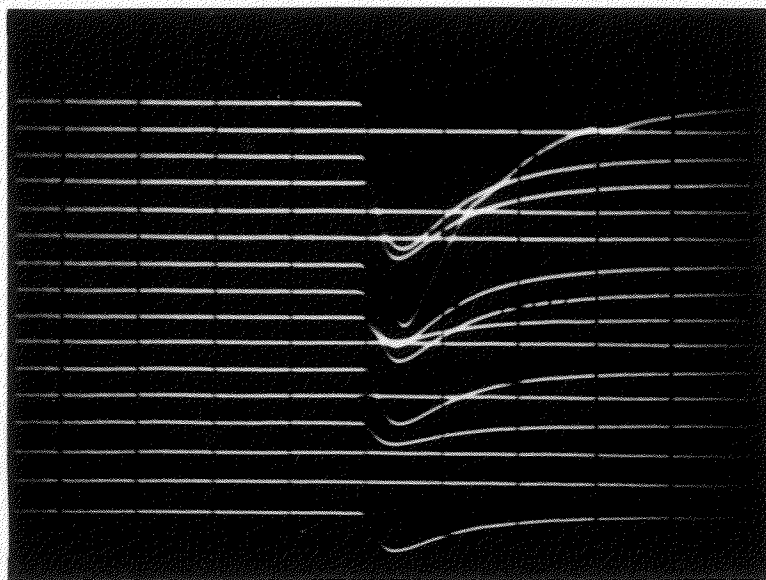
provides for single particle detection. Examples of typical pulses obtained during an experiment with rhodium appear in Figure 14.

The preamplifier is attached externally to the appropriate ceramic feedthrough on the detector flange. A 50 $\Omega$  cable connects its low impedance output to one channel of the dual channel vertical amplifier of a Tektronix type 554 oscilloscope. The other channel is connected to a stepped DC power supply, and both channels are added, algebraically. This arrangement allows the position of the trace appearing on the scope face to be shifted by precise amounts, by stepping the applied DC voltage. In such a manner many equally spaced, consecutive traces can be recorded on a single photograph.

The sweep of the oscilloscope is initiated by a pulse from a transistorized multivibrator, triggered by a signal from the pulse generator which provides the evaporation pulse. The pulse generated by the multivibrator is also displayed on each trace providing a convenient zero reference marker from which to measure time. Such a marker of fixed amplitude and duration is displayed in preference to the actual trigger pulse from the pulse generator because the trigger pulse amplitude and width are not constant, but vary markedly with changes in pulse voltage, amplitude and duration.



A. Rhodium at 14.8kV + 2.0kV pulse



B. Rhodium at 15.3kV + 1.6kV pulse

Figure 14. Atom Probe Examination of Rhodium

In addition to the pulse triggered traces which appear on each photograph, a time calibration sweep can be displayed if desired. This sweep, obtained from a Tektronix type 180A oven-controlled crystal oscillator, provides a means for measuring time independent of the setting of the oscilloscope's time base generator. In practice, the linear distance on each recorded sweep between the initial marker pulse, and the pulse of interest, is measured. The number of cycles of the time sweep appearing within the same distance is the ion's time of flight, less correction for any electronic delay time introduced by the detection or triggering circuitry. Since the atom probe can be calibrated by techniques to be described shortly, the actual time delay introduced by the electronic circuitry can be determined. Provided it is a constant of the apparatus, time-of-flight measurements become simple and accurate.

By using the Tektronix 554's option of expanding in time any preselected portion of a given time sweep, a great improvement in the accuracy of the time-of-flight measurement is obtained, especially if a time sweep from the oscillator is likewise displayed. The Tektronix 180A crystal oscillator produces 5, 10, 20, and 50 Mhz signals, so that one appropriate to the measurement can usually be chosen.

#### 6. Alignment:

In order to insure that a field evaporated ion is

detected the tip, probe hole, and detector must lie, and remain, on a common axis. But during operation the tip must usually be moved to position the image of a selected species over the probe hole. If, during this movement, the tip's spatial position changed by only 0.1 mm, alignment would suffer and, in all probability, the evaporated ion although passing through the probe hole would not strike the detector.

To insure that alignment is preserved during tip movement, the tip is positioned as closely as possible to the intersection point of the rotation axis and the axis about which the bellows can move (See Figures 4 and 8). When the instrument was constructed, this point was chosen to lie on the time-of-flight tube (or instrument) axis, approximately 8.0 cm from the fluorescent screen, and in the microscope body. Adjustment screws (shown by black arrows in the upper portion of Figure 8) allow the rotation axis to be selectively oriented with respect to the vertical, causing it to intersect the horizontal bellows axis. The intersection point, which determines the tip location, will be called the "center of rotation" for convenience.

In practice, to align the instrument, the center of rotation is determined first. This point and the center of the detector flange define the "effective" axis of the instrument, which is essentially coincident with the

time-of-flight tube axis. The screen is then positioned so that the probe hole is centered with respect to the effective axis. Two different techniques were developed to align the atom probe. Each has its own advantages and disadvantages, but either will permit the instrument to be accurately aligned.

Alignment method #1--The cold finger assembly, including the greased joint and matching flange, is rigidly fastened in an "alignment jig" which permits the tip to be viewed by two low power microscopes: one aligned with the cold finger axis, and one at right angles to it. Figures 7A and 7B show these microscopes, which are equipped with circular reticles 0.3 mm in diameter, as well as the base of the cold finger assembly.

The tip is rotated by turning the greased joint, and viewed in the axial microscope. Its position is changed with the aid of tweezers until its very end remains stationary during rotation. When such a condition occurs, the tip lies on the rotation axis of the cold finger. Both microscopes are now adjusted until the end of the tip appears centered in the reticle of each. The adjustment of these microscopes, once made, permits any other tip to be positioned at the same spatial point by centering it in each reticle. Next, the tip is removed, and replaced with

an etched "hairpin" shaped filament whose end is centered in the reticles. The cold finger is inserted into the instrument, the detector flange replaced with a ground glass screen, and the entire atom probe rough pumped to about one micron. After filling the cold finger with liquid nitrogen, and opening the valve between microscope and spectrometer, an electric current is passed through the hairpin filament. If it was properly made, only its very end will become incandescent approximating, quite closely, a point source of light. The cold finger is rotated and the image of the probe hole, projected by the illuminated filament on the ground glass, is observed. If the filament was originally positioned on the rotation axis and did not move during insertion or heating, the image will remain stationary. The bellows assembly is now moved and the adjustment screws turned until the image remains stationary during this movement. When the image position remains unchanged during any combination of these movements, the center of rotation has been found. The instrument is shut down, and the cold finger removed and reinserted into the alignment jig. Final, precise microscope positioning is effected by centering the reticles on the end of the filament. Following this, the cold finger is reinserted in the atom probe and the position of the tip again checked by watching for image motion on the ground glass. If the

image remains stationary, but is not centered on the ground glass, the probe hole position must be adjusted by trial and error until the image is centered. This procedure, although tedious, completes the alignment.

Alignment method #2--The beam of a CW laser is projected through both the main window of the atom probe, and the probe hole. Its position is adjusted until it strikes the center of a ground glass positioned in place of the detector flange. Symmetry of the resulting laser pattern insures that the probe hole is not vignetting the beam. The instrument is rough pumped during this procedure. Figure 9 shows the laser beam directed, by a mirror mounted on a micromanipulator, through the main atom probe window. The binoculars used to view the immediate area surrounding the probe hole are also shown. This laser beam, once positioned to pass through the probe hole and intercept the center of the detector flange, defines the effective axis of the instrument.

A tip is positioned in the alignment jig as described in the first method, and the cold finger inserted into the instrument. The screen is replaced by another screen, at the same position, having a piece of millimeter graph paper mounted on it. A small cross on the graph paper shows the location of the probe hole. Great care is taken to

insure that the position of the laser beam is not disturbed during these operations. The cold finger assembly is now moved while watching the shadow of the tip produced by the laser on the millimeter paper. As in the first method rotation is checked, and the screws are adjusted until the image remains stationary during bellows movement. In addition, the very edge of the tip's image must lie on the mark indicating the probe hole's position. If this is not the case, the position of the tip's image must be noted, a new probe hole drilled, and the entire procedure repeated. Finally, when the image is stationary and located over the probe hole's marked position, the actual screen is reinserted and the laser beam position on the ground glass rechecked. If it is accurately centered, the alignment is completed.

It is perhaps worthwhile to mention that both procedures, when carefully followed, allow the tip to be aligned well within the necessary tolerance. The first method is perhaps more accurate since a greatly magnified image is observed at the detector flange itself. Unfortunately, satisfactory "point source" filaments are difficult to make, and often move during heating. If a filament does move, it must be repositioned in the alignment jig. The second method relies upon the shadow image of the tip on the screen. Although the magnification is not as great as



if the image were observed at the detector flange, it is quite sufficient. The second procedure is probably simpler than the first unless the probe hole needs to be repositioned. In general, the first method is preferred for initial alignment, and the second for subsequent checking or realignment.

## V. PERFORMANCE OF THE INSTRUMENT

### 1. Further Theoretical Considerations

Equation (3), used to calculate the masses observed in the prototype instrument, was derived using several assumptions not all of which are satisfied in practice. Because of the relatively crude apparatus, and the inexperience associated with the introduction of any new instrument, such approximations, at the time, seemed reasonable. Now, as a result of using the new instrument, these assumptions must be re-examined.

If the evaporation pulse terminates before the evaporated ion has acquired its full kinetic energy, equation (1), the true mass-to-charge ratio will not be given by equation (3). To calculate the error made by using this equation in such a situation assume that at the instant the evaporated ion has traveled a distance  $d$  from the tip, the evaporation pulse terminates. If the spatial potential at  $d$  was  $V$ , before the pulse terminated, and  $(V - \Delta V)$  after, the ion's final kinetic energy will be:

$$\frac{1}{2} m v_t^2 = ne (V_0 - V) + ne [(V - \Delta V) - 0] = ne (V_0 - \Delta V) \quad (10)$$

where  $m$  is the mass of the ion,  $v_t$  its terminal velocity,  $ne$  its charge,  $V_0$  the total potential at the tip before the pulse terminated, and  $\Delta V$  the change in potential, at  $d$ , resulting from the pulse termination.

The change in potential,  $\Delta V$  may be calculated by assuming a paraboloidal geometry, and using equation (A-16) for the resulting potential. Identifying in that equation  $V_o = V_{\text{pulse}}$ ,  $z = (d + z_o)$ , and  $R = 2z_o$ , the kinetic energy of the ion becomes:

$$\frac{1}{2} m v_t^2 = n e V_o \left( 1 - \frac{\Delta V}{V_o} \right) = n e V_o (1 - C) \quad (11)$$

where:

$$C \equiv \frac{V_{\text{pulse}}}{V_o} \frac{\ln \left( \frac{d + z_o}{z_1} \right)}{\ln (z_o / z_1)} = \frac{V_{\text{pulse}}}{V_o} \frac{\ln \left( \frac{2d + R}{2z_1} \right)}{\ln (R / 2z_1)} \quad (12)$$

Then the observed travel time is just:

$$t^2 = \frac{d^2}{v_t^2} = \frac{m}{n} \frac{d^2}{2eV_o (1 - C)} \quad (13)$$

Since this is an experimentally observed parameter, substitution of equation (13) into equation (3) will allow the mass-to-charge ratio to be calculated. The result is:

$$\left( \frac{m}{n} \right)_o = \frac{2e}{d^2} V t^2 = \frac{m}{n} \frac{1}{(1 - C)} \quad (14)$$

whereas, if the pulse duration was made sufficiently long, the ion would be fully accelerated and equation (3) would predict the actual mass-to-charge ratio. That is, it would predict:

$$\left(\frac{m}{n}\right)_0 = \frac{m}{n} \quad (15)$$

These results indicate that if the pulse terminates before the ion is fully accelerated, the mass-to-charge ratio predicted by equation (3) would be larger by a factor  $(1 - C)^{-1}$  than the ratio predicted by equation (3) if a sufficiently long pulse was used. The percent difference between these results is given by:

$$\% \text{ diff} = \frac{\left(\frac{m}{n}\right) \frac{1}{1 - C} - \left(\frac{m}{n}\right)}{\left(\frac{m}{n}\right)} \times 100 = \frac{C}{1 - C} \times 100 \quad (16)$$

Assume that the pulse terminates after the ion has traveled only one-half of the tip to ground electrode distance  $z_1$ , where  $z_1 = 0.001\text{m}$ . For a  $504\text{\AA}$  tip radius (12kV tip), the differences corresponding to  $\frac{V_{\text{pulse}}}{V_0} = 0.1, 0.2, \text{ and } 0.5$  are, respectively: 0.6%, 1.3%, and 3.4%. If the tip radius,  $R$ , is  $322.2\text{\AA}$  (8kV tip), the corresponding percent differences are essentially the same, since the correction factor  $C$  is insensitive to such a change of tip radius.

These results have been verified, experimentally, by evaporating a single isotope metal, rhodium, in vacuum,

and comparing the  $m/n$  values calculated from equation (3), when either a two or a twenty nanosecond evaporation pulse was used. Worst case calculations using the results of Appendix A, indicate that a two nanosecond pulse duration (as used with the prototype instrument) is much shorter than the ion's travel time in the acceleration region near the tip, while a 12ns pulse is longer, for any ion and tip radius of interest. Although the two nanosecond pulse is too short to allow the evaporated ion to acquire the full kinetic energy, given by equation (11), the consistency and magnitude of identical species flight times indicate that the actual evaporation event must take place within the first nanosecond after applying the pulse. As a result of these considerations, an 18ns pulse having a rise time of 0.33ns is currently being used. The rise time of the pulse must obviously be small compared to its duration to insure that the ion, upon evaporation, will encounter a potential equal to the sum of the DC imaging voltage, and the maximum amplitude of the evaporation pulse.

If the ion does acquire the full kinetic energy,  $(ne)(V_{dc} + V_{pulse})$ , but travels for only part of its remaining path in field free regions, and then encounters an attractive potential, equation (3) must be modified. Such an attractive potential exists in the immediate vicinity of the multiplier detector due to the relatively large DC

potential applied to the first dynode and shielding cap. The resulting field accelerates the approaching ion, causing its travel time to be shorter than predicted by equation (2). The effect of this additional acceleration on the travel time can be predicted, theoretically, if the exact potential distribution in front of the multiplier is known. Since the imposing geometry makes a first principle solution difficult, a dimensionally exact model of the detector and time-of-flight tube was constructed in an electrolytic trough. The resulting potential distribution was measured along the multiplier axis, and the results are shown in Figure 15. The circles appearing in Figure 15 are estimates of the experimental error associated with each measured point. For convenience, the multiplier cap is drawn with the same scale chosen for the x-axis.

A fifth degree polynomial was fitted to the experimental data by use of a digital computer program, and the exact form of the polynomial was obtained by computer plotting for 200 values of the independent variable. Figure 15, whose axes and data points were computer plotted, shows, as a solid line, this polynomial. Its exact form is:

$$\begin{aligned} \frac{V(x)}{V_d} = & 1.000000 - (1.817831 \times 10^{-1})x \\ & - (2.698437 \times 10^{-2})x^2 + (1.062603 \times 10^{-2})x^3 \\ & - (1.083624 \times 10^{-3})x^4 + (3.734131 \times 10^{-5})x^5 \quad (17) \end{aligned}$$

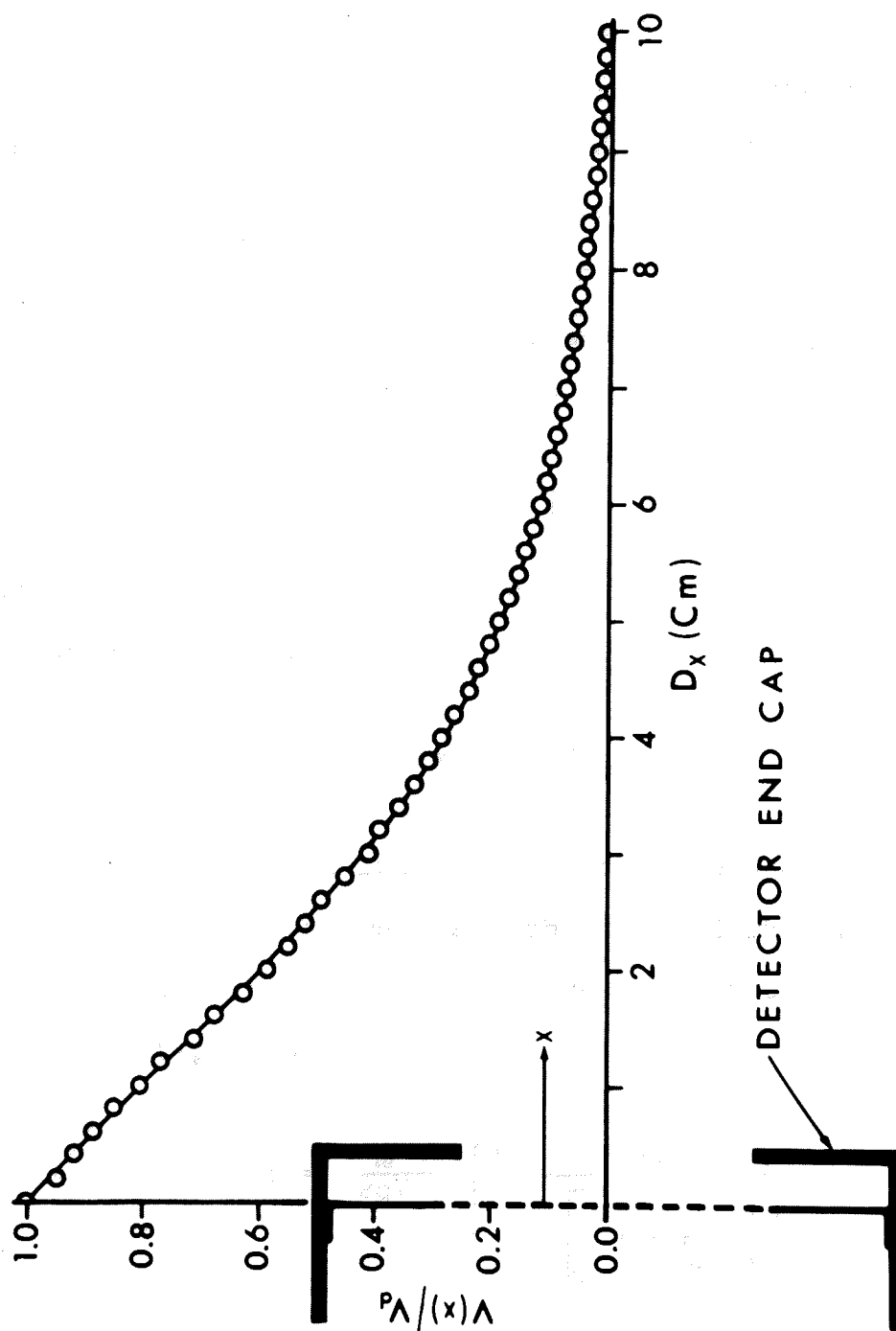


Figure 15. The Axial Multiplier Potential

Since it is expected that ions will travel to the multiplier on, or quite near the axis, only axial distances measured from the multiplier cap need to be considered. Let  $d$  be the cap-to-tip distance;  $d_0$  the distance from the cap to a point in space, along the axis, where the multiplier potential is effectively zero; and let  $x$  be the axial position of the ion in front of the multiplier cap. With  $V_0$  defined as the total tip voltage,  $(V_{dc} + V_{pulse})$ , the kinetic energy of the ion, at position  $x$ , is just:

$$\frac{1}{2} mv(x)^2 = q [V_0 + V(x)] \quad (18)$$

where  $v(x)$  is its instantaneously velocity and  $V(x)$  the potential at point  $x$ . But:

$$v(x) = - \frac{dx}{dt} \quad (19)$$

where the minus sign indicates that the distance of the ion from the detector decreases with time. Combining equations (18) and (19) and integrating gives, for the total travel time from tip to detector:

$$\tau = \frac{m}{2qV_0} \int_0^d \frac{dx}{\left[ 1 + \frac{V(x)}{V_0} \right]^{\frac{1}{2}}} \quad (20)$$



Squaring equation (20) and solving for  $m/n$  yields:

$$\frac{m}{n} = \frac{2eV_0 \tau^2}{d^2} \left[ \frac{1}{d} \int_0^d \frac{dx}{\left[ 1 + \frac{V(x)}{V_0} \right]^{\frac{1}{2}}} \right]^{-2} \quad (21)$$

But  $\tau$  is an experimental parameter measured on the oscilloscope. Previously, the mass-to-charge ratio was calculated from equation (3) which gave:

$$\left( \frac{m}{n} \right)_0 = KV\tau^2 = \frac{2e}{d^2} V_0 \tau^2 \quad (22)$$

combining equations (21) and (22) allows  $m/n$ , the correct mass-to-charge ratio, to be expressed in terms of  $(m/n)_0$ , the previous ratio. That is:

$$\frac{m}{n} = \frac{2eV_0 \tau^2}{d^2} \beta = \left( \frac{m}{n} \right)_0 \beta \quad (23)$$

where  $\beta$ , the mass correction factor, is given by:

$$\beta \equiv \left[ \frac{1}{d} \int_0^d \frac{dx}{\left[ 1 + \frac{V(x)}{V_0} \right]^{\frac{1}{2}}} \right]^{-2} \quad (24)$$

But the potential  $V(x)$  is, by definition, negligible (i.e., zero) from  $d_0$  to  $d$ . This allows equation (24) to be rewritten:

$$\beta \equiv \left[ \frac{1}{d} \int_0^{d_0} \frac{dx}{\left(1 + \frac{V(x)}{V_0}\right)^{\frac{1}{2}}} + \frac{1}{d} \int_{d_0}^d dx \right]^{-2} \quad (25)$$

Rearranging and evaluating the second integral in equation (25) yields:

$$\beta \equiv \left[ 1 + \frac{1}{d} \int_0^{d_0} \frac{dx}{\left(1 + \frac{V(x)}{V_d} \frac{V_d}{V_0}\right)^{\frac{1}{2}}} - \frac{d_0}{d} \right]^{-2} \quad (26)$$

where  $V_d$  is the voltage applied to the multiplier cap. The polynomial fit to the electrolytic trough data provides the ratio  $V(x)/V_d$ , so that the correction factor  $\beta$  can be evaluated and plotted for various values of  $V_d/V_0$ . The integrations can be performed numerically; and the result, a computer generated plot for 200 values of  $V_d/V_0$ , is shown in Figure 16 (upper curve, labeled "no grid").

Although Figure 16 allows the prototype data to be corrected, a more satisfactory solution for the new instrument would be to eliminate the need for any correction factor. The magnitude of  $\beta$  depends, ultimately, on the spatial extent of the multiplier potential. If the region of non-zero potential could be restricted to the immediate vicinity

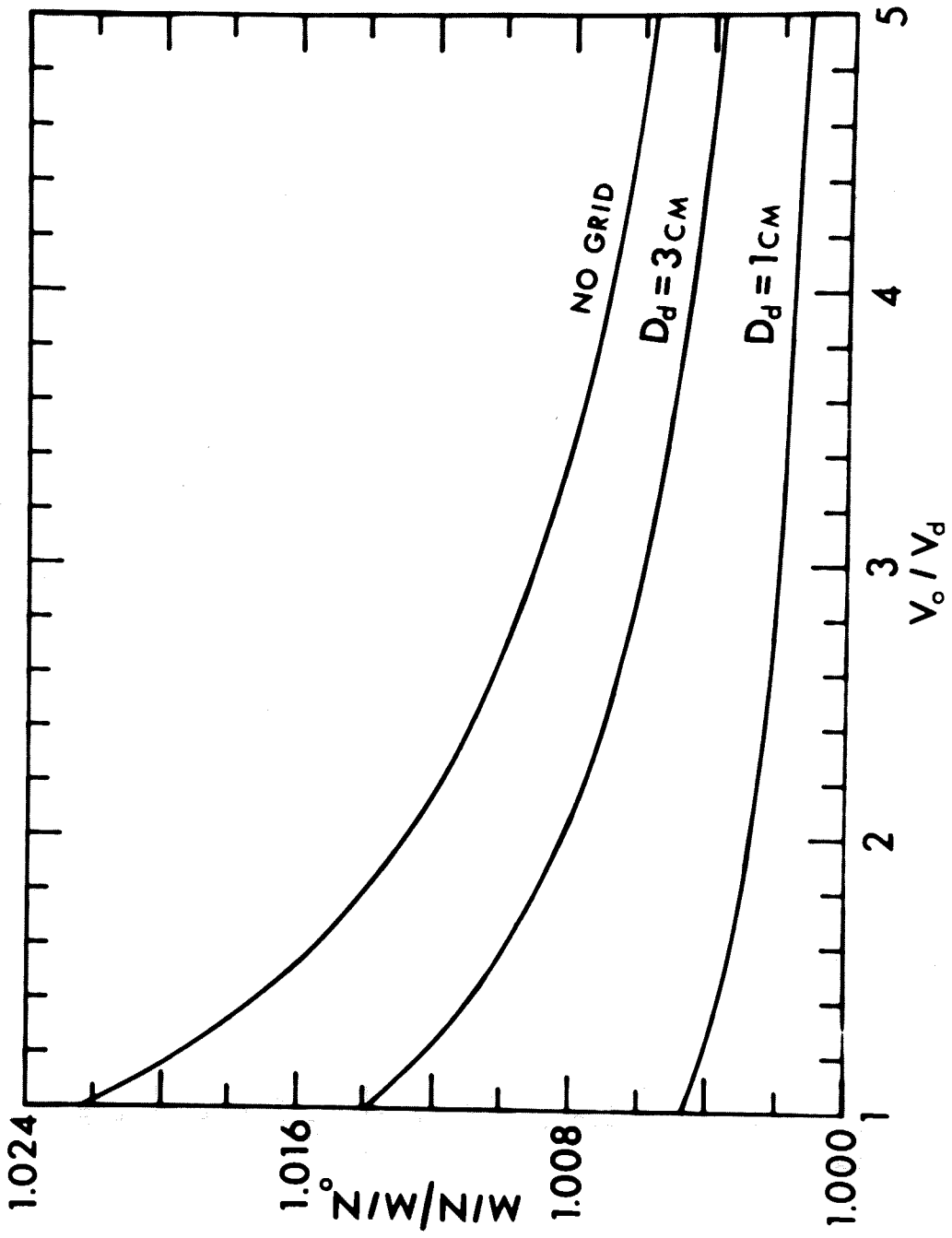


Figure 16. (m/n) Correction Curves

of the multiplier cap, rather than extending for 10 cm as shown in Figure 15,  $\beta$  could be made as close to unity as desired. By placing a grounded grid some distance  $d_o$  in front of the cap, this situation can be easily achieved. Consider the cap to be a solid plate at potential  $V_d$ , and the grid a parallel grounded plate spaced  $d_o$  from it. The potential between the plates is of the form:

$$V(x) = \frac{V_d}{d_o} (d_o - x) \quad (27)$$

where  $x$  is, again, the ion's position measured from the cap. Substitution of equation (27) into equation (26) yields for the correction factor;

$$\beta = \left[ 1 + \frac{1}{d} \int_0^{d_o} \frac{dx}{\left[ 1 + \frac{V_d}{V_o d_o} (d_o - x) \right]^{\frac{1}{2}}} - \frac{d_o}{d} \right]^{\frac{1}{2}} \quad (28)$$

The integral is a standard form and the resulting value of  $\beta$ , after integration and some rearrangement of terms, is just:

$$\beta = \left[ 1 + 2 \frac{d_o}{d} \frac{V_o}{V_d} \left( 1 + \frac{V_d}{V_o} \right)^{\frac{1}{2}} - 2 \frac{d_o}{d} \frac{V_o}{V_d} \left( 1 + \frac{1}{2} \frac{V_d}{V_o} \right) \right]^{-2} \quad (29)$$

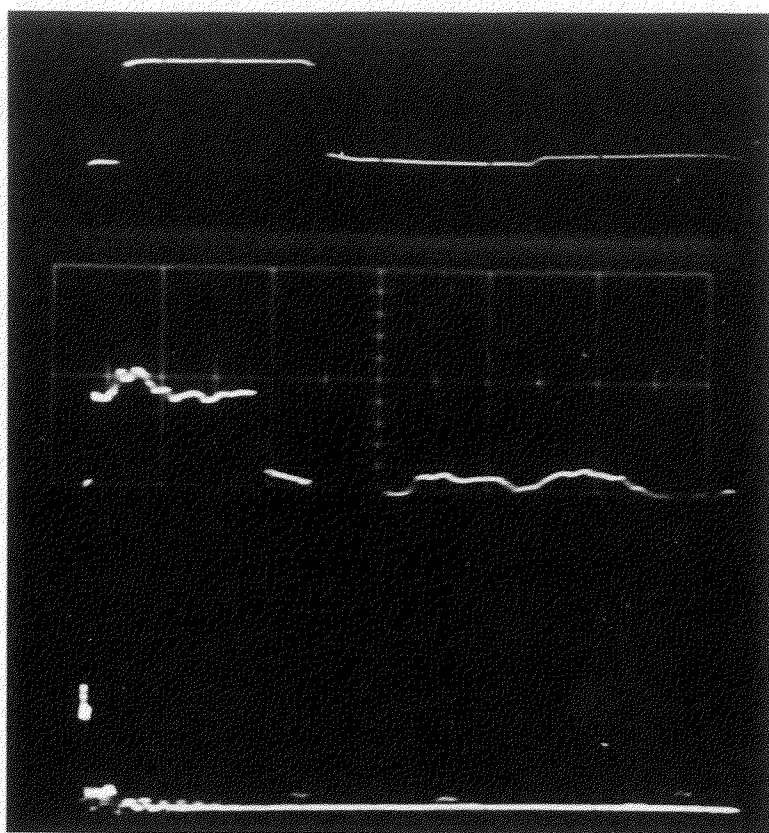
$\beta$ , evaluated from equation (29) for two cases,  $d_o = 3.0$  cm, and  $d = 1.0$  cm, is also computer plotted in Figure 16.

The results indicate that a grid placed one centimeter from the multiplier cap will give a correction factor  $\beta$  of less than 1.005 for the worst case of  $V_o/V_d = 1.0$ . This result, although obtained for the idealized case of parallel plate electrodes, is probably sufficiently accurate for practical purposes. It indicates that placing a wire grid 1.0 cm from the cap reduces the increase in  $m/n$  to below 0.5% for the worst case, and makes it completely negligible for larger initial ion energies. Figure 12B shows the grid in place above the multiplier. All calculations for Figure 16 were made with  $d = .995$  m, corresponding to the time-of-flight tube used in the prototype instrument. For the longer time-of-flight tube currently used,  $\beta$  would be correspondingly smaller.

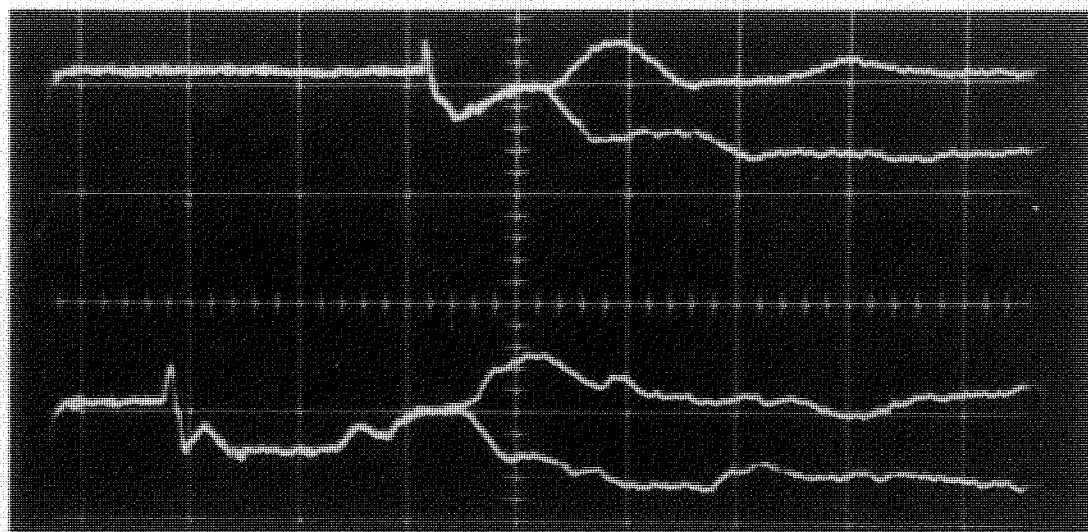
The previous analysis indicates that the effect of stray fields on the ion's energy, and therefore on the mass-to-charge ratio that is obtained cannot be ignored. For this reason special care was taken in the design of the new instrument to provide adequate electrical shielding. But even with adequate shielding, equation (3) must still be modified because the actual energy acquired by the ion, initially, is not simply  $(ne)(V_{dc} + V_{pulse})$ .

The selected ion is evaporated typically, by an 18 ns positive high voltage pulse of 0.33 ns rise time. This pulse is coupled to the tungsten wires leading to the specimen through a DC blocking capacitor located outside of the cold finger assembly (See Figure 4). After passing through this capacitor the pulse must travel to the tip which forms, for practical purposes, the unterminated end of a cylindrically symmetric transmission line. The center electrode of this line consists of the two tungsten leads ending with the specimen, while the outer electrode is the grounded copper shielding tube, and grounded copper housing which surrounds the specimen itself. Such an unterminated line is characterized by voltage reflections.<sup>26</sup> Unfortunately, the line cannot be terminated at the specimen to eliminate these reflections because of the high DC imaging voltage present at all times. As a result, if the initial pulse is of sufficient duration, these reflections will add to it producing, at the tip, an effective pulse whose amplitude is greater by some factor  $\alpha$  than the initial pulse. This "pulse factor", which in the course of this investigation was first observed by plotting for a single isotope metal  $m/n$  vs.  $V_{\text{pulse}}$  (the mass-to-charge ratio for a given species should not depend on the pulse voltage used), is constant for a given line geometry.

A direct measurement of the pulse factor by observing the pulse shape at the tip with a suitable oscilloscope (such as the Tektronix type 519) is quite difficult to interpret. The waveshape depends critically upon the line termination, and placing a probe in contact with, or in the vicinity of the tip radically changes the line's normal boundary conditions. Nevertheless, the measurement was attempted and Figure 17A shows the waveshape at the pulser's output (top trace), and at the tip (lower two traces), resulting from a probe placed in contact with it. The upper and middle traces in this figure were recorded at 10 ns/cm, and the lower trace at 100 ns/cm. Although a small increase in amplitude can be seen several nanoseconds from the start of the pulse, it in no way accounts for the magnitude of the pulse factor observed experimentally. Figure 17B is another measurement using a time domain reflectometer to record the amplitude variations along the line. This device connected in place of the pulser, generates, on an oscilloscope screen, a profile of the amplitude variations along the line to which it is attached. By shorting the tip to ground after the actual measurement, a second trace is obtained whose amplitude decreases at the point of the short thereby indicating the point of the sweep corresponding to the location of the tip. Figure 17B actually records two different measurements. The upper



A. Output of Pulser (upper); at tip (middle);  
at tip (lower)



B. Time Domain Reflectometer Traces: New Divider Assembly (upper); Old Divider Assembly (lower)

Figure 17. The Evaporation Pulse



curves were recorded with the new instrument, while the lower show the result of using an older design. Note the improved amplitude uniformity with the new instrument. A Tektronix type 549 oscilloscope with a 5 ns/cm sweep was used. Unfortunately, the generated pulse is a step function, and does not approximate the actual 18 ns pulse produced by the Huggins generator. Nevertheless, a small amplitude increase is again noted several nanoseconds after the main pulse arrives at the tip. The amplitude variations, including this increase, after the point corresponding to the tip (the short) are those resulting from the reflected wave.

The presence of the pulse factor suggests a modification of equation (3) as follows:

$$\left(\frac{m}{n}\right)_o = K (V_{dc} + \alpha V_{pulse}) \tau^2 \quad (30)$$

where  $\alpha$  is the observed "pulse factor". Moreover, as mentioned previously, the travel time  $\tau$  is not directly recorded on the oscilloscope. What is recorded is the observed time  $t$ , where:

$$t = \tau \pm \delta \quad (31)$$

and  $\delta$  is the total electronic delay time. Equation (3) may now be written in its final form:

$$\left(\frac{m}{n}\right) = K (V_{dc} + \alpha V_{pulse}) (t + \delta)^2 \quad (32)$$

It is assumed, of course, that  $V_{dc}$  and  $V_{pulse}$  are accurately known. The pulse voltage is supplied by the Huggins Laboratory pulse generator (model 961D) mentioned previously, having a maximum amplitude jitter of 4.0%. A Power Designs model 1584 decade-switched high voltage 0-20 kV power supply provides an extremely well-regulated imaging voltage accurately known to  $\pm 0.25\%$  of the switch settings ( $\pm 25$  volts in 10 kV).

Fortunately, at least two independent methods have been found to determine the correction factors  $\alpha$  and  $\delta$ , thereby calibrating the atom probe. Both methods rely upon a prior knowledge of the evaporated species, but such knowledge is possible since several single-isotope metals exist which can be field evaporated in the atom probe. One of these, rhodium ( $m = 103$ ), has been used extensively for this purpose.

## 2. Calibration:

Suppose that a rhodium tip has been suitably prepared, aligned, and placed in the atom probe for a calibration experiment. After establishing a satisfactory FIM pattern with helium, the imaging gas is pumped away. When a

typical background vacuum of  $\sim 3.0 \times 10^{-8}$  Torr is reached, pulse evaporation is started. If a single, sufficiently large pulse is used, many atom layers will field evaporate causing several ions to pass through the probe hole. Provided the total voltage is kept constant, continued pulsing is observed always to produce two mass spikes on the oscilloscope at the same points in time. Since the single isotope metal itself is field evaporating in high vacuum, the reproducible pulses observed could only represent rhodium ions of different charge. Applying equation (32) to each of the two observed pulses on a single sweep, and dividing, one obtains (using the binomial theorem):

$$\frac{\left(\frac{m}{n}\right)_2^2}{\left(\frac{m}{n}\right)_1^2} \approx \frac{t_2^2}{t_1^2} \left[ 1 \pm \frac{2\delta}{t_1} \right] \left[ 1 \pm \frac{2\delta}{t_2} \right] \approx \frac{t_2^2}{t_1^2} \left[ 1 \pm 2\delta \left( \frac{1}{t_2} - \frac{1}{t_1} \right) \right] \quad (33)$$

Or:

$$\left( \frac{t_1}{t_2} \right)^2 \left( \frac{\left(\frac{m}{n}\right)_2}{\left(\frac{m}{n}\right)_1} \right) = 1 \mp \frac{2\delta\Delta t}{t_2 t_1} \quad (34)$$

To a first approximation, the second term in equation (34) is negligible since  $t_1$  and  $t_2$  are both large,  $\Delta t$  is small,

and  $\delta$  must be less than  $t_2$ . Substitution of the measured values of  $t_1$  and  $t_2$  in the resulting equation, and solving for the ratio of the mass-to-charge ratios, gives:

$$\left(\frac{m}{n}\right)_2 / \left(\frac{m}{n}\right)_1 \approx 1.5 \quad (35)$$

Since both pulses correspond to the same mass, equation (35) indicates that triply and doubly charged ions are present. Figure 14A is a typical photograph obtained during such a calibration experiment. Each sweep corresponds to a single evaporation pulse sufficiently large to cause many atom layers of rhodium to field evaporate, and resulting in the impact of several ions with the detector. A time calibration sweep, in this case  $10 \text{ Mhz} \pm 60 \text{ Hz}$ , is displayed in addition to the normal sweeps. The first mass spike in the sweep directly after the time trace corresponds to helium ( $m/n = 4.0$ ) desorbed from the surface.

Since the two species have been identified as doubly and triply charged rhodium, equation (32) may be used to find the pulse factor,  $\alpha$ . Applying equation (32) to each species on a given single sweep and solving the two resulting equations for  $\alpha$  gives:

$$\alpha = \left[ \frac{\left(\frac{m}{n}\right)_2^{\frac{1}{2}} - \left(\frac{m}{n}\right)_1^{\frac{1}{2}}}{K V_{\text{pulse}} \Delta t^2} \right]^2 - \frac{V_{\text{dc}}}{V_{\text{pulse}}} \quad (36)$$

where,  $\Delta t \equiv t_2 - t_1$ , is the measured time difference between the two rhodium spikes;  $V_{dc}$  and  $V_{pulse}$  are accurately known, and  $(m/n)_2 = 103/2$  while  $(m/n)_1 = 103/3$ . Combining equations (13) and (16), and solving for the time delay gives:

$$\delta = t_2 - \Delta t \left[ 1 - \left[ \left( \frac{m}{n} \right)_1 / \left( \frac{m}{n} \right)_2 \right]^{\frac{1}{2}} \right]^{-1} \quad (37)$$

This method<sup>27</sup> then, allows both  $\alpha$  and  $\delta$  to be calculated and the atom probe to be calibrated if at least two differently charged ions of the same known mass appear on a single trace. If several known masses appear, the method can be applied to each measureable time difference, and an average of  $\alpha$  and  $\delta$  computed. Finally, if unknown masses appear on the same trace, they can be determined with a great degree of accuracy since both the pulse factor  $\alpha$ , and the time correction factor  $\delta$ , are known. In practice, an average value of  $\alpha$  and  $\delta$  for the atom probe have been determined from thirty or forty mass pairs ( $Rh^{3+} - Rh^{2+}$ ) using this method.

Other calibration masses may also be used. By admitting hydrogen to the microscope and momentarily reducing the DC to encourage adsorption on the specimen, both  $H^+$  and  $Rh^{2+}$  can be observed on a single trace. The danger is that what one assumes is a  $Rh^{2+}$  ion may actually be a

$\text{RhH}^{2+}$  or  $\text{RhH}_2^{2+}$  molecular ion, while the ion assumed to be  $\text{H}^+$ , may actually be a fragment ion caused by field induced dissociation of  $\text{H}_2^+$  or  $\text{H}_3^+$  at some distance from the tip surface. Even evaporation in vacuum, directly after imaging, often leads to difficulty since helium-rhodium molecular ions,<sup>28</sup> which again must not be confused with the pure metal ion alone, are frequently observed. Only after sufficient pulsing in vacuum can one be reasonably sure that the surface is "clean", and only pure metal ions are being detected. Surface migration of adsorbed atoms from the shank, however, must not be ignored although the coverage due to such a process must be small at the usual tip temperature of 21°K.

The accuracy of the determination of the pulse factor and time correction factor rests, primarily, with the accuracy to which the travel times can be measured. In order to improve the measurement accuracy, each photograph is magnified by a factor of ten using an aerial Ektar lens of negligible distortion. Even so, accuracy is limited to 10-20 nsec at best (probably closer to 20 nsec), primarily by the pulse shape, trace width, and exact position of the zero marker. As a result, typical values of  $\alpha$  and  $\delta$  are found to be:

$$\alpha = 2.00 \pm 0.05$$

and

$$\delta = 0.06 \pm 0.02 \text{ } \mu\text{sec}$$

It is assumed, of course, that the species used for calibration were correctly identified, a situation which, as was indicated, is often difficult to achieve in practice.

A second method of calibration provides an independent determination of  $\alpha$  and  $\delta$ . It also requires a prior knowledge of the evaporated species but unlike the previous method it requires only one known mass spike for calibration. This is often desirable since the double spikes in the previous rhodium experiment can only be obtained consistently, on each trace, by a very rapid evaporation of the tip. The required rate is often as large as 10 surface layers per nanosecond or 2 1/2 meters of metal per second! Besides the danger of premature tip destruction which such rates can encourage, the physical conditions at the surface must be much different than during gentle evaporation in which the doubly charged ion, predicted by field evaporation theory, almost exclusively appears. A simple calculation using evaporation rates of 10 layers/nanosecond indicates that current densities equivalent to those found in the space charge region for electrons are approached. The density of ions could, therefore, appreciably alter the local potential distribution near the surface, perhaps "screening" a percentage of the ions from the true potential of the tip. Fortunately, such an effect, which should cause differences in the travel times obtained during

gentle and rapid evaporation, has not been observed. The effect might be masked, of course, by the current uncertainty in time measurement which is of the same order as the expected time differences.

The second calibration technique requires an experiment similar to the one previously described. Assume, again, that a single isotope metal, perhaps rhodium, is pulse evaporated in high vacuum after having first established a satisfactory pattern in an imaging gas. After removing the gas, the pulse voltage is set at some convenient value, and the DC voltage increased until ions are detected during each pulse. Pulsing is continued, and the DC voltage gradually raised until the surface is "cleaned" and only consistent masses, one per trace, are observed. Figure 14B is a typical photograph obtained during such an experiment. Note the expanded time sweep used ( $0.2\mu\text{sec}/\text{division}$ ).

Field evaporation theory, or comparison with a species observed under similar conditions previously, indicate that  $\text{Rh}^{2+}$  ( $m/n = 51.5$ ) is being detected. This is the value of  $m/n$  which equation (32) would predict if  $\alpha$  and  $\delta$  were known. One is interested, then, in minimizing the difference between 51.5 and the value of  $m/n$  predicted by equation (32) for each  $\text{Rh}^{2+}$  pulse detected.



In minimizing this difference for  $n$  recorded mass spikes, the square of the difference must also be minimized. That is, the quantity:

$$\sum_n \left[ 51.5 - K (V_{dc} + \alpha V_{pulse}) (t \pm \delta)^2 \right]^2 \quad (39)$$

is to be minimized with respect to the unknown quantities  $\alpha$  and  $\delta$ . Therefore, one requires that:

$$\frac{\partial}{\partial \alpha} \sum_n \left[ 51.5 - K (V_{dc} + \alpha V_{pulse}) (t \pm \delta)^2 \right]^2 = 0 \quad (40)$$

and:

$$\frac{\partial}{\partial \delta} \sum_n \left[ 51.5 - K (V_{dc} + \alpha V_{pulse}) (t \pm \delta)^2 \right]^2 = 0 \quad (41)$$

where  $V_{dc}$ ,  $V_{pulse}$ , and  $t$  may vary for each trace, but are known. Performing the indicated differentiations gives:

$$\sum_n \left[ 51.5 - K (V_{dc} + \alpha V_{pulse}) (t \pm \delta)^2 \right] V_{pulse} (t \pm \delta)^2 = 0 \quad (42)$$

and

$$\sum_n \left[ 51.5 - K (V_{dc} + \alpha V_{pulse}) (t \pm \delta)^2 \right] \times (V_{dc} + \alpha V_{pulse}) (t \pm \delta) = 0 \quad (43)$$

These two equations, containing  $n$  terms each, can be solved simultaneously for  $\alpha$  and  $\delta$ . Their complexity demands a numerical solution which, fortunately, is easy to obtain provided some form of electronic calculator is available. A convenient method for solving such simultaneous equations, called the Newton-Raphson method, is well known<sup>29</sup> and requires, in this case, the solution of  $2 \times 2$  determinants. The necessary steps are outlined, for convenience, in Appendix B. One finds that the values obtained for  $\alpha$  and  $\delta$  do not depend upon the values chosen to initiate the solution provided, of course, that physically reasonable numbers are used. Practically, this means that  $\alpha$  can be set equal to 1.0 and  $\delta$  set equal to 0.0, and the method will rapidly converge to final values which are found to be within the uncertainty of the previous values within the range. That is, it is found once again that:

$$\alpha = 2.00 \pm 0.05$$

and:

$$\delta = 0.06 \pm 0.20 \text{ } \mu\text{seconds}$$

As stated, previously, the value of  $\alpha$  obtained by either calibration method depends upon the exact geometry of the tip end of the pulse transmission line. For example, increasing the small one millimeter aperture in the copper housing to eight millimeters decreases the pulse factor to 1.40. Experimentally, it was found that the pulse

factor does not depend upon the tip material used for calibration, nor upon the type or level of cryogenic coolant used in the cold finger. It was thought originally that the discontinuity in dielectric constant across the surface of the liquid in the cold finger might lead to major reflections on the line. This would result, it seemed, in variable travel times for the reflected pulses along the line as the level of the coolant changed. As a result, the point in time of maximum pulse amplitude at the tip (and hence the total ion energy) would be a function of the level of liquid in the cold finger. Fortunately, the experiments performed have not shown such an effect.

### 3. Resolution and Accuracy:

The degree to which adjacent mass spikes may be just resolved depends, ultimately, upon the method of time measurement employed. As indicated previously, using an expanded time sweep allows adjacent masses differing by less than one mass unit to be easily distinguished. The resolution of the instrument is, therefore, much better than one amu for any mass of interest.

The accuracy of the mass determination, however, depends upon the magnitude of the uncertainties in the experimental parameters of time, voltage, and distance. The time measurement error, as well as the error in the time

delay  $\delta$ , is probably at worst  $\pm 20$  nanoseconds. For  $V_{dc} = 8.0$  kV, the error in  $V_{dc}$ , as mentioned previously, is about  $\pm 20$  volts. The error in  $V_{pulse}$  is more difficult to determine since amplitude measurements of 18 nsec pulses with 0.33 nsec rise times are currently, state-of-the-art. Within the 3.0% accuracy of the calibrated vertical amplifier of a Tektronix type 519 oscilloscope, the pulse amplitude corresponded to that read on the pulser. But this measurement was made with 60 pulses per second, and the pulser specifications do indicate a maximum amplitude "jitter" of  $\pm 4.0\%$  from pulse to pulse. These considerations indicate a total maximum error in  $V_{pulse}$  of about 7.0%, or  $\pm 70$  volts for  $V_{pulse} = 1.0$  kV. In practice, the actual error is probably less than this, perhaps closer to 5.0% or  $\pm 50$  volts for  $V_{pulse} = 1.0$  kV.

The error in the distance measurement is, at worst,  $\pm 2.0$  mm for  $d = 2000$  mm, or 0.1%.

The total maximum error in the mass determination is found from direct differentiation of equation (32). Dividing the result by equation (32) itself gives the total corresponding error in these quantities. A further fractional error in  $m/n$ . The result is:

$$\frac{\Delta(\frac{m}{n})}{(\frac{m}{n})} = \frac{(\Delta V_{dc} + \alpha \Delta V_{pulse} + \Delta \alpha V_{pulse})}{V_{dc} + V_{pulse}} + \frac{2(\Delta t + \Delta \delta)}{t + \delta} + \frac{2 \Delta d}{d}$$

(44)

where the last term results by assuming that the error in the constant,  $K$ , is due entirely to the distance measurement. Substitution in equation (44) of  $V_{dc} = 8.0$  kV,  $V_{pulse} = 1.0$  kV,  $\alpha = 2.00 \pm .05$ , and  $\delta = 0.06 \pm .02$   $\mu$ sec., with the errors in voltage and time as given previously, results in a maximum fractional error of:

$$\frac{\Delta(\frac{m}{n})_o}{(\frac{m}{n})_o} = 0.012 + \frac{0.08}{(t + .06)} + .002 \quad (45)$$

This corresponds to an error in mass determination of  $\pm 0.5$  amu at  $(\frac{m}{n})_o = 20$ , and  $\pm 1.9$  amu at  $(\frac{m}{n})_o = 100$  using for  $t$ , in equation (45), a value calculated from equation (32).

Fortunately, the accuracy can be greatly improved if multiple masses appear on a single sweep, provided at least one mass is known, a priori. In such instances equation (36) can be used to predict the other masses in terms of the measured time differences which are independent of the time delay  $\delta$ , the position of the zero-time marker, and the corresponding errors in these quantities. A further increase in accuracy is obtained by expanding in time the portion of the sweep which contains the mass spikes of interest. Resulting mass determination uncertainty may approach  $\pm 0.4$  amu at  $(m/n)_o = 50$ .

Of course, as indicated earlier, if two masses are known, a priori, an unknown mass on the same sweep can be determined to perhaps  $\pm 0.2$  amu since a calibration using the two known masses will accurately determine both the pulse factor and the time delay. Then, using the results for  $\alpha$  and  $\delta$ , as well as the time difference between a known, and an unknown mass in equation (36), the unknown mass-to-charge ratio can be accurately determined.

## VI AIMING THE ATOM PROBE

The two most difficult problems associated with atom probe analysis are single particle detection and aiming, where aiming simply refers to the ability to detect, unambiguously, a preselected surface species. As was indicated previously, the rate of field evaporation of the emitter can be carefully controlled so that only one atom layer, or just a fraction thereof, will evaporate per pulse. As a result, if the probe hole diameter is approximately the same as that of the image of an atom positioned over it, and a single mass is observed after pulsing, a single particle must have been detected. The question is whether the detected ion corresponds to the surface species whose image was placed over the probe hole.

There is no reason to assume, a priori, that the field evaporated ion will follow the same trajectory as the less massive gas ions which imaged it. In fact, since the desired species originates at the surface where the tangential potential gradient is a maximum, it is likely that it will follow a somewhat different trajectory. As a result, although an image spot is placed over the probe hole, the evaporated ion itself may strike the screen at some other point and never hit the detector. What may be recorded is the impact of a surface species which was imaged near, but not on, the probe hole.

The magnitude of such an effect is difficult to predict theoretically, because of the problem of formulating a realistic expression for the motion of a particle originating at the surface. Even if the differential equations governing the motion could be obtained, their solution would critically depend upon the initial boundary conditions at the surface--boundary conditions which are unknown.

Conventional trajectory problems which are difficult to handle theoretically, can often be solved by using a rubber sheet analog to approximate the actual potential distribution which governs the particle's motion. But even if the usual experimental difficulties<sup>30</sup> associated with such an approach are minimized, the method cannot be applied with confidence to the atom probe problem since the analog is based on a classical description of the particle's motion. Obviously, near the surface where the particle is most strongly influenced, a quantum mechanical description of the motion is demanded. In addition, the trajectories obtained with the rubber analog depend critically upon the chosen initial velocity vector of the particle which, as was mentioned, is unknown. Fortunately, experiments can be performed to indicate the magnitude and degree of anisotropy of the effect. Since the motion of the evaporated ion must be strongly governed by the local



field at the surface, it is expected that the effect will vary with position on the surface. For example, the trajectory of ions originating at the edge of net planes (where the normal as well as the tangential potential gradient is large) would be more strongly perturbed than if the ions originated from a smooth crystallographic area of slowly varying potential.

The most desirable method of investigating the effect would be to record the relative positions of the field evaporated ions on the screen, and compare them to the corresponding image positions observed in the presence of a gas. Unfortunately, photographic techniques do not provide the necessary sensitivity and other methods, such as the use of a network of closely spaced miniature detectors on the screen, would be difficult to employ.

The aiming problem has been investigated in the current instrument by using a tungsten specimen, and placing the probe hole on the 110 plane, where only the atoms at the edge of the plane are imaged. If an image spot is placed over the probe hole, and a few atoms of the net plane edge are evaporated, no metal ion is ever detected. However, if the probe hole is placed approximately one image spot diameter from the selected image spot toward the center of the plane, a metal ion is recorded during essentially every pulse.<sup>31</sup> By performing the experiment many

times, and at various locations about the center of the plane, the same observation is always made: a tungsten ion will be detected only if the probe hole is displaced toward the center of the plane. This implies that at the surface, the evaporated ion from the edge of the 110 plane always acquires a tangential velocity component toward the center of the plane, and that the magnitude of this component is the same for any such ion evaporated. If the same experiment is performed on the imaged center of the 111 plane, a metal ion is detected with each pulse, indicating that the tangential velocity component acquired by an ion near the center of a plane is negligibly small.

Although these results do indicate that an effect is present, they are not sufficiently accurate to make definite predictions about its magnitude and direction. In each case there is no absolute assurance that the ion detected did not originate far from the probe hole since it is impossible to distinguish between the atoms comprising the emitter. A better experiment would entail the deposition, by evaporation, of a few widely spaced "foreign" atoms on the emitter surface.<sup>31</sup> These atoms, chosen so as to have a mass greatly different from that of the substrate atoms, would be visible in the image, and could be evaporated after positioning their image over, or near, the probe hole. In this way the ambiguity in aiming, inherent in the

evaporation of the indistinguishable atoms of the emitter itself, would be minimized. Of course, such an experiment relies upon the assumption that the adsorbed species would encounter the same forces as the substrate atoms normally evaporated, and therefore follow the same trajectory. The validity of this assumption is open to question, however, because of the different, and usually weaker, bonding between adsorbed species and substrate. Because of time limitation, this aiming experiment has not yet been done.

Another problem associated with proper aiming of a selected species arises from the presence of stray electrostatic fields within the microscope body, particularly those which can change during pulse evaporation. During image positioning one essentially compensates for the effect of any steady state electrostatic field, since the trajectories of charged particles in such fields are independent of their mass-to-charge ratio. For this reason, the focusing action of the aperture in the cold finger housing can be neglected since both paraxial metal ions, and gas ions will follow the same path. Of course, the focusing action of such a lens depends, at least to first order, on the ions' energy. But the pulse voltage is usually a small fraction of the steady state DC imaging voltage so that the evaporated surface species will have, for practical purposes, the same energy as the imaging gas ions.

The thorough shielding of the tip assembly in the present instrument, as well as the 18 nsec pulse duration used, insures that the evaporated ion is in field free space when the evaporation pulse terminates. As a result, any significant change in the ion's trajectory, which might be caused by the rapid decrease in voltage during the fall time of the pulse, is minimized. Other atom probe instruments, in particular one recently used by Brenner and McKinney,<sup>32</sup> neglect to consider the electrode geometry in the microscope body. As a result, Müller<sup>33</sup> has been able to demonstrate, experimentally, that Brenner and McKinney could not detect preselected species as originally claimed. A mock-up of their apparatus clearly indicated an image shift by as much as ten atomic diameters during pulsing.

Although difficulty with aiming is recognized, its importance, at least for this work, must not be over emphasized since many problems of interest do not require identification of a specifically selected surface atom. As an example, the continual appearance of only pure metal ions when the probe hole was placed in the area of the zone line decorations of tungsten and iridium, clearly indicated that these decorations were displaced metal atoms, and not oxides, nitrides, or other impurities as might have been imagined.

## VII. EXPERIMENTAL RESULTS

Pulsed field evaporation in the atom probe may be conducted in high vacuum ( $10^{-8}$  Torr) or in the presence of an imaging gas. Both methods of operation have their particular advantages. Evaporation in vacuum assures that the partial pressure of ambient, residual gas contaminants is kept at an absolute minimum, but precludes the possibility of observing the surface. If an imaging gas is present, evaporation of the specimen may be observed continuously but, because of the dynamic gas supply system, the background vacuum suffers. A titanium sublimation trap, connected to the microscope body, helps to rectify the situation, but only if it is periodically reactivated.

### 1. Field Evaporation in Imaging Gas

Evaporation in imaging gas is interesting from a physical point of view because the evaporation field for most metals appears to be lower than if evaporation were conducted in vacuum. Both Young,<sup>34</sup> and later, Ehrlich and Hudda,<sup>35</sup> attributed this effect to the impact of electrons with the surface. In view of the low energy of these electrons, assumed to be produced by the ionization of the imaging gas, and the small cross section<sup>36</sup> for desorption by electron bombardment, Nishikawa and Müller<sup>37</sup> later proposed that the impact of neutral gas atoms with the surface might be responsible. Recent data obtained with the atom probe

suggests still another mechanism: weakening of the metal-metal surface bonds by adsorbed gas atoms, and the subsequent formation of metal-gas molecular ions.

Previously, it was assumed that an imaged emitter surface was perfectly clean<sup>38</sup> since the electric field, which could easily ionize helium in space, would certainly ionize all other contaminants before they reached the surface. Atom probe studies have indicated, however, that this is usually not the case.<sup>39</sup> Both hydrogen, and the noble imaging gases have been consistently detected on the surface, and under certain conditions appear to be so abundant that they must provide coverage equivalent to a significant fraction of a monolayer. When the imaging gas is removed, and pulsing continued in vacuum, these species are still detected for a considerable length of time, indicating that high ambient gas pressures are not necessary for reasonable coverage. Recent work by McKinney and Brenner<sup>40</sup> confirm this result, since their investigations show that noble gas ions are detected at partial pressures as low as  $5.0 \times 10^{-9}$  Torr, almost an order of magnitude smaller than the background pressure in the atom probe being described. Although Nishikawa and Müller<sup>37</sup> postulated the existence of adsorbed imaging gas, and Barofsky<sup>12</sup> indicated its presence, little emphasis was placed upon it until the recent paper by Müller,<sup>39</sup> et. al. It is now

clear that the polarization binding energies of helium and neon at the imaging fields usually encountered on the surface of an emitter,  $\sim 4.5 \text{ V/\AA}$ , are an order of magnitude larger than those due to a pure van der Waals interaction. As a result, the adsorption of the imaging gas must be due, primarily, to the electric field. In addition, atom probe studies have indicated that the imaging gas could only be adsorbed within a certain field range, which depended upon the gas and the emitter temperature. The data allowed the limiting field strengths to be estimated, thereby giving numerical bounds to the interval in which field adsorption could occur.

A great deal of significance must not be attributed to any individual mass spike recorded during operation in imaging gas since the spike may actually be due to a secondary process, and therefore not represent the true mass of the detected particle. These secondary processes, which will be discussed later, include charge exchange, field dissociation of molecules evaporated from the surface, and the imaging process itself which produces an ion current at the detector. As a result, in order to obtain meaningful information in the presence of an imaging gas, a large number of spikes must be analyzed and only those masses considered which are statistically abundant. If the

calculated mass-to-charge ratios are plotted in the form of an abundance vs.  $m/n$  histogram, the meaningful events are easily recognized.

Rhodium ( $m = 103$ ) was chosen for the initial experiments since it has no isotopes, thereby eliminating much ambiguity in mass identification. The probe hole was confined, primarily, to a small region on the 011 plane although other sites were also investigated. Gentle evaporation at  $78^\circ\text{K}$  or  $21^\circ\text{K}$  produced, almost exclusively, the doubly charged ion predicted by field evaporation theory, while rapid evaporation produced triply charged ions as well. The unexpected occurrence of  $\text{Rh}^{3+}$  appears to be due to a physical effect of the increased evaporation rate, and correspondingly higher evaporation field, and not to the fact that an increased rate produces more ions per unit time so that, statistically, a less abundant species should be observed more frequently. Unfortunately, the relative abundance of the two species cannot be determined by merely counting the total number of mass spikes produced by each, since several identical ions detected during a single pulse would appear, in time, as a single spike of large amplitude. Obviously then, a pulse height analysis would have to be performed as well as a simple count, but the statistical nature of the secondary electron emission process in the multiplier itself makes the result difficult to interpret.



The independence of the charge of the observed species with temperature is in qualitative agreement with recent calculations by Tsong,<sup>41</sup> based upon experiments by Vanselow and Schmidt<sup>42</sup> and Barofsky and Müller.<sup>43</sup> Although the evaporation rates used in these experiments were much less than those generally employed in atom probe analysis, one must be certain that it is not the possible charge dependence on rate, just mentioned, which is actually being observed. Such assurance can only be obtained if the evaporation rate is held constant as the temperature is changed, a condition not previously emphasized.

Figure 18 is a computer plotted histogram (with 0.1 amu resolution) of the data obtained by analyzing 2089 mass spikes, obtained during several rhodium experiments. Equation (32) with  $\alpha = 1.0$  and  $\delta = 0.0$  (equivalent to equation (3)) was used to calculate the mass-to-charge ratios. The data was replotted in Figure 19 again using equation (32), but with  $\alpha = 2.0$  and  $\delta = 0.02$ . A comparison between the figures clearly shows the importance of the pulse factor and time delay in accurate mass determination. Because several different experiments were incorporated in Figure 19, and pulse amplitudes were ignored, no attempt should be made to extract absolute abundances. Even relative abundances should not be emphasized since many spikes were obtained during vacuum experiments in which the number of

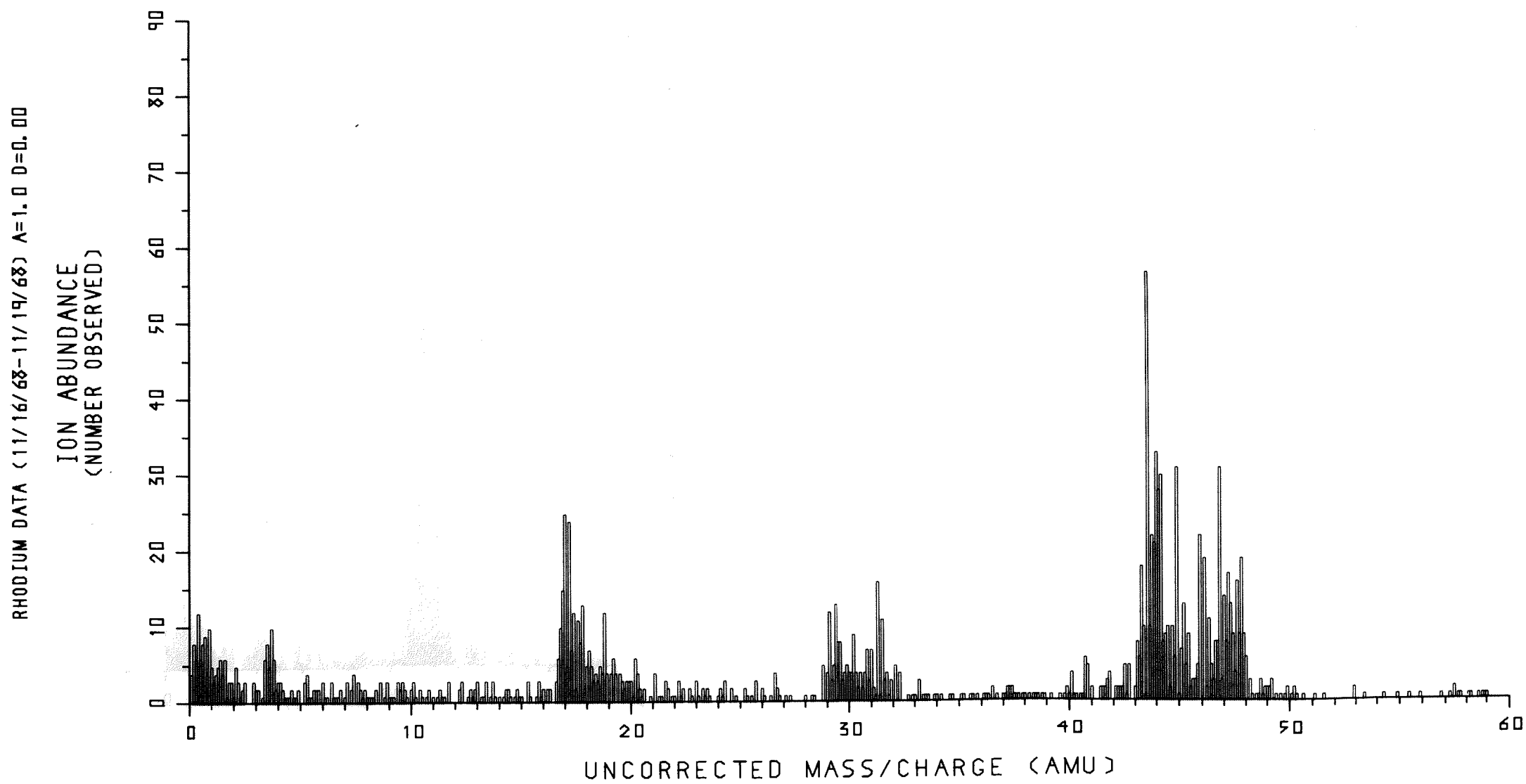


Figure 18. Abundance Histogram ( $\alpha = 1.0$ ,  $\delta = 0.0$ )

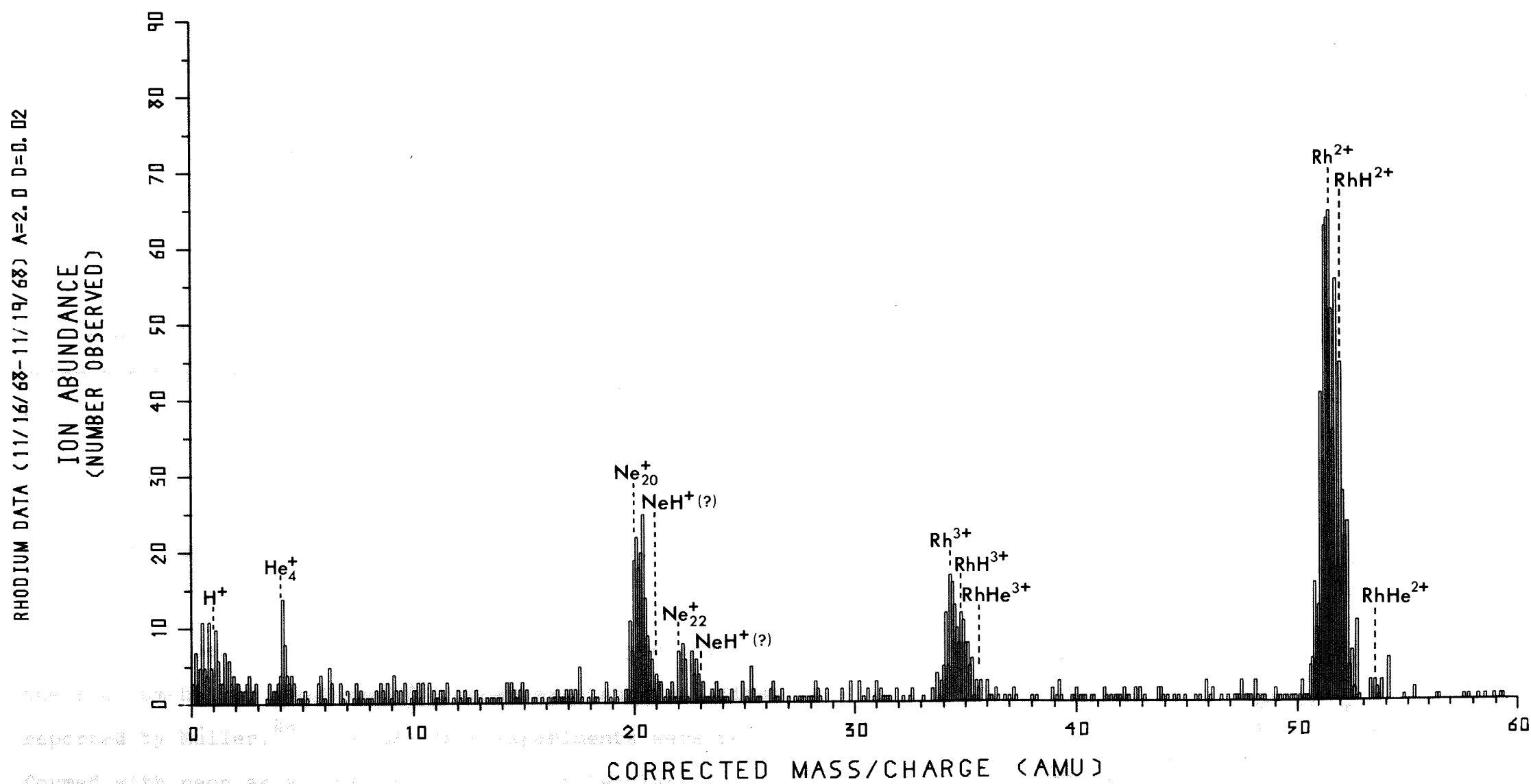


Figure 19. Abundance Histogram ( $\alpha = 2.0$ ,  $\delta = 0.02$ )

image gas ions would be significantly reduced. Nevertheless, several striking features characterize this figure.

The appearance of the peaks at  $m/n = 1.0$ ,  $4.0$ ,  $20.0$ , and  $22.0$  clearly indicate, as was mentioned previously, that gas atoms are present, and abundant, on the surface. A careful examination of all multiple spikes detected during a single evaporation pulse, as well as the width of the rhodium peaks, indicates that rhodium-hydrogen ions (appearing at  $m/n = 34.7$  and  $m/n = 52.0$ ) are also extremely abundant. Recent experiments using an EAI "Quad" residual gas analyzer indicate that there is a significant amount of hydrogen in the microscope, produced by dissociation of water vapor on the ionization gauge, or titanium sublimation trap, filament. Since the current atom probe cannot be completely baked, water vapor will always be present, dynamically, even with liquid hydrogen cooling, and the resultant hydrogen will always be a contaminant, reacting with the emitter to produce hydrides.

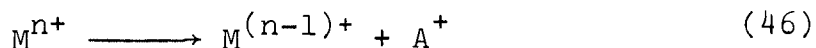
A small peak at  $m/n = 53.5$  indicates the presence of the rhodium-helium ion,  $\text{He-Rh}^{2+}$ , whose existence was first reported by Müller.<sup>44</sup> Although many experiments were performed with neon as an imaging gas, neon molecular ions were never definitely observed.

Since the reduction of the evaporation field occurs with neon as well as helium, compound ion formation at the surface must not be the primary mechanism. Rather, field adsorption of imaging gas seems to be primarily responsible. However, no definite conclusion can be reached since, to date, all experiments have been performed in the presence of some residual hydrogen, and the ability of hydrogen to lower the evaporation field is well known. This effect, incidentally, can now be explained by the formation of metal hydrides (previously predicted by Müller<sup>18</sup>) with the subsequent reduction of local bond strengths.

A large number of "background" events can be observed in Figure 19, uniformly distributed over the entire mass range. The average "height" of these peaks corresponds to 3 or 4 events, and a systematic study of the data shows that they appear only during the experiments performed in imaging gas. Because of their seemingly random distribution, they must not be confused with surface species of interest. Actually, they represent imaging gas ions striking the detector at random times during a single oscilloscope sweep.

Previously, it was thought that they were the result of some form of charge exchange process occurring near the tip.

To investigate this possibility, assume that a surface species,  $M$ , field evaporates with charge  $n$ , and at some distance from the surface where the potential is  $V$ , singly ionizes an excited gas atom,  $A$ . The charge exchange reaction described is of the form:



If the surface species has mass  $M$ , and the gas atom, mass  $m$ , the final kinetic energy attained by each species will be:

$$\frac{1}{2} M v_M^2 = n e (V - V_0) + (n-1) e (V - 0) \quad (47)$$

and:

$$\frac{1}{2} m v_m^2 = e (V - 0) \quad (48)$$

where  $v_M$  and  $v_m$  are the final velocities of the surface, and gas ion, respectively.  $V_0$  is the potential at the emitter, and  $V$  the potential in space where the reaction occurred. Since ions will strike the detector only if they travel quite close to the instrument axis, only rectilinear motion has been considered.

The travel times for metal and gas ion can be calculated directly from equation (2). Identifying

$(V_{dc} + \alpha V_{pulse})$  as  $V_0$ , and setting  $\delta = 0$  allows the  $m/n$  ratio for metal and gas ion to be calculated from equation (32). Calling this ratio  $(M/n)_{calculated}$ , one obtains, for the metal and gas ion, respectively,

$$(M/n)_{calculated} = M/n \left[ 1 - 1/n (V/V_0) \right]^{-1} \quad (\text{metal ion}) \quad (49)$$

$$(M/n)_{calculated} = m/n \left[ V/V_0 \right]^{-1} \quad (\text{gas ion}) \quad (50)$$

What will be observed on a single time sweep is, then, two mass spikes whose calculated ratios as given above depend, for a given species, upon the potential ratio  $V/V_0$ . When  $V = V_0$  or charge exchange occurs at the emitter, the resulting ions are accelerated by the full potential difference. If the process occurs where  $V = 0$ , only the metal ion has been accelerated by the full potential difference. The ionized gas atom, undergoing no acceleration, takes an infinite time to reach the detector, which corresponds to a calculated  $m/n$  of infinity. In practice, the two calculated ratios can be plotted against each other for various values of  $V/V_0$  between 0 and 1.0. The results, computer plotted in Figures 20 and 21 allow one to determine if charge exchange is occurring, by simply comparing any pair of mass ratios read from the figures with any pair corresponding to mass spikes observed on a single time sweep.

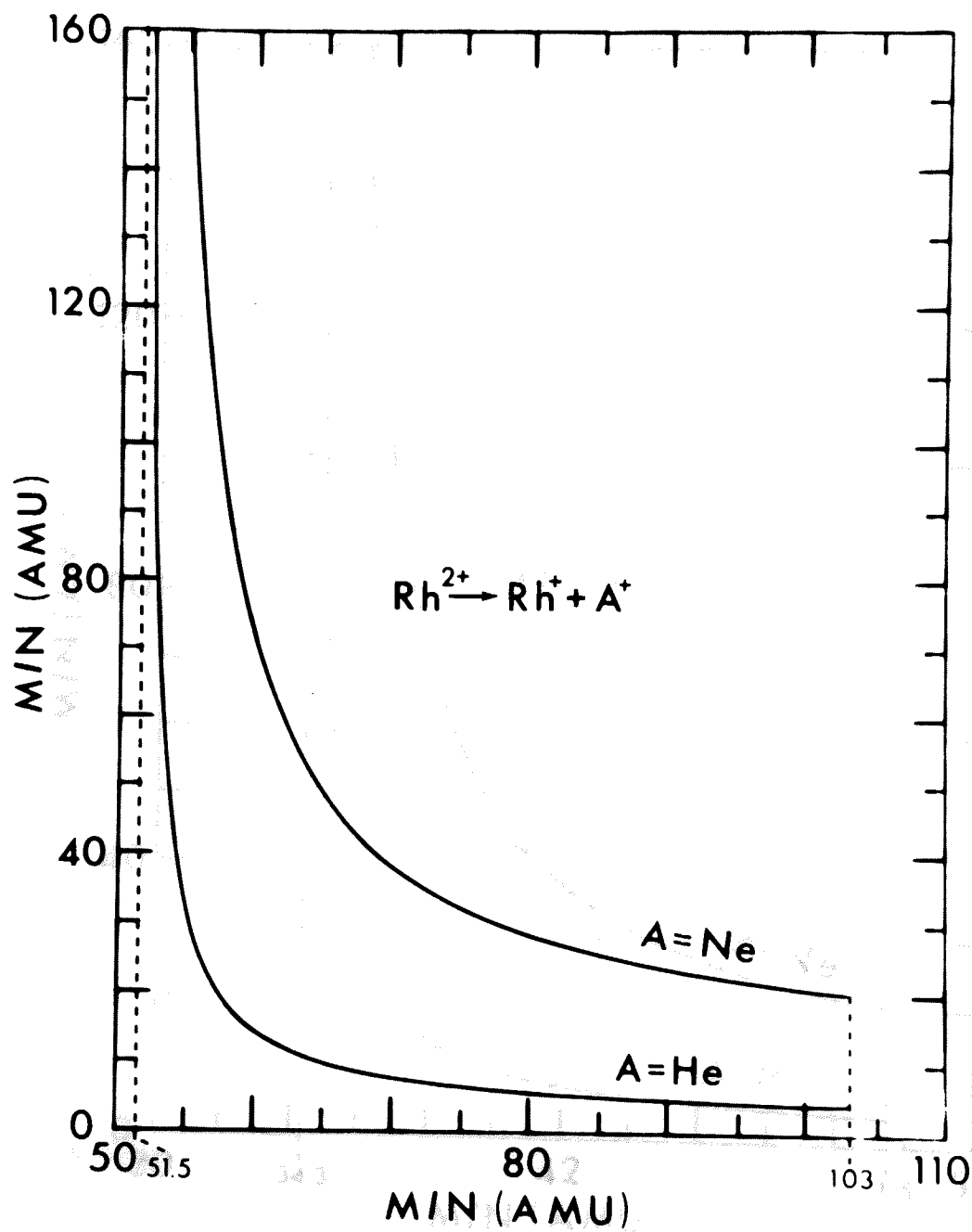


Figure 20. Charge-Exchange Pairs



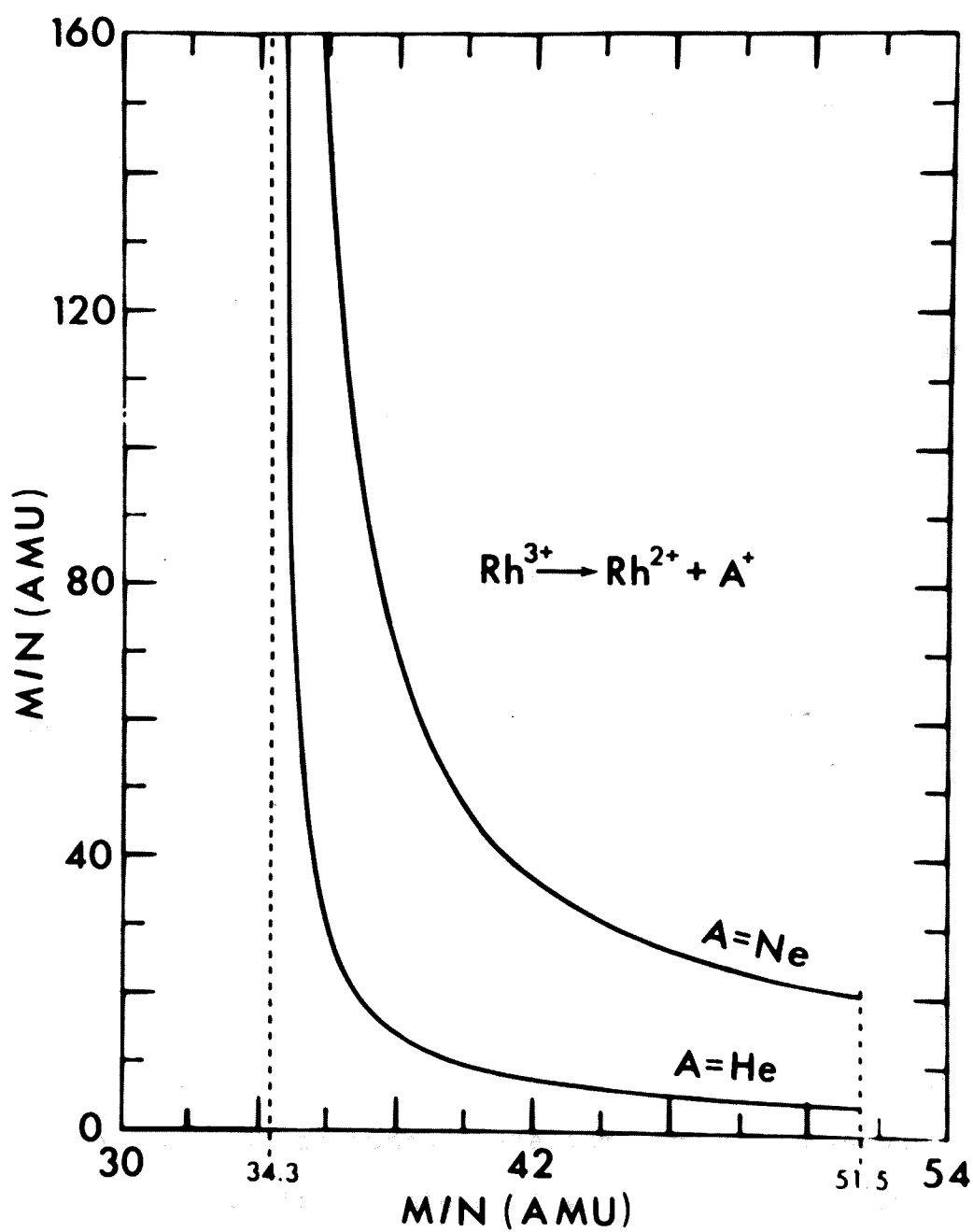


Figure 21. Charge-Exchange Pairs

Although the figures give the results for four possible reactions, only perhaps ten sweeps out of many hundred analyzed indicate the presence of charge exchange pairs. To determine if one species was appreciably deviating from the axis, and therefore being blocked by the screen, a larger probe hole was used and the experiment repeated. The occurrence of possible charge exchange pairs remained a rare event, indicating that charge exchange is not a significant process.

Figure 22 presents the results of investigating the evaporation of tungsten in helium gas. Because of its closely spaced isotopes, quantitative discussion of the masses observed is difficult. A trend is, however, quite clear. The distribution curve is definitely "skewed" toward the larger  $m/n$  ratios, and the actual peak heights indicate that helium-tungsten molecular ions may be responsible. The relative abundance of the tungsten isotopes are indicated by the length of the solid black lines appearing above the distribution. These lines indicate where pure tungsten, as well as tungsten-helium ions would occur on the mass scale. It is interesting to note that tungsten field evaporates, primarily, as a triply charged ion, and on occasion quadruply charged. This observation is not predicted by field evaporation theory, yet is not unexpected either,<sup>45</sup> because of the current uncertainty in the

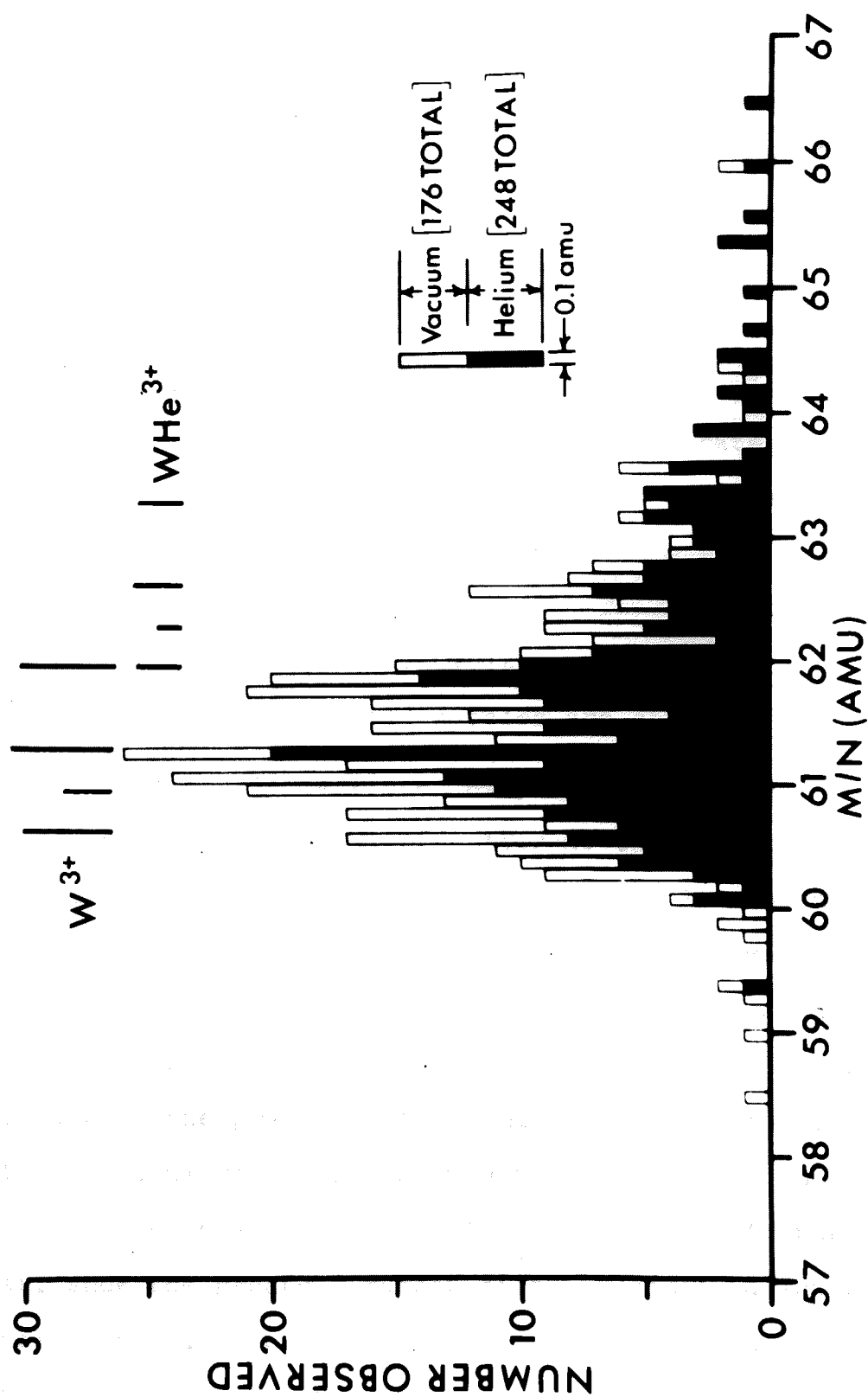


Figure 22. Abundance Histogram (Tungsten)

value of the higher ionization potentials of tungsten. Actually, using the fact that tungsten does not evaporate, usually, as  $W^{3+}$ , one can predict its formerly uncertain higher ionization potentials.

## 2. Field Evaporation in Vacuum

Of the two possible methods of operation, field evaporation in vacuum is certainly the most difficult. Since the surface cannot be seen, the evaporation rate can only be inferred from either the charge of the species being detected, or the amplitude of the resulting mass spikes. And, since the evaporation field is higher in vacuum, one must gradually raise the tip voltage at some arbitrary rate and pulse continually until species are observed.

Several metals have been evaporated in vacuum to see if the species observed were different than those detected when imaging gas was present. For the metals examined, Ta, Ir, Rh, W, Mo, Be, and Fe, each evaporated, primarily, as a doubly charged ion, with the exception of tungsten which evaporated as triply charged ion. The same results were recorded in the presence of an imaging gas. Oxides, hydrides, and nitrides have been detected on occasion, with all of these metals, although iron experiments in particular, show the greatest number of these compound ions. Singly charged iron and beryllium have occasionally been detected, as well as triply charged ions of all metals

except, perhaps, beryllium for which the data is inconclusive.  $W^{4+}$  has been recorded on occasion, the most highly ionized species detected thus far.

Investigations of Re-Mo and Rh (60%) - Pt (40%) alloys have indicated that the individual metals evaporate with the same charge as if the pure metal was field evaporated itself. Thus, the alloy experiments show primarily  $Re^{2+}$ ,  $Mo^{2+}$ ,  $Rh^{2+}$ , and  $Pt^{2+}$  ions.

A rather surprising result obtained during several rhodium and iron experiments in vacuum, was the occurrence of fractional mass-to-charge ratios between one and two, and much less abundantly, between two and three. On occasion, these occurred on the same time sweep as two known species so that the unknown ratios could be determined very accurately. Both  $H_2^+$  and  $H_3^+$  have also been observed, suggesting that the unknown species might be dissociation fragments of these more common ions.

The extremely high electric field near the emitter is easily capable of dissociating  $H_2^+$  and  $H_3^+$  ions, a fact noted by Clements and Müller,<sup>8</sup> Barofsky,<sup>11</sup> and Ingram and Gomer.<sup>6</sup> In fact, Beckey,<sup>9</sup> and other workers interested in field ionization mass spectroscopy have devoted considerable effort to the study of fragmentation spectra resulting from such dissociations, and have carried out calculations<sup>46</sup> similar to the one which will be presented shortly.

All of these investigators, however, considered only the spatial dissociation of ions which did not originate at the tip surface. The atom probe results indicate that surface species, after evaporating as positive ions, may also dissociate, a process previously undetected.

The fact that the fractional mass ratios peak about  $m/n = 1.2$ , suggests that the dissociation event occurs, preferentially, at a certain distance from the emitter where the potential has a specific, well-defined value. The ion species after dissociation would then always be accelerated by a definite potential difference, and therefore appear at well-defined positions in time during each oscilloscope sweep. It is important to emphasize that well-defined flight times do not, necessarily, imply that the detected species were formed at the surface, although this is usually the case. Actually, all that is required is that the event was initiated by the evaporation pulse, and that the resulting ion was accelerated by a definite potential difference.

Consider a singly charged surface molecule of mass  $M$  field evaporated, and dissociated in space to form a neutral fragment, and a singly charged fragment of mass  $m$ . If the potential at the tip is  $V_0$ , and the potential in space where dissociation occurs,  $V$ , the final kinetic energy of the charged fragment will be:

$$\frac{1}{2} m v^2 = \left[ \frac{m}{M} (V_0 - V) + V \right] e \quad (51)$$

As can be seen, equation (51) predicts the correct kinetic energy of the fragment for the limiting cases of  $V = V_0$  (dissociation at the tip surface), and  $V = 0$  (dissociation in field free space). Once again, a classical, one dimensional model has been chosen whose validity will be judged, eventually, by the type of solution it generates.

Solving equation (51) for the fragment's velocity, and substituting into equation (2) for its time of travel gives:

$$t^2 = \frac{d^2}{v^2} = \frac{d^2}{2e V_0} \left[ \frac{m}{\left[ \frac{m}{M} + (V/V_0) (1 - m/M) \right]} \right] \quad (52)$$

Because of the two meter flight path currently used, this travel time is long compared to the time delay  $\delta$ , which may safely be neglected. If  $(V_{dc} + \alpha V_{pulse})$  is identified as  $V_0$ , the total voltage at the tip, equation (32) may be used to calculate the observed  $m/n$  ratios. Substitution of  $t^2$  from equation (52), into equation (32) with  $\delta = 0$  gives:

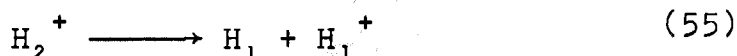
$$\left( \frac{m}{n} \right)_{\text{calculated}} = K V_0 t^2 = \frac{2e}{d^2} V_0 \cdot \frac{d^2}{2e V_0} \left[ \frac{M}{\left[ \frac{m}{M} + \frac{V}{V_0} \left( 1 - \frac{M}{m} \right) \right]} \right] \quad (53)$$

or:

$$\left(\frac{m}{n}\right) \text{ calculated} = \frac{m}{\left[\frac{m}{M} + \frac{V}{V_0} \left(1 - \frac{m}{M}\right)\right]} \quad (54)$$

Where  $\left(\frac{m}{n}\right)$  calculated is the  $m/n$  ratio calculated from equation (32).

Consider the specific dissociation:



for which, equation (54) gives:

$$(m/n) \text{ calculated} = \frac{2}{\left[1 + V/V_0\right]} \quad (56)$$

When  $V = V_0$ , dissociation occurs at the emitter and the calculated ratio equals that of the fragment ion, since it falls through the full potential difference. When  $V = 0$ , dissociation occurs in field free space, and the calculated ratio is that of the parent ion which has fallen through the full potential difference.

Figure 23 is a plot of equation (54) for three specific reactions. As can be seen, a calculated mass ratio of 1.2 corresponds to  $V/V_0 = 0.667$  for the most probable reaction, considered above.



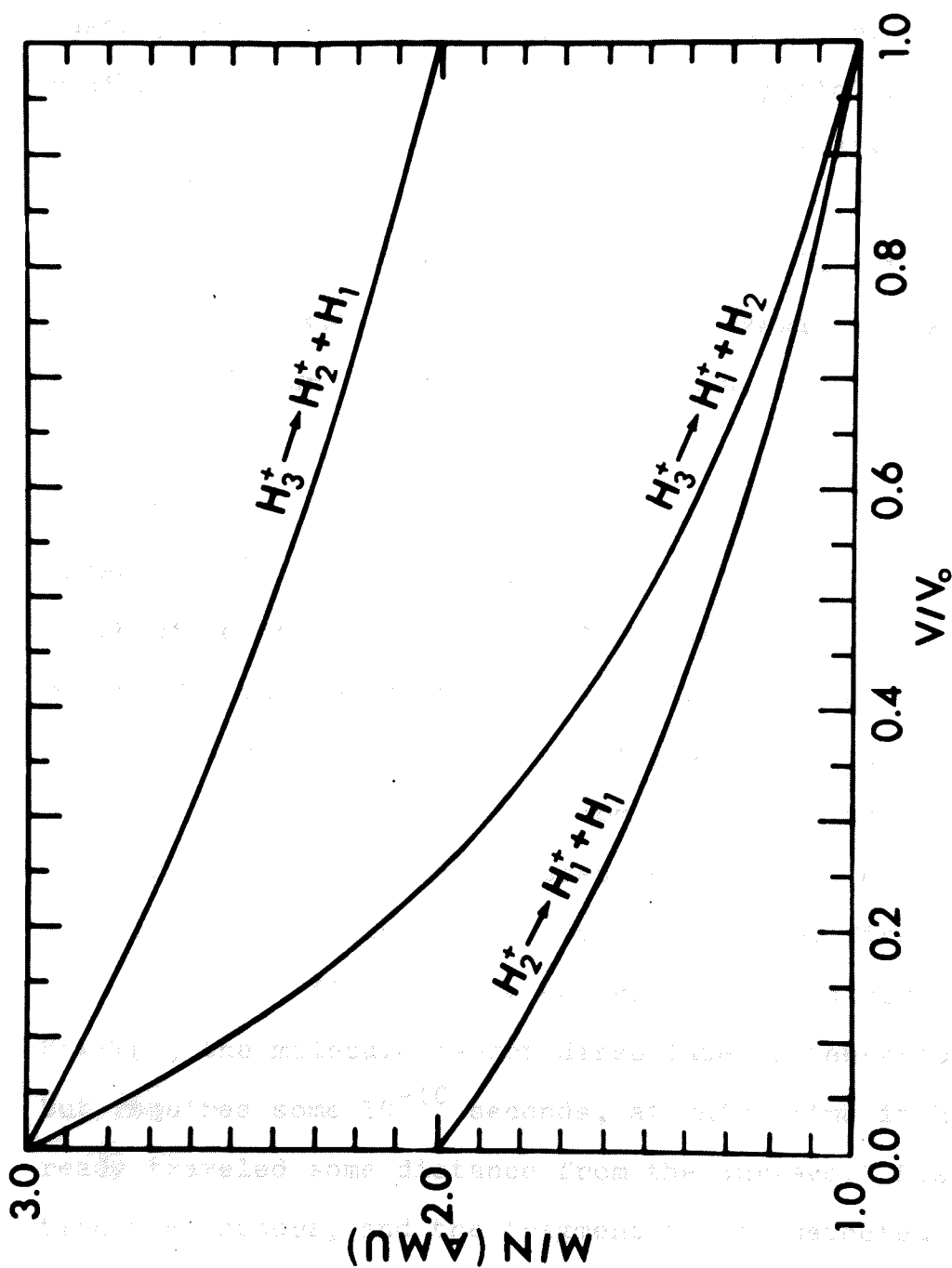


Figure 23. Apparent  $m/n$  vs.  $V/V_0$  for Dissociation

By using the results of appendix A, one can calculate at what distance,  $z$ , from the surface, the dissociation takes place, in terms of the tip radius,  $R$ . Both the tip radius, and the electric field at this spatial position can also be calculated from the results of appendix A, assuming a reasonable field at the tip surface of  $4.5 \text{ V/\AA}$ . Finally, the travel time of the parent ion from surface to this point can be calculated. All of these results are presented in Figure 24, for three characteristic tip voltages,  $V_0$ .

The results indicate that the parent ion takes on the order of  $10^{-10}$  seconds to reach the spatial position at which dissociation is assumed to occur. This is just the order of magnitude of the dissociation time for an excited  $\text{H}^+$  ion in a very high electric field, as calculated by Hiskes,<sup>47</sup> and Wind.<sup>48,49,50</sup> From these results a simple model of the dissociation process emerges. A molecular ion, once field evaporated from the surface, finds itself in an electric field strong enough to cause dissociation. However, the molecule cannot dissociate instantaneously, but requires some  $10^{-10}$  seconds, at which time it has already traveled some distance from the surface. Dissociation then occurs, and the fragment ion is detected as a fractional mass-ratio in the atom probe.

TIP VOL (VOLTS)	TIP RADIUS (M)	M/N (AMU)	V/VO	Z/R	FIELD (VOLTS/M)	TRAVEL-TIME (SECONDS)
4000.0	0.15070-07	1.000	1.000	0.0	0.45000 11	0.0
4000.0	0.15070-07	1.100	0.818	0.37700 01	0.52700 10	0.25460-12
4000.0	0.15070-07	1.200	0.667	0.25000 02	0.88220 09	0.10580-11
4000.0	0.15070-07	1.300	0.538	0.11520 03	0.19440 09	0.38450-11
4000.0	0.15070-07	1.400	0.429	0.42250 03	0.53190 08	0.12230-10
4000.0	0.15070-07	1.500	0.333	0.13000 04	0.17300 08	0.34190-10
4000.0	0.15070-07	1.600	0.250	0.34760 04	0.64720 07	0.85160-10
4000.0	0.15070-07	1.700	0.176	0.82750 04	0.27190 07	0.19200-09
4000.0	0.15070-07	1.800	0.111	0.17890 05	0.12580 07	0.39730-09
4000.0	0.15070-07	1.900	0.053	0.35660 05	0.63090 06	0.76400-09
4000.0	0.15070-07	2.000	0.0	0.66350 05	0.33910 06	0.13790-08
6000.0	0.23490-07	1.000	1.000	0.0	0.45000 11	0.0
6000.0	0.23490-07	1.100	0.818	0.34390 01	0.57120 10	0.31660-12
6000.0	0.23490-07	1.200	0.667	0.21500 02	0.10230 10	0.12400-11
6000.0	0.23490-07	1.300	0.538	0.93780 02	0.23870 09	0.42570-11
6000.0	0.23490-07	1.400	0.429	0.32770 03	0.68550 08	0.12880-10
6000.0	0.23490-07	1.500	0.333	0.96720 03	0.23250 08	0.34470-10
6000.0	0.23490-07	1.600	0.250	0.24920 04	0.90280 07	0.82690-10
6000.0	0.23490-07	1.700	0.176	0.57420 04	0.39180 07	0.18040-09
6000.0	0.23490-07	1.800	0.111	0.12060 05	0.18660 07	0.36250-09
6000.0	0.23490-07	1.900	0.053	0.23420 05	0.96060 06	0.67900-09
6000.0	0.23490-07	2.000	0.0	0.42570 05	0.52850 06	0.11970-08
8000.0	0.32220-07	1.000	1.000	0.0	0.45000 11	0.0
8000.0	0.32220-07	1.100	0.818	0.32190 01	0.60500 10	0.36620-12
8000.0	0.32220-07	1.200	0.667	0.19300 02	0.11360 10	0.13760-11
8000.0	0.32220-07	1.300	0.538	0.80990 02	0.27610 09	0.45360-11
8000.0	0.32220-07	1.400	0.429	0.27350 03	0.82110 08	0.13240-10
8000.0	0.32220-07	1.500	0.333	0.78340 03	0.28700 08	0.34370-10
8000.0	0.32220-07	1.600	0.250	0.19660 04	0.11440 08	0.80260-10
8000.0	0.32220-07	1.700	0.176	0.44260 04	0.50830 07	0.17100-09
8000.0	0.32220-07	1.800	0.111	0.91060 04	0.24710 07	0.33650-09
8000.0	0.32220-07	1.900	0.053	0.17360 05	0.12960 07	0.61860-09
8000.0	0.32220-07	2.000	0.0	0.31040 05	0.72490 06	0.10730-08
10000.0	0.41190-07	1.000	1.000	0.0	0.45000 11	0.0
10000.0	0.41190-07	1.100	0.818	0.30560 01	0.63270 10	0.40800-12
10000.0	0.41190-07	1.200	0.667	0.17740 02	0.12330 10	0.14850-11
10000.0	0.41190-07	1.300	0.538	0.72250 02	0.30930 09	0.47460-11
10000.0	0.41190-07	1.400	0.429	0.23760 03	0.94480 08	0.13470-10
10000.0	0.41190-07	1.500	0.333	0.66500 03	0.33810 08	0.34140-10
10000.0	0.41190-07	1.600	0.250	0.16350 04	0.13760 08	0.78080-10
10000.0	0.41190-07	1.700	0.176	0.36160 04	0.62220 07	0.16330-09
10000.0	0.41190-07	1.800	0.111	0.73200 04	0.30740 07	0.31620-09
10000.0	0.41190-07	1.900	0.053	0.13760 05	0.16350 07	0.57300-09
10000.0	0.41190-07	2.000	0.0	0.24280 05	0.92670 06	0.98050-09
12000.0	0.50370-07	1.000	1.000	0.0	0.45000 11	0.0
12000.0	0.50370-07	1.100	0.818	0.29290 01	0.65620 10	0.44470-12
12000.0	0.50370-07	1.200	0.667	0.16560 02	0.13190 10	0.15770-11
12000.0	0.50370-07	1.300	0.538	0.65800 02	0.33930 09	0.49130-11
12000.0	0.50370-07	1.400	0.429	0.21180 03	0.10600 09	0.13640-10
12000.0	0.50370-07	1.500	0.333	0.58150 03	0.38660 08	0.33880-10
12000.0	0.50370-07	1.600	0.250	0.14060 04	0.16000 08	0.76160-10

Figure 24. Dissociation Data for  $H_2^+ \rightarrow H_1^+ + H_1$

Beckey,<sup>47</sup> interestingly, shows that the dissociation of a molecular ion in a high electric field becomes more improbable as the ratio of charged to uncharged species increases. For this reason, the  $\text{He-Rh}^{2+}$  and  $\text{H-Rh}^{2+}$  ions previously mentioned were detected intact, without dissociation. Of course, the model presented is only intended as a semiquantitative explanation of the fractional mass ratios observed. The author realizes its limitations, and presents the calculations only to give an order of magnitude estimate of the expected dissociation times.

## VIII. SUMMARY AND CONCLUSION

By combining a field ion microscope and a time-of-flight mass spectrometer, an instrument has been successfully developed which is capable of preselecting a surface species, removing it by field evaporation from an atomically resolved metal surface, and determining the mass-to-charge ratio,  $m/n$ , of the resulting ion. Random detector signals are effectively eliminated since the flight time of the selected ion is recorded by an oscilloscope whose ten or twenty microsecond time sweep is initiated by the evaporation pulse itself. Specific calibration procedures for this "atom probe FIM" assure an  $m/n$  determination of at least  $\pm 1.0$  amu at  $m/n = 50$ . However, when two or more known species appear on a single time sweep, the  $m/n$  ratio of an unknown species on the same sweep may be determined to  $\pm 0.2$  amu at  $m/n = 50$ . Such accuracy is sufficient to unambiguously identify metal-hydride molecules as commonly occurring species on a "clean" imaged FIM surface.

Further experiments have indicated the presence of field adsorbed noble gas atoms on the emitter surface. These adsorbates may be field desorbed together with a metal ion to form various metal-noble gas molecule ions.

The field evaporation of numerous metals in vacuum and gas is found to occur essentially with the charge of

the ion predicted theoretically. However, several metals also show ions of higher charge, up to four-fold in the case of tungsten. The experiments suggest that the charge of the ion species example, the continual appearance of only pure metal ions when the probe hole was placed in the area of the zone line decorations of tungsten and iridium, clearly indicated that these decorations were displaced metal ions, and not oxides, nitrides, or other impurities as might have been imagined.

## APPENDIX A

Ion Travel Times Between Confocal Parabolic Electrodes

In order to calculate the travel time of ions between the tip and grounded cathode cap (see Figure 4), it is necessary to choose a potential model which realistically approximates the true electrode geometry. Approximating the tip and cathode cap as concentric spheres<sup>51</sup> results in a simple analytic expression for the travel time. Unfortunately, the model is unrealistic since it ignores both the true shape of the specimen, as well as the electrode assembly which supports the tip. A more satisfactory approximation is to choose the tip and ground electrode as two members of a family of confocal paraboloids of revolution. The resulting potential distribution, first obtained by Eyring et. al.<sup>52</sup> and later used by Rose<sup>53</sup> and Russell<sup>54</sup> to calculate electron trajectories in an idealized field emission microscope, can be used to obtain an order of magnitude calculation for the travel time of ions in the atom probe. Although other geometries are also easily handled, the confocal paraboloid approximation is probably as good as any<sup>55</sup> particularly if the travel time of axial ions are of primary interest. For simplicity, then, the specimen tip and its associated mounting will be approximated by a paraboloid of revolution having a vertex radius of curvature equal to the actual radius of the field ion microscope tip. This radius can be quite simply calculated once an

analytic expression for the potential (and hence the electric field at the surface of the specimen) is obtained. The copper enclosure surrounding the tip (see Figure 7B) will be approximated by a second confocal paraboloid; the geometry forcing its vertex radius of curvature to be numerically equal to twice the actual tip to electrode distance. The aperture in the grounded electrode will be ignored in the calculation since in practice its diameter is less than the tip to electrode distance. The origin of coordinates is taken, for convenience, at the focus of the paraboloid representing the tip.

Because of the geometry chosen, the potential is easily found by expressing Laplace's equation in confocal parabolic coordinates. Consider confocal paraboloids of revolution about the  $z$ -axis. The ordinary cartesian coordinates  $(x, y, z)$  are related to the confocal parabolic coordinates  $(\xi, \eta, \phi)$  by the transformations:<sup>56</sup>

$$x = (\xi\eta)^{\frac{1}{2}} \cos\phi \quad (\text{A-1})$$

$$y = (\xi\eta)^{\frac{1}{2}} \sin\phi \quad (\text{A-2})$$

$$z = \frac{1}{2} (\eta - \xi) \quad (\text{A-3})$$

From these transformations, the metric in the confocal paraboloidal system can be easily found. It is, in fact, for this orthogonal curvilinear coordinate system, just:



$$ds = \frac{1}{2} \left( \frac{\eta}{\xi} + 1 \right)^{\frac{1}{2}} d\xi + \frac{1}{2} \left( \frac{\xi}{\eta} + 1 \right)^{\frac{1}{2}} d\eta + (\xi\eta)^{\frac{1}{2}} d\phi \quad (\text{A-4})$$

Now, restrict the discussion to the family of confocal paraboloids of revolution described by  $\eta = \text{constant}$ . Since only  $\eta$  will enter into the boundary conditions, the potential must depend only upon this coordinate. In other words, Laplace's equation in curvilinear coordinates, for this special case, reduces to:

$$\nabla^2 \Phi = \frac{1}{h_\eta h_\xi h_\nu} \frac{\partial}{\partial \eta} \left[ \frac{h_\eta h_\xi}{h_\nu} \frac{\partial \Phi}{\partial \eta} \right] = 0 \quad (\text{A-5})$$

where the scale factors  $h_\eta$ ,  $h_\xi$ , and  $h_\nu$  are found from the metric to be:

$$h_\eta = \frac{1}{2} \left( \frac{\xi}{\eta} + 1 \right)^{\frac{1}{2}} \quad (\text{A-6})$$

$$h_\xi = \frac{1}{2} \left( \frac{\eta}{\xi} + 1 \right)^{\frac{1}{2}} \quad (\text{A-7})$$

and:

$$h_\phi = (\xi\eta)^{\frac{1}{2}} \quad (\text{A-8})$$

Substitution of A-6, A-7, and A-8 into A-5 yields:

$$\frac{d}{d\eta} \left( \eta \frac{d\Phi}{d\eta} \right) = 0 \quad (\text{A-9})$$

which can be integrated twice with respect to  $\eta$  to give,  
for the potential:

$$\Phi = C \ln \eta + B \quad (\text{A-10})$$

It is now convenient to express  $\eta$  in terms of cylindrical coordinates  $(r, z)$  where  $z$  is measured as before, and  $r$ , the perpendicular distance from the  $z$ -axis to the point of interest is just:

$$r = (x^2 + y^2)^{\frac{1}{2}} \quad (\text{A-11})$$

In terms of these new coordinates  $(r, z)$  the potential,  $\Phi$ , becomes:

$$\Phi = C \ln \left[ z + (r^2 + z^2)^{\frac{1}{2}} \right] + B \quad (\text{A-12})$$

where the equality:

$$\eta = z + (r^2 + z^2)^{\frac{1}{2}} \quad (\text{A-13})$$

has been used, and can be verified from the transformation equations(A-1)-(A-3). At the tip where  $z = z_0$ ,  $\Phi = V_0$ . At the other electrode where  $z = z_1$ ,  $\Phi = 0$ . Combining these boundary conditions with equation(A-10) gives, for the potential:

$$\Phi = \frac{V_0}{\ln (z_0/z_1)} \ln \left[ \frac{z + (r^2 + z^2)^{\frac{1}{2}}}{2z_1} \right] \quad (\text{A-14})$$

which is equivalent to:

$$\phi = \frac{V_o}{\ln (z_o/z_1)} \ln \left[ \frac{z + z (1 + r^2/z^2)^{1/2}}{2z_1} \right] \quad (\text{A-15})$$

For paraxial ions  $r/z \ll 1$  Therefore:

$$\phi \approx \frac{V_o}{\ln (z_o/z_1)} \ln \left[ \frac{2z}{2z_1} \right] \quad (\text{A-16})$$

The electric field strength at the tip is, from equation (A-16) just:

$$\left. \frac{\partial \phi}{\partial z} \right|_{z = z_o} \equiv F = \frac{V_o}{\ln (z_o/z_1)} \frac{1}{z_o} \quad (\text{A-17})$$

But the vertex tip radius  $R$  is  $2z_o$ . This can be shown by considering the parabola formed by the interaction of the paraboloid of revolution representing the tip, with, say, the  $y$ - $z$  plane, and recalling that at the tip for points near the  $z$ -axis,  $\eta = 2z_o$ . Combining this result with equation (A-13) and the general expression for the radius of curvature  $R$  of a section of arc gives:

$$R = 2z_o \quad (\text{A-18})$$

Since the best image field,  $F$ , for helium is approximately  $4.5 \text{ V}/\text{\AA}$ , equation(A-17) can be used to predict the tip radius,  $R$ . Solving that equation for  $R$  and setting  $F = 4.5 \text{ V}/\text{\AA}$  gives:

$$R = \frac{V_o}{4.5 \left[ \frac{1}{2} \ln (R/2z_1) \right]} \quad (\text{A-19})$$

Three or four iterations of equation(A-19) gives a value of  $R$ , in angstroms, good to several decimal places. For the atom probe, with  $z_1 = .001 \text{ m}$ , equation(A-19) predicts that an 8 kV tip ( $V_o = 8 \text{ kV}$ ) will have a radius of  $322.2 \text{ \AA}$ , which is in good agreement with experimental data obtained by net plane ring counting.

Since an order of magnitude calculation for the flight time is desired for this work, only axial ions will be considered. The kinetic energy of such ions, at a position  $z$  in space where the potential  $\Phi = V(z)$ , is just:

$$\frac{1}{2} m v(z)^2 = q \left[ V_o - V(z) \right] \quad (\text{A-20})$$

The travel time is obtained by integrating the velocity over the distance traveled. That is:

$$T = \int_{z_o}^{z_1} \frac{dz}{v(z)} = \int_{z_o}^z \frac{dz}{\left[ \frac{2q}{m} \left( V_o - V(z) \right) \right]^{1/2}} \quad (\text{A-21})$$

Using equation A-16 for the potential, the travel time becomes:

$$T = \frac{m}{2qV_0} \int_{z_0}^z \frac{dz}{\left[ 1 - \frac{\ln(z/z_1)}{\ln(z_0/z_1)} \right]^{1/2}} \quad (A-22)$$

The integral may be transformed into a more convenient form by means of the following substitution:

$$\mu \equiv \left[ \ln(z_0/z_1) \right]^{1/2} \left[ 1 - \frac{\ln(z/z_1)}{\ln(z_0/z_1)} \right]^{1/2} \quad (A-23)$$

Then, the travel time becomes:

$$T = -2T_t \frac{z_0}{d_0} \left[ \ln(z_0/d_0) \right]^{1/2} \int_0^{\left[ \ln(z_0/z) \right]^{1/2}} e^{-\mu^2} d\mu \quad (A-24)$$

where  $z_1 \approx d_0$ , the distance between electrodes, and  $T_t \equiv$  terminal time  $= d_0 \left( \frac{m}{2qV} \right)^{1/2}$

Plots of  $T_t / \left( \frac{m}{n} \right)^{1/2}$  as a function of total tip voltage,  $V_0$ , are given in Figure 25 for three values of  $d_0$ . The graph was computer drawn using 200 values of  $V_0$ .

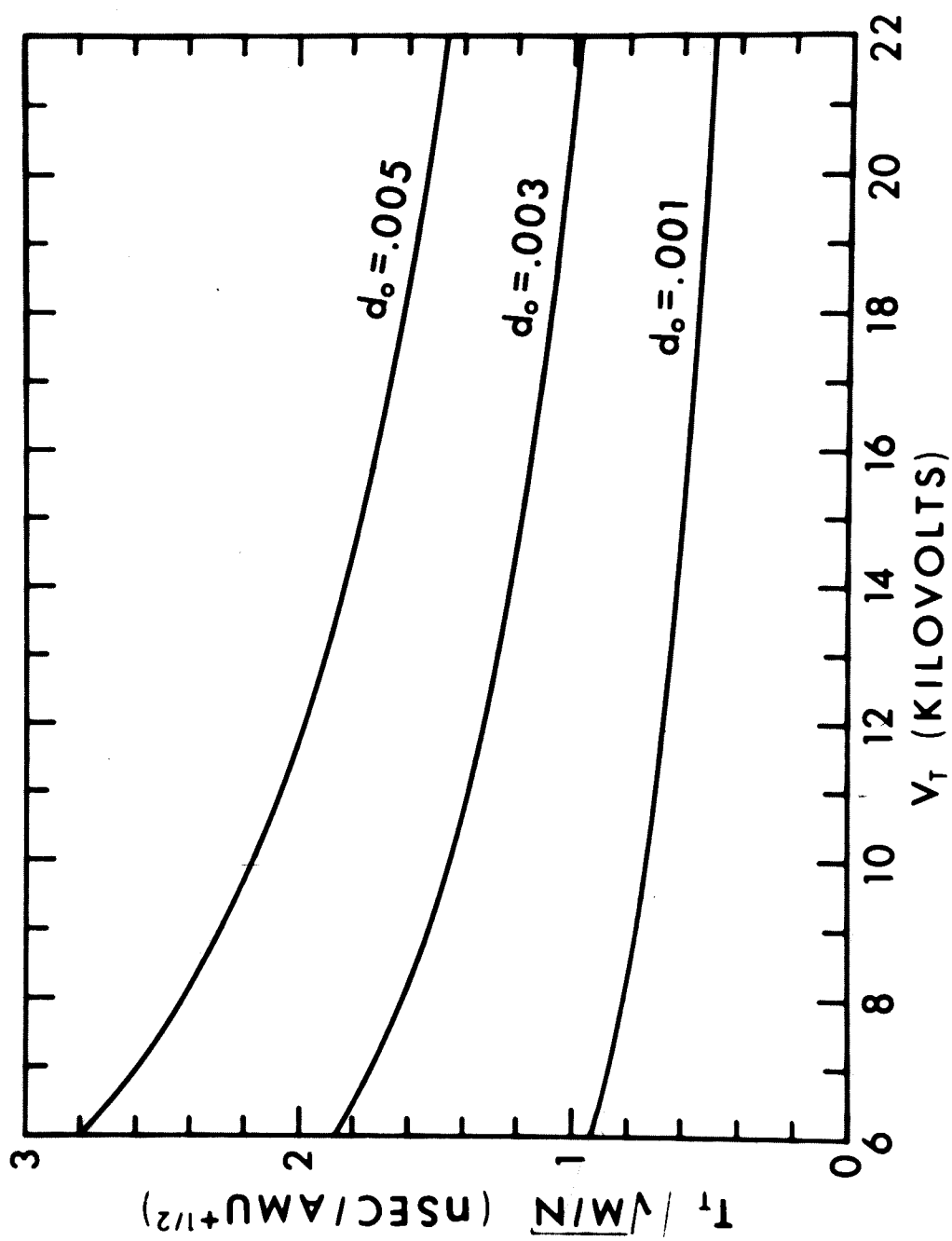


Figure 25. Terminal Travel Times ( $T_t$ )

The new integral in equation(A-24) is just the error integral defined by:

$$\frac{2}{\sqrt{\pi}} \int_0^x e^{-\mu^2} d\mu = \text{erf}(x) = \frac{2}{\sqrt{\pi}} \left[ x - \frac{x^3}{3} + \frac{x^5}{5.2!} - \frac{x^7}{7.3!} + \dots \right] \quad (\text{A-25})$$

so that equation A-24 can be written

$$T = - 2T_t \frac{z_o}{d_o} \left[ \ln (z_o/d_o) \right]^{\frac{1}{2}} \left[ \ln (z_o/z) \right]^{\frac{1}{2}} \times \left[ 1 - \frac{x^2}{3} + \frac{x^4}{5.2!} - \frac{x^6}{7.3!} + \dots \right] \quad (\text{A-26})$$

Where:

$$x \equiv [\ln (z_o/z)]^{\frac{1}{2}} \quad (\text{A-27})$$

Notice that  $\ln (z_o/z)$  and  $\ln (z_o/d_o)$  are both negative numbers. Using this fact, and letting:

$$y \equiv \ln (z_o/z) \quad (\text{A-28})$$

Equation(A-26)becomes:

$$T = T_t \left( \frac{z_o}{d_o} \right)^{\frac{1}{2}} \left| \ln \left( \frac{z_o}{d_o} \right) \right|^{\frac{1}{2}} \left| \ln \left( \frac{z_o}{z} \right) \right|^{\frac{1}{2}} \left[ 1 - \frac{y}{3} + \frac{y^2}{5.2!} - \frac{y^3}{7.3!} \right] \quad (A-29)$$

or equivalently:

$$T = T_t \left( \frac{z_o}{d_o} \right)^{\frac{1}{2}} \left| \ln \left( \frac{z_o}{d_o} \right) \right|^{\frac{1}{2}} \left| \ln \left( \frac{z_o}{z} \right) \right|^{\frac{1}{2}} \left[ 1 + \sum_{v=1}^{\infty} \frac{[-\ln(z_o/z)]^v}{v!(2v+1)} \right] \quad (A-30)$$

Consider the special case  $z = d_o$ . Then  $T$  is just the tip-to-ground cap travel time,  $T_o$ , and equation(A-30)becomes:

$$\frac{T_o}{T_t} = \frac{R}{d_o} \left| \ln(R/2d_o) \right| \left[ 1 + \sum_{v=1}^{\infty} \frac{[-\ln(R/2d_o)]^v}{v!(2v+1)} \right] \quad (A-31)$$

Figure 26 is a computer drawn plot of  $T_o/T_t$  for various values of  $R/d_o$ . To obtain this plot, 200 values of  $R/d_o$  were taken, and for each the series in equation(A-16)was evaluated. Sufficient terms were included (usually about 30) so that the sum of the series was always accurate to seven decimal places. For the atom probe with  $z_1 = .001$  m,



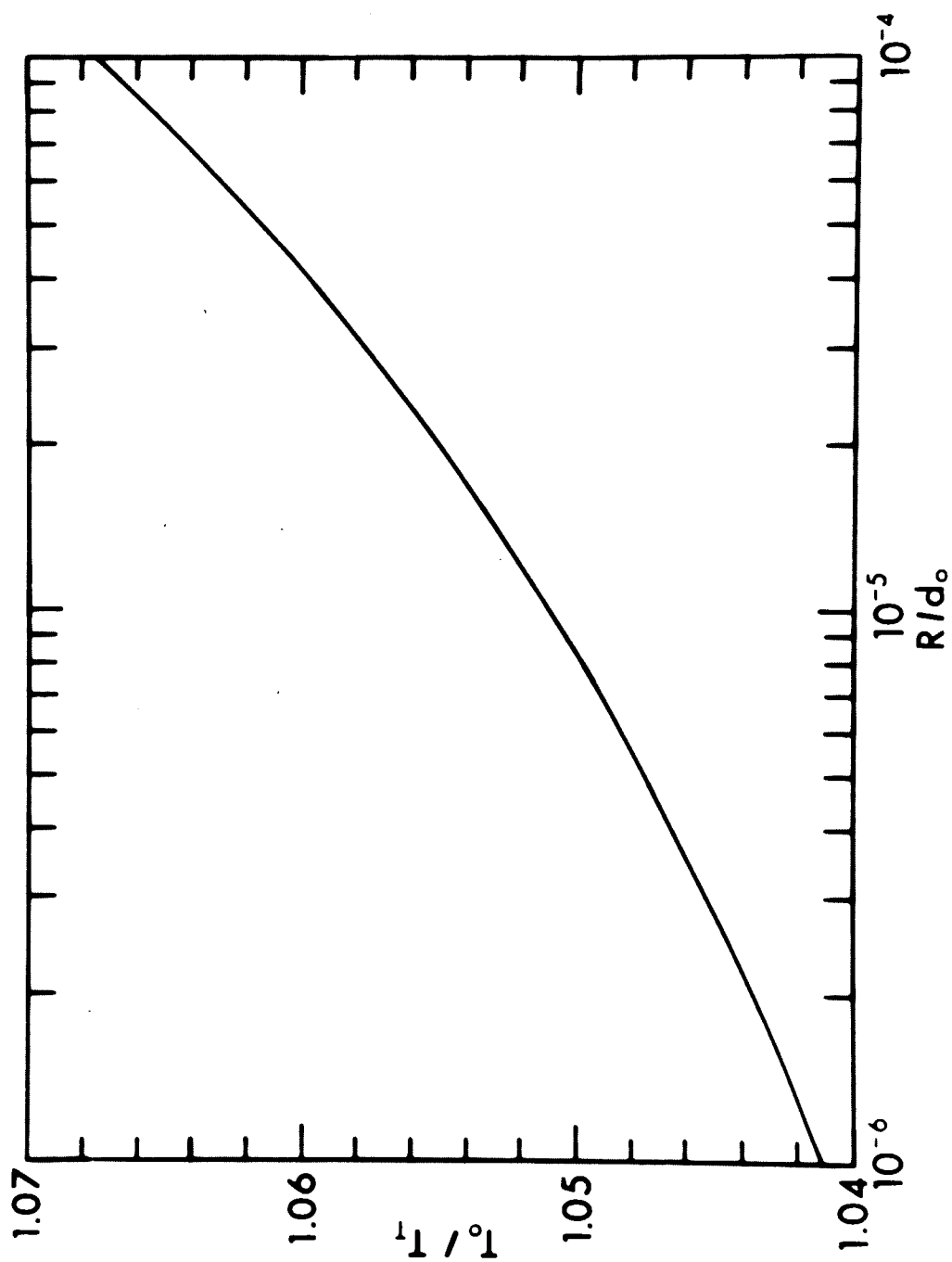


Figure 26. Actual Travel Times ( $T_o$ ) for Confocal Paraboloid Geometry

and  $R = 322.2 \text{ \AA}$  (8kV tip) Figure 25 predicts that  $T_t / (\frac{m}{n})^{\frac{1}{2}} = .81 \text{ nsec} / (\text{amu})^{\frac{1}{2}}$  and Figure 26 that:

$$T_o / T_t = 1.06$$

From which, the tip-to-cathode travel time,  $T_o$ , is just 6.02 nanoseconds for a particle of  $\frac{m}{n} = 49$ .

## APPENDIX B

The Newton-Raphson Method

In order to calculate the pulse factor  $\alpha$ , and the time delay  $\delta$ , equations (42) and (43) must be solved simultaneously. The complexity of the equations demand a numerical solution, which may be obtained by direct application of the Newton-Raphson method. Reference 29 describes the general procedure in detail, which is applied here to the specific problem of determining  $\alpha$  and  $\delta$ .

Equations (42) and (43) may be rewritten as follows:

$$K^2 \sum_i \left[ (V_i + \alpha P_i) (t_i + \delta)^2 - \frac{M}{K} \right] \left[ P_i (t_i + \delta)^2 \right] = 0 \quad (B-1)$$

$$K^2 \sum_i \left[ (V_i + \alpha P_i) (t_i + \delta)^2 - \frac{M}{K} \right] \left[ (V_i + P_i) (t_i + \delta) \right] = 0 \quad (B-2)$$

where  $V_i$ ,  $P_i$ , and  $T_i$  are the DC voltage, pulse voltage, and observed travel time; respectively, which correspond to the  $i^{\text{th}}$  mass spike recorded.  $M$  is defined as the known mass-to-charge ratio being observed (for rhodium,  $M = 51.5$ ). The positive sign for the time delay,  $\delta$ , has been chosen for convenience.

Equations(B-1)and(B-2)are of the form:

$$\xi (\alpha, \delta) = 0 \quad (B-3)$$

$$\eta (\alpha, \delta) = 0 \quad (B-4)$$

Let:

$$\alpha = \alpha_o + a \quad (B-5)$$

and:

$$\delta = \delta_o + d \quad (B-6)$$

where  $\alpha_o$  and  $\delta_o$  are approximate values for the pulse factor and time delay, and a and d are the appropriate correction terms. Substitution of equation(B-5)and(B-6)into equation (B-3)and(B-4)and expanding in a Taylor series about  $\alpha$  and  $\delta$ , gives:

$$\xi(\alpha_o + a, \delta_o + d) \approx \xi (\alpha_o, \delta_o) + a \left( \frac{\partial \xi}{\partial \alpha} \right)_o + d \left( \frac{\partial \xi}{\partial \delta} \right)_o = 0 \quad (B-7)$$

$$\eta(\alpha_o + a, \delta_o + d) \approx \eta (\alpha_o, \delta_o) + a \left( \frac{\partial \eta}{\partial \alpha} \right)_o + d \left( \frac{\partial \eta}{\partial \delta} \right)_o = 0 \quad (B-8)$$

where terms in higher powers of a and d as well as their products have been neglected, since the correction terms, a and d, are assumed small. The subscript "o" attached

to each derivative corresponds to the subscript of  $\alpha$  and  $\delta$ , and indicates that the derivative is to be evaluated for these values of  $\alpha$  and  $\delta$ .

Equations (B-7) and (B-8) may be solved by the method of determinants for the initial correction terms  $a$  and  $d$ . These correction terms, corresponding to the values chosen for  $\alpha$  and  $\delta$  ( $\alpha_0$  and  $\delta_0$ ), will be designated  $a$  and  $d$ . They are just:

$$a_1 = \frac{\begin{vmatrix} -\xi(\alpha_0, \delta_0) & \left(\frac{\partial \xi}{\partial \delta}\right)_0 \\ -\eta(\alpha_0, \delta_0) & \left(\frac{\partial \eta}{\partial \delta}\right)_0 \end{vmatrix}}{\begin{vmatrix} \left(\frac{\partial \xi}{\partial \alpha}\right)_0 & \left(\frac{\partial \xi}{\partial \delta}\right)_0 \\ \left(\frac{\partial \eta}{\partial \alpha}\right)_0 & \left(\frac{\partial \eta}{\partial \delta}\right)_0 \end{vmatrix}} \quad (\text{B-9})$$

$$d_1 = \frac{\begin{vmatrix} -\left(\frac{\partial \xi}{\partial \alpha}\right)_0 & -\xi(\alpha_0, \delta_0) \\ -\left(\frac{\partial \eta}{\partial \alpha}\right)_0 & -\eta(\alpha_0, \delta_0) \end{vmatrix}}{\begin{vmatrix} \left(\frac{\partial \xi}{\partial \alpha}\right)_0 & \left(\frac{\partial \xi}{\partial \delta}\right)_0 \\ \left(\frac{\partial \eta}{\partial \alpha}\right)_0 & \left(\frac{\partial \eta}{\partial \delta}\right)_0 \end{vmatrix}} \quad (\text{B-10})$$

A corrected value for  $\alpha$  and  $\delta$  can now be obtained from equations(B-5)and(B-6):

$$\alpha_1 = \alpha_o + a_1 \quad (B-11)$$

$$\delta_1 = \delta_o + d_1 \quad (B-12)$$

These new values can be used to obtain a further correction, and the process repeated as often as necessary. The calculation is finally terminated when the corrections to  $\alpha$  and  $\delta$  become negligibly small. That is, when  $\alpha$  and  $\delta$  remain unchanged to the accuracy required. The simultaneous solution of equations(B-1)and(B-2)by this method require the following quantities:

$$\xi(\alpha_1, \delta) \equiv K^2 \sum_i \left[ (V_i + \alpha P_i) (t_i + \delta)^2 - \frac{M}{K} \right] \left[ (V_i + P_i) X (t_i + \delta) \right] = 0 \quad (B-13)$$

$$\frac{\partial \xi}{\partial \alpha} = 2K^2 \sum_i \left[ (V_i + \alpha P_i) (t_i + \delta)^2 - \frac{M}{2K} \right] \left[ P_i (t_i + \delta) \right] \quad (B-14)$$

$$\frac{\partial \xi}{\partial \delta} = 3K^2 \sum_i \left[ (V_i + \alpha P_i) (t_i + \delta)^2 - \frac{M}{3K} \right] \left[ V_i + \alpha P_i \right] \quad (B-15)$$

$$\eta(\alpha, \delta) \equiv K^2 \sum_i \left[ (V_i + \alpha P_i) (t_i + \delta)^2 - \frac{M}{K} \right] \left[ P_i (t_i + \delta)^2 \right] = 0 \quad (\text{B-16})$$

$$\frac{\partial \eta}{\partial \alpha} = K^2 \sum_i \left[ P_i (t_i + \delta)^2 \right]^2 \quad (\text{B-17})$$

$$\frac{\partial \eta}{\partial \delta} = (2K)^2 \sum_i \left[ (V_i + P_i) (t_i + \delta)^2 - \frac{M}{2K} \right] \left[ P_i (t_i + \delta) \right] \quad (\text{B-18})$$

A computer program has been written to calculate the correction terms,  $a$  and  $d$ , which correspond to given initial values  $\alpha$  and  $\delta$ . The resulting corrected values for  $\alpha$  and  $\delta$  are used to generate a second-order correction, and the process repeated until  $\alpha$  and  $\delta$ , at succeeding cycles, differ by less than  $1.0 \times 10^{-7}$ . In practice, twenty or thirty cycles are usually required to achieve this accuracy. The resulting numbers are then rounded to two decimal places to give final values for the pulse factor and the time delay.

Scale 0.1 sec. = 1000

11. L. R. Barrick, *Journal of Geophysical Research*, **68**, 1963, p. 4199

University of Illinois

12. W. M. M. *Journal of Geophysical Research*, **68**, 1963, p. 4201

University of Illinois

## BIBLIOGRAPHY

1. E. W. Müller, Z. Physik 136, 131 (1951).
2. T. T. Tsong and E. W. Müller, Chem. Phys. 41, 3284 (1964).
3. E. W. Müller, Phys. Rev. 102, 618 (1956).
4. R. Gomer and L. W. Swanson, J. Chem. Phys. 38, 1613 (1963).
5. E. W. Müller, unpublished data (1953).
6. M. G. Ingram and R. Gomer, J. Chem. Phys. 22, 1279 (1954).
7. E. W. Müller and K. Bahadur, Phys. Rev. 102, 624 (1956).
8. T. C. Clements and E. W. Müller, J. Chem. Phys. 37, 2684 (1962).
9. H. D. Beckey, H. Knöppel, G. Metzinger and P. Schulze, "Advances in Mass Spectroscopy" 3, 35 (1966).
10. M. P. R. Thomsen, Master's Thesis, The Pennsylvania State University (1963).
11. D. F. Barofsky, Master's Thesis, The Pennsylvania State University (1965).
12. D. F. Barofsky, Ph.D. Thesis, The Pennsylvania State University (1967).
13. E. W. Müller and J. A. Panitz, 14th Field Emission Symposium, Washington, D. C. (1967).



14. J. C. Riviere, Phys. Bull. 20, 86 (1969).
15. R. Castaing, "Advances in Electronics and Electron Physics" 13, 317 (1960).
16. A. V. Crewe, Science 154, 729 (1966).
17. E. W. Müller, J. A. Panitz and S. B. McLane, Rev. Sci. Instr. 39, 83 (1968).
18. E. W. Müller, "Advances in Electronics and Electron Physics" 13, 83 (1960).
19. B. Wacławski and E. W. Müller, J. Appl. Phys. 32, 1472 (1961).
20. G. A. Morton, "Advances in Electronics and Electron Physics" 4, 83 (1952)
21. J. S. Allen, "Nucleonics" 3, 36 (1948).
22. J. S. Allen, Proc. I.R.E. 38, 354 (1950).
23. J. S. Allen, Proc. I.R.E. 38, 350 (1950).
24. J. S. Allen, Rev. Sci. Instr. 18, 740 (1947).
25. J. S. Allen, Phys. Rev. 55, 968 (1939).
26. D. A. Gray, Handbook of Coaxial Microwave Measurements, (General Radio Company, West Concord, Mass., (1968), p. 26.
27. J. A. Panitz, S. B. McLane, and E. W. Müller, Rev. Sci. Instr. 40, 1321 (1969).
28. E. W. Müller, Quarterly Rev., 23, 177 (1969).
29. J. B. Scarborough, Numerical Mathematical Analysis, (Johns Hopkins Press, Baltimore, 1966), p. 215.

30. A. D. White and D. L. Ferry, Rev. Sci. Instr. 32, 730 (1961).
31. E. W. Müller, 13th Field Emission Symposium, Bonn, Germany (1968).
32. S. S. Brenner and J. T. McKinney, Appl. Phys. Letts. 13, 29 (1968).
33. E. W. Müller, Private Communication (1969).
34. R. D. Young, 7th Field Emission Symposium, McMinnville, Oregon (1960).
35. G. Ehrlich and F. G. Hudda, Phil. Mag. 8, 1587 (1963).
36. D. Mensel and R. Gomer, 10th Field Emission Symposium, Berea, Ohio (1963).
37. O. Nishikawa and E. W. Müller, J. Appl. Phys. 35, 2806 (1964).
38. E. W. Müller, Science 149, 594 (1965).
39. E. W. Müller, S. B. McLane and J. A. Panitz, Surface Science, (1969).
40. S. S. Brenner and J. T. McKinney, 16th Field Emission Symposium, Pittsburgh (1969).
41. T. T. Tsong, Surface Science 10, 102 (1968).
42. R. Vanselow and W. A. Schmidt, 13th Field Emission Symposium, Ithica, New York (1966).
43. D. F. Barofsky and E. W. Müller, Surface Science 10, 177 (1968).
44. E. W. Müller, Cambridge University Colloquium, Cambridge, England (March 3, 1969).

45. D. G. Brandon, Surface Science 3, 1 (1965).
46. H. D. Beckey and H. Knöppel, Z. Naturf. 21, 1923 (1966).
47. J. R. Hiskes, Phys. Rev. 122, 1207 (1961).
48. H. Wind, Nuclear Fusion 6, 68 (1966).
49. H. Wind, J. Chem. Phys. 42, 2371 (1965).
50. H. Wind, J. Chem. Phys. 43, 2956 (1965).
51. R. Gomer, Field Emission and Field Ionization, (Harvard University Press, Cambridge, Mass., 1961), p. 39.
52. C. F. Eyring, S. S. Mackeown and R. A. Millikan, Phys. Rev. 31, 900 (1928).
53. D. J. Rose, J. Appl. Phys. 27, 215 (1956).
54. A. M. Russell, J. Appl. Phys. 33, 970 (1962).
55. W. P. Dyke, J. K. Trolan, W. W. Dolan and G. Burnes, J. Appl. Phys. 24, 576 (1955).
56. G. Arfken, Mathematical Methods for Physicists (Academic Press, New York, 1966), p. 102.

## VITA

John Andrew Panitz was born in Flushing, New York, on May 31, 1944 and graduated from Bayside High School, Bayside, New York in June 1961. He enrolled at The Pennsylvania State University and received the B.S. degree in Physics in June 1965, and the M.S. degree in Physics in December 1966. During the period 1965 - 1968 he studied under a NASA traineeship, and served as a research assistant upon its termination. Mr. Panitz is the co-author of seven scientific papers, and a member of Sigma Pi Sigma, Pi Mu Epsilon, The American Physical Society, and The Acoustical Society of America.

**THE PENNSYLVANIA STATE UNIVERSITY**  
**PUBLICATION INFORMATION FORM**

Please list chronologically each book, article, piece of music, bulletin, monograph, manual, major review, paper you have had published. (i.e., author, book, title, date; for articles — author, "title in full," name of periodical, volume, date, pages). If you have done creative work, such as painting, sculpture, etc., instead of writing, please describe and list exhibitions or galleries in which your work has been shown:

1. A paper "Field Ion Microscopy of Beryllium" presented by J. A. Panitz at the 13th. Field Emission Symposium, September 6, 1966, at Cornell University.
2. A paper, "An Atom Probe Field Ion Microscope," by E. W. Mueller and J. A. Panitz presented at the 14th Field Emission Symposium, June 27, 1967, The National Bureau of Standards in Gaithersburg, Maryland.
3. A publication "The Atom-Probe Field Ion Microscope", by E. W. Müller, J. A. Panitz and S. B. McLane, Rev. Sci. Instr. 39, 83 (1968).
4. A paper "An Atom Probe Field Ion Microscope" authored by E. W. Mueller, S. B. McLane and J. A. Panitz ~~to be~~ presented at the 4th Regional European Conference on Electron Microscopy, September 4, 1968, at Rome, Italy.
5. A paper "A New Atom-Probe FIM" authored by E. W. Muller, S. B. McLane, and J. A. Panitz ~~will be~~ presented by E. W. Müller at the 15th Field Emission Symposium, September 13, 1968, at Bonn, Germany.
6. A paper, "Calibration of the Atom-Probe F.I.M.", by J. A. Panitz, S. B. McLane and E. W. Müller, Rev. Sci. Instr. 40, 1321 (1969).
7. A paper, "Field Adsorption and Desorption of Helium and Neon", by E. W. Müller, S. B. McLane and J. A. Panitz, accepted for publication in Surface Science, November, 1969.